

THE PHOTOCHEMISTRY OF “SUPER” PHOTOACID N-METHYL-6-HYDROXYQUINOLINIUM AND OTHER NOVEL PHOTOACIDS

A Dissertation
Presented to
The Academic Faculty

by

Elizabeth-Ann Gould

In Partial Fulfillment
of the Requirements for the Degree
Doctor of Philosophy in the
School of Chemistry and Biochemistry

Georgia Institute of Technology
May 2012

THE PHOTOCHEMISTRY OF “SUPER” PHOTOACID N-METHYL-6-HYDROXYQUINOLINIUM AND OTHER NOVEL PHOTOACIDS

Approved by:

Dr. Laren M. Tolbert, Advisor
School of Chemistry and Biochemistry
Georgia Institute of Technology

Dr. Lawrence A. Bottomley
School of Chemistry and Biochemistry
Georgia Institute of Technology

Dr. Jean-Luc Brédas
School of Chemistry and Biochemistry
Georgia Institute of Technology

Dr. David M. Collard
School of Chemistry and Biochemistry
Georgia Institute of Technology

Dr. William J. Koros
School of Chemical and Biomolecular
Engineering
Georgia Institute of Technology

Date Approved: January 27, 2012

ACKNOWLEDGEMENTS

This dissertation would not have been possible without the professional and personal support of innumerable colleagues, friends, and family members. In Dr. Laren Tolbert's laboratory, I found an intellectually nurturing environment that allowed me to flourish professionally. As my advisor, Laren provided me with the right balance between structure and freedom that allowed me to thrive. It is a privilege to have been the student of such an accomplished scientist and personally fine individual. Dr. Kyril Solntsev has been in every sense of the word my mentor. Kyril never accepted what I produced as good enough and always demanded that I strive harder. Without that moving bar, I might never have learned to stretch myself intellectually. By example, Kyril taught me what it means to be a true scholar and exacting scientist. I will always be indebted to him and will always value his friendship. Dr. Janusz Kowalik, an unquestionably talented scientist, broadened my perspective on chemistry and gave invaluable assistance with my work. Janusz made complete, in both expertise and personality, the rich environment of the Tolbert laboratory.

No graduate experience can be successful without the support and assistance of student colleagues. Russell Vegh has been my laboratory companion and friend from the beginning; I repeatedly depended on his support which he readily provided. I am also grateful to Mike Salvitti, whose scientific contributions laid the groundwork for this research. I must also express my thanks to the current and former members of the Tolbert Group, including Brett Fellows, Jing Chen, Juan Vargas, Nathan Jarnagin, and Yoon-Keun Chae, who were a consistent source of insightful commentary on my work and personal encouragement.

An important part of my graduate education was achieved through collaboration with scientists in other laboratories. I would especially like to thank Dr. Dan Huppert who not only opened his laboratory, but also his home to me. The insight that I gained while working with him in Tel Aviv was invaluable to my growth as a chemist. Dr. Alex Popov has also been an integral part of this research. The ability to marry theory and experiment has been pivotal to my work, and without Alex this marriage would not have been possible. Finally, Dr. Rui Nunes provided both experimental support and lively scientific discourse. It has been an absolute honor to work with such gifted people.

The faithful dedication of my students, Jack Bright, Verjine Khodaverian, Ben Recca, Catherine Robinson, and Alix Shamir has been nothing short of a blessing. Working with them has allowed me to extend my project into areas that would have otherwise gone unexplored. These students also provided me the opportunity to teach, a skill that I try to continue to develop.

It is with the deepest gratitude that I thank my parents, Drs. Dan and Karen Gould. Their lifelong steadfast love and support has enabled me to thrive both academically and personally. It is the small fraction of their love of learning which I inherited that has made me successful in this venture. I can only hope to follow in the footsteps of my incredibly bright, talented, and successful parents as I continue my academic and professional journey. I also extend my deepest thanks and appreciation to my grandparents, Arthur and Barbara Hovagimian, who have supported my academic career since its inception. Their unequivocal support of and contribution to my education has been unwavering. I would also like to thank my father- and mother-in-law, Mike and Sue Bartolo, and my sister-in-law, Daniela Bartolo, all of whom have extended their

support unconditionally. Finally, it would be impossible for me not to acknowledge my husband, Mike Bartolo and our beautiful son, Lino, both of whom bring me immeasurable happiness. Without them, the celebration of achievements such as this would certainly fall short. Without my family, my graduate career would not have been possible and I am forever grateful and indebted to each of them individually as well as a whole for their unwavering devotion.

TABLE OF CONTENTS

	Page
ACKNOWLEDGEMENTS	iii
LIST OF TABLES	ix
LIST OF FIGURES	xi
LIST OF ABBREVIATIONS	xvi
LIST OF SYMBOLS	xix
SUMMARY	xxi
<u>CHAPTER</u>	
1 INTRODUCTION AND OVERVIEW	1
References	7
2 EXCITED-STATE PROTON TRANSFER IN CHIRAL ENVIRONMENTS: PHOTORACEMIZATION OF NOVEL CHIRAL LIGANDS	9
Introduction	9
Experimental Protocols	11
Results	13
Discussion and Conclusions	19
References	23
3 DESIGN, SYNTHESIS, AND PROPERTIES OF A NOVEL “SUPER” PHOTOACID, <i>N</i> -METHYL-6-HYDROXYQUINOLINIUM (MHQ)	26
Part I: Synthesis and General Characterization	26

Introduction	26
Experimental Protocols	30
Results	31
Discussion and Conclusions	34
Part II: Excited-State Proton Transfer Kinetics of MHQ Salts: Experiment and Theory	37
Introduction	37
Experimental Protocols	39
Results	41
Discussion and Conclusions	55
References	73
4 MHQ AS A PHOTOCHEMICAL AGENT IN VARIOUS MICROHETEROGENEOUS SYSTEMS	77
Part I: Studies of the Photoinduced Cationic Polymerization of Cyclohexene Oxide using MHQ	77
Introduction	77
Experimental Protocols	78
Results	80
Discussion and Conclusions	86
References	90
Part II: A Fluorescence Tool for Understanding Excited-State Proton Transfer in Supercritical Media	92
Introduction	92
Experimental Protocols	93
Results	96

Discussion and Conclusions	102
References	113
Part III: MHQ Photophysics in Nafion Films	115
Introduction	115
Experimental Protocols	117
Results	118
Discussion and Conclusions	120
References	123
5 FLUORESCENCE QUENCHING OF QUINOLINIUM SALTS: SOLVENT EFFECTS	125
Introduction	125
Experimental Protocols	127
Results	128
Discussion and Conclusions	143
References	151
6 CONCLUSIONS AND FUTURE WORK	154
APPENDIX A: CHARACTERIZATION OF COMPOUNDS STUDIED	161
APPENDIX B: SSDP AND FFIT FITS FOR MHQ KINETICS	164
APPENDIX C: ALGORITHM OF BROWNIAN DYNAMICS SIMULATIONS	177
References	191

LIST OF TABLES

	Page
Table 3.1: Solvatochromism of MHQ-Nf.	34
Table 3.2: Parameters used for calculating the curves in Figure 3.14.	48
Table 3.3: Diffusion coefficients: “self” vs. “effective” used for BD simulations.	53
Table 3.4: Multiexponential decays of MHQ in various solvents.	56
Table 3.5: Parameters of the proton and solvent coordinate rates used for calculating the dissociation rate of MHQ and DCN2 in various alcohols.	62
Table 3.6: Parameters of the proton and solvent coordinate rates used for calculating the association rate of MHQ in various alcohols.	65
Table 3.7: Values of the enthalpy, ΔH , and entropy, ΔS , of the proton transfer reaction obtained as slopes and intercepts of the pK_a^* curves in Figure 3.22.	66
Table 3.8: Values of the parameters in Eq. 3.9 used for fitting the diffusion coefficients in Figure 3.25.	71
Table 4.1: Protolytic dissociation constants, k_d , for MHQ in MeOH/scCO ₂ .	104
Table 4.2: Slopes of Arrhenius plots for MHQ in MeOH/scCO ₂ .	106
Table 4.3: Slopes of Arrhenius plots for MHQ in MeOH/dioxane mixtures.	109
Table 4.4: Values of enthalpy, ΔH , and entropy, ΔS , of the proton transfer reaction of MHQ in MeOH/dioxane.	112
Table 4.5: Average lifetimes of MHQ in Nafion.	122
Table 5.1: Structures of quinolinium salts studied.	129
Table 5.2: Lifetimes in the absence of quencher and Stern-Volmer quenching constants for all quinoliniums studied.	140
Table 5.3: Lifetimes in MeCN and quenching rate constants of MQ, isoMQ, 4MMQ and 6MMQ in ethers.	144
Table B.1: SSDP fit parameters for MHQ in alcohols.	164

Table B.2: SSDP Fits of C* and Z* decays on MHQ in various alcohols at different temperatures.	167
Table B.3: SSDP fit parameters for MHQ in MeOH/scCO ₂ mixtures.	170
Table B.4: SSDP Fits of C* and Z* decays on MHQ in MeOH/scCO ₂ mixtures; vol MeOH=0.33 mL.	172
Table B.5: SSDP Fits of C* and Z* decays on MHQ in MeOH/scCO ₂ mixtures; vol MeOH=0.40 mL.	173
Table B.6: SSDP Fits of C* and Z* decays on MHQ in MeOH/scCO ₂ mixtures; vol MeOH=0.50 mL.	174
Table B.7: SSDP fit parameters for MHQ in MeOH/dioxane mixtures.	175
Table B.8: SSDP Fits of C* and Z* decays on MHQ in MeOH/dioxane mixtures.	176

LIST OF FIGURES

	Page
Figure 1.1: Proton transfer and decay processes in reversible photoacids.	3
Figure 1.2: Structure and HOMO/LUMO orbital diagrams of 2N.	5
Figure 2.1: Photochemical processes in BINOLs.	11
Figure 2.2: Enantioselectivity of BINOL in MeOH/H ₂ O, α -D-methylglucoside, aminobutanol, and sec-butylamine..	14
Figure 2.3: Photolysis of S-(-)-BINOLs in toluene + 2-butylamine.	15
Figure 2.4: Mechanism of BINOL photocyclization.	21
Figure 3.1: Structure and HOMO/LUMO orbital diagrams of DCN2.	27
Figure 3.2: Structure and HOMO/LUMO orbital diagrams of MHQ.	28
Figure 3.3: Synthetic pathway for preparation of MHQ salts.	32
Figure 3.4: Uv-vis absorption spectra of MHQ-Nf in BuOH and DMSO.	33
Figure 3.5: Steady-state emission spectra of MHQ salts in BuOH and DMSO	33
Figure 3.6: Fluorescent pathways of MHQ salts.	35
Figure 3.7: Geminate recombination reaction scheme.	37
Figure 3.8: TCSPC decay curves monitored at 460 nm for MHQ salts in BuOH and MHQ-Nf in MeCN/DMSO and MeCN/water.	41
Figure 3.9: Fluorescence upconversion of MHQ-Nf in various alcohols and at various wavelengths.	42
Figure 3.10: H/D isotope effect on the ESPT of MH.	43
Figure 3.11: ROH [*] /C [*] decays of DCN2/MHQ in EtOH at T=86–297 K.	44
Figure 3.12: RO ⁻ */Z [*] decays of DCN2/MHQ in EtOH at T=197–297 K.	45
Figure 3.13: MHQ kinetic scheme.	47

Figure 3.14: Fluorescence decays of MHQ in BuOH and results of BD simulations at different R_{reac} .	49
Figure 3.15: Fluorescence decays of MHQ in BuOH, results of BD simulations and fittings using SSDP with time-dependent PMF and Kirkwood's effective potential.	50
Figure 3.16: MSDs from BD simulations.	51
Figure 3.17: MSDs from BD simulations without reaction and with interaction only between the proton and counterion.	52
Figure 3.18: Arrhenius plot of protolytic photodissociation for MHQ and DCN2 in EtOH.	59
Figure 3.19: Protolytic photodissociation rates of MHQ at different temperatures in various alcohols.	60
Figure 3.20: Protolytic photodissociation activation energies for MHQ and DCN2 in various alcohols.	63
Figure 3.21: Association rates of MHQ protolytic photodissociation in various alcohols at different temperatures.	65
Figure 3.22: MHQ pK_{a}^* values in various alcohols at different temperatures.	66
Figure 3.23: Mutual diffusion coefficients of a proton-zwitterion pair at different temperatures in BuOH.	68
Figure 3.24: MSD of a proton-zwitterion pair at $T=293$ K in BuOH.	69
Figure 3.25: Mutual diffusion coefficients of a proton-zwitterion pair in various alcohols at different temperatures.	70
Figure 4.1: Reaction scheme of polymerization of CHO by MQs and NMR spectra of reaction mixture at various times.	80
Figure 4.2: Kinetics of polymerization of CHO by various MHQ salts.	81
Figure 4.3: Kinetics of polymerization of CHO by MHQ, MMQ, and MQ.	82
Figure 4.4: pH change upon irradiation of MHQ and its derivatives with and without CHO in acetone.	84

Figure 4.5: pH change upon irradiation of pentafluorophenols in acetone.	85
Figure 4.6: Proposed mechanism of acid production via electron transfer from CHO to MQ followed by proton abstraction from CHO.	87
Figure 4.7: Proposed mechanism of acid production via excited-state acetone.	88
Figure 4.8: Steady-state emission of MHQ in MeOH/scCO ₂ at various temperatures and pressures.	96
Figure 4.9: Steady-state emission of MHQ in MeOH/dioxane ($X_{\text{MeOH}} = 0.6$) at various temperatures.	97
Figure 4.10 : C* (450 nm) decays of MHQ in MeOH/scCO ₂ . X_{MeOH} : 0.25-0.61 Pressure:129-215 bar; Temperature: 313-300K.	98
Figure 4.11: Z* (610 nm) decays of MHQ in MeOH/scCO ₂ . X_{MeOH} : 0.25-0.61; Pressure:129-215 bar; Temperature: 313-300K.	98
Figure 4.12: C* (450 nm) decays of MHQ in MeOH/dioxane. X_{MeOH} : 0.55-0.72; Temperature: 307-330 K.	99
Figure 4.13: Z* (610 nm) decays of MHQ in MeOH/dioxane. . X_{MeOH} : 0.50-0.70; Temperature: 307-330 K.	100
Figure 4.14: Normalized steady-state emission of MHQ in MeOH/scCO ₂ mixtures at various pressures.	103
Figure 4.15: Arrhenius plots for MHQ in MeOH/scCO ₂ mixtures as determined by steady-state and time-resolved measurements.	105
Figure 4.16: MHQ in MeOH/scCO ₂ : recombination rate, k_r , at various pressures, X_{MeOH} , and temperatures.	107
Figure 4.17: Arrhenius plotsfor MHQ in MeOH/dioxane calculated from steady-state and time-resolved methods.	108
Figure 4.18: MHQ in MeOH/dioxane: ESPT rates, k_d and $Z^*/C^*\tau_{Z^*}$, vs. X_{MeOH} from steady-state and time-resolved methods.	109
Figure 4.19: MHQ in MeOH/dioxane: Z* lifetime, τ_{Z^*} , vs. 1000/T.	110
Figure 4.20: MHQ in MeOH/dioxane: recombination rate, k_r , vs. 1000/T.	111

Figure 4.21: MHQ in Nafion: water solutions before/after 24 hr soak.	118
Figure 4.22: Steady-state emission of MHQ in Nafion 117 and 115.	119
Figure 4.23: MHQ in Nafion: TCSPC decays of C* (440 nm) and Z* (610 nm).	120
Figure 4.24: MHQ fluorescence quenching in Nafion: dry vs. wet films.	122
Figure 5.1: Fluorescence quenching of MQ, isoMQ, 4MMQ and 6MMQ by ethers.	130
Figure 5.2: Fluorescence quenching of MHQ and MMQ by ethers.	131
Figure 5.3: Fluorescence quenching of 6CNMQ by ethers.	132
Figure 5.4: Fluorescence quenching of MQ, isoMQ, 4MMQ and 6MMQ by hydroxylic solvents.	133
Figure 5.5: Fluorescence quenching of MHQ and MMQ by hydroxylic solvents.	134
Figure 5.6: Fluorescence quenching of 6CNMQ by hydroxylic solvents.	134
Figure 5.7: Fluorescence quenching of MQ, isoMQ, 4MMQ and 6MMQ by nucleophilic solvents.	135
Figure 5.8: Fluorescence quenching of MHQ and MMQ by nucleophilic solvents.	136
Figure 5.9: Fluorescence quenching of 6CNMQ by nucleophilic solvents.	137
Figure 5.10: Fluorescence quenching of MHQ in water and DMSO	138
Figure 5.11: MHQ decays at 440 nm in MeCN/DMSO and MeCN/water	138
Figure 5.12: MHQ decays at 610 nm in MeCN/DMSO and MeCN/water	139
Figure 5.13: Lifetimes of MHQ in DMSO and water	139
Figure 5.14: Fluorescence quenching of various quinoliniums as a function of quencher nucleophilicity.	145
Figure 5.15: 1-naphthol quenching by photoprotonation.	146
Figure 5.16: Nucleophilic quenching mechanism of quinolinium salts.	147
Figure 5.17: Fluorescence quenching of various MHQ salts by DMSO and water.	150
Figure 6.1: Proposed chiral “super” photoacid.	158

Figure 6.2: Proposed “super” photoacid based on anthracene.	159
Figure C.1: Real and model systems for BD simulations.	178
Figure C.2: Time dependent PMF between the proton and Z^* at several instants of time.	188
Figure C.3: Comparison of U_{eff} calculated from BD simulations, the PMF from Eqs. C.10 and C.11.	191

LIST OF ABBREVIATIONS

2-Me-THF	2-methyl-tetrahydrofuran
2N	2-naphthol
4MMQ	<i>N</i> -methyl-4-methylquinolinium
6CNMQ	<i>N</i> -methyl-6-cyanoquinolinium
6HQ	6-hydroxyquinoline
6MMQ	<i>N</i> -methyl-6-methylquinolinium
BD	Brownian dynamics
BINOL	1,1'-bis-2-naphthol
BTFMP	bis(trifluoromethyl)phenol
BuOH	1-butanol
C/C*	Ground/excited-state cation
CD	Circular dichroism
CHE	1-cyclohexylethylamine
CHO	Cyclohexene oxide
CI	Counteranion
CPL	Circular polarized luminescence
DCN2	5,8-dicyano-2-naphthol
DFP	2,3-difluorophenol
DFT	Density functional theory
DLS	Dynamic light scattering
DMF	Dimethylformamide

DMS	Dimethylsulfide
DMSO	Dimethylsulfoxide
DSE	Debye-Smoluchowsky equation
ESPT	Excited-state proton transfer
EtOH	Ethanol
EWG	Electron withdrawing group
FWHM	Full width half maximum
GPC	Gel permeation chromatography
GPE	Glycidyl phenyl ether
GR	Geminate recombination
HOMO	Highest occupied molecular orbital
HPLC	High-performance liquid chromatography
HPTA	8-hydroxy- <i>N,N,N',N',N'',N''</i> -hexamethylpyrene-1,3,6,-trisulfonamide
HPTS	8-hydroxypyrene-1,3,6-trisulfonic acid
IRF	Instrument response function
ISE	Ion selective electrode
isoMQ	<i>N</i> -methylisoquinolinium
KIE	Kinetic isotope effect
LUMO	Lowest unoccupied molecular orbital
Me2BINOL	2,2'-dimethoxy-1,1'-bi-2-naphthyl
MeBINOL	2-hydroxy-2'-methoxy-1,1'-bi-2-naphthyl
MeCN	Acetonitrile
MeOH	Methanol

MHQ	<i>N</i> -methyl-6-hydroxyquinolinium
MMQ	<i>N</i> -methyl-6-methoxyquinolinium
MQ	<i>N</i> -methylquinolinium
MSD	Mean-square displacement
NaOH	Sodium hydroxide
Nf	Nonaflate; nonafluorobutanesulfonate
NMR	Nuclear magnetic resonance
PAG	Photoacid generator
PFP	Pentafluorophenol
pK _a [*]	Excited-state acidity constant
PMF	Potential of mean force
PrOH	Propanol
R6G	Rhodamine 6G
scCO ₂	Supercritical carbon dioxide
SSDP	Spherically Symmetric Diffusion Problem
TCSPC	Time-correlated single photon counting
Tf	Triflate; trifluoromethanesulfonate
THF	Tetrahydrofuran
THP	Tetrahydropyran
UV	Ultraviolet
VANOL	3,3'-diphenyl-2,2'-bi-1-naphthol
VAPOL	2,2'-diphenyl-3,3'-4-biphenanthrol
Z/Z [*]	Ground/excited-state zwitterion

LIST OF SYMBOLS

a/R_{reac}	Contact distance
D	Diffusion Coefficient
E	Energy
G	Entropy
g_{lum}	Luminescence dissymmetry factor
H	Enthalpy
I	Fluorescence intensity
$k_a/k_r/k_{\text{pt}}$	Association rate constant
k_B	Boltzmann constant
k_d/k_{pt}	Prototypic photodissociation rate constant
k_f	Radiative rate constant
k_H	Proton coordinate rate constant
k_{nf}	Non-radiative rate constant
k_{nuc}	Rate of reaction of ethers with benzyl cation
k_q	Quenching rate constant
k_s	Solvent coordinate rate constant
K_{SV}	Stern-Volmer quenching constant
N_A	Avagadro's number
$\text{p}K_a(*)$	Ground(excited)-state acidity constant
R	Universal gas constant
R_D	Debye radius

$\text{RO}^{\cdot -}/\text{A}^{\cdot -}$	Excited-state anionic photoacid
RO^-/A^-	Anionic hydroxyarene photoacid
$\text{ROH}^{\cdot}/\text{AH}^{\cdot}$	Excited-state neutral photoacid
ROH/AH	Neutral hydroxyarene photoacid
U	Potential
X_A	Mole fraction of A
ϵ	Dielectric constant
λ	Wavelength
τ	Fluorescence lifetime
τ_D	Dielectric relaxation time
ϕ	Fluorescence quantum yield

SUMMARY

Reversible photoacids are molecules that exhibit a large pK_a drop upon excitation, but return to the ground-state pK_a upon excited-state decay. These transient photoacids are grouped roughly into two categories: “normal” photoacids that have excited-state acidity constants (pK_a^*) greater than zero, and “super” photoacids that have pK_a^* s less than zero. While these reversible photoacids are not used in industrial applications, they are used in basic research. Excited-state proton transfer (ESPT), or the dissociation of a photoacid in the excited state, is central to photoacid research; consequently, understanding the properties and kinetics of the ESPT in various novel photoacids was the major focus of the research presented here.

The present research began with the study of ESPT in chiral environments; experiments were conducted that examined the ESPT to/from chiral proton donors to chiral and achiral acceptors. The role of the exergonicity of the reaction and the transition-state position along the reaction coordinate for the existence of an enantiomeric effect was established and compared to previously studied “super” photoacids. A photoracemization was observed for the chiral photoacids (BINOLs), which was ultimately attributed to a “late” transition state similar to a planar achiral binaphtholate anion.

While this work proved fruitful and interesting, the research was limited by the excited-state acidity of the BINOLs, which have excited-state pK_a^* s greater than zero. Interest in studying photoacids capable of more facile deprotonation in the excited-state

led to the design and synthesis of the “super” photoacid, *N*-methyl-6-hydroxyquinolinium (MHQ).

With the successful synthesis of various MHQ salts, we explored the ESPT dynamics of MHQ and discovered that it is the strongest photoacid reported in the literature to-date with a $\text{pK}_a^* \approx -7$. Because little work has been conducted on photoacid salts, one goal of the research was to explore the effects of the counteranion on the ESPT. While we found that the proton-transfer step is independent of the counteranion, results indicate that the counteranion does affect some of the dynamics in these systems. As stated above, understanding the proton-transfer kinetics in these systems was a major goal of our research; therefore, the ESPT reaction of MHQ was studied using both fluorescence upconversion and time-correlated single photon counting techniques. The ultrafast kinetics were investigated in various alcohols and water and determined to be solvent-controlled. The ESPT temperature dependence of MHQ was also studied in various alcohols and compared to the ESPT temperature dependence observed for another “super” photoacid, 5,8-dicyano-2-naphthol (DCN2). A full set of kinetic and thermodynamic parameters describing the ESPT was obtained. The protolytic photodissociation rate constant for MHQ was higher than for DCN2, while the ESPT activation energies of MHQ were smaller. These findings were attributed to the approximately 3 orders of magnitude differences in excited-state acidities of MHQ and DCN2.

The research was then extended to the marriage of experiment and theory in order to further characterize the MHQ kinetics. Due to the complexity of the system upon photodissociation, the typical description of the reversible ESPT within the framework of

the Spherically Symmetric Diffusion Problem (SSDP) was not possible. Further, the system is a three-body problem and the presence of counteranion causes additional complications that affect the proton mobility. Consequently, Brownian dynamics (BD) simulations were performed as a tool to reveal the interaction potentials and to elucidate the role of the counterion on the diffusion and reactive properties in the system. The results indicated that the anisotropy of the potential force can be taken into account after adapting this force for use in SSDP. The results of both the BD simulations and the SSDP calculations with the adapted potential were used to fit the experimental kinetics with excellent agreement.

Concurrently, we conducted several experiments exploring potential application of MHQ. Because MHQ exhibits such a dramatic pK_a drop in the excited state, its use as a photoinitiator in cationic polymerization was of interest. The photoinitiated cationic polymerization of cyclohexene oxide (CHO) by MHQ through direct ESPT was explored. Although MHQ did, in fact, polymerize CHO upon irradiation in acetone solution, control experiments revealed that the polymerization occurs via irreversible ground-state acid formation. Further, control studies on several reversible photocatalysts for cationic polymerization revealed similar latent acid production.

The microheterogeneous environment of supercritical carbon dioxide ($scCO_2$) expanded liquids was explored using MHQ as a probe. Previous work showed that ESPT is, in fact, possible in gas-expanded liquids for “super” photoacids. The ESPT kinetics of MHQ were studied in various methanol/ $scCO_2$ mixtures. The results were fitted with the SSDP program using the modified potential from the BD simulations described above. A full set of kinetic and thermodynamic parameters were obtained for the system. The

ESPT rate constants, however, were unaffected by the introduction of CO₂ into the environment. This was attributed to the extremely strong preferential solvation of MHQ by methanol, where the system was in the exergonic regime and therefore the ESPT rate remained relatively constant.

Finally, MHQ was used as a photoprobe in the Nafion membrane. Nafion is the preeminent membrane used in polymer exchange membrane fuel cells and while there has been much effort applied to elucidation of the microheterogeneous structure in the membrane, the current model is still quite over-simplified. To probe the proton transport channels in Nafion, the ESPT of MHQ was investigated as a function of film hydration and film thickness as monitored spectroscopically. The absorption of the photoacid into the dye was found to be a function of the film thickness. ESPT was observed in water-swollen films; however, little ESPT was seen at low hydration levels. This suggests that a significant amount of water is needed in the film in order for ESPT to occur. Of particular note is the observation that upon drying the films, the overall emission increased by more than two orders of magnitude, indicating that the fluorescence of MHQ is quenched in environments where ESPT occurs.

The observation of the quenching phenomenon of MHQ by proton-accepting solvents led to a broad study of quenching of various quinolinium compounds. Several different quinolinium compounds, capable and incapable of ESPT, were synthesized. The quenching of these salts by several different classes of quenchers was studied. These classes included ethers, hydroxylic solvents, and nucleophilic solvents. While previous work attributed the fluorescence quenching of quinolinium salts to electron transfer, this research led to different conclusions. While the exact quenching mechanism remains

elusive, in the case of ethers an interesting correlation between quencher nucleophilicity and the Stern-Volmer quenching constant of the quinolinium was observed. Therefore, an unusual mechanism was proposed involving nucleophilic attack on the electron-poor aromatic ring, leading to development of a curve-crossing with the ground state and rapid internal conversion. In cases where no ESPT is possible, the lack of quenching by non-nucleophilic hydroxylic solvents and the very efficient quenching by nucleophilic solvents such as DMSO, is in good agreement with this mechanism. For all systems in which ESPT can occur (MHQ in proton accepting solvents), the overall emission is heavily quenched, indicating that ESPT is involved in quenching.

CHAPTER 1

INTRODUCTION AND OVERVIEW

The dissociation reaction of a protonic acid is one of the simplest and most widely studied reactions in chemistry. As a result, the ground-state reactions of protonic acids are well characterized; the characterization of their excited-state counterparts, however, remains a much more elusive subject.

The acid-base properties of aromatic compounds in the excited state are vastly different from those in the ground-state and are closely related to electronic structure. Photoacids, such as amino- and hydroxyaromatics, greatly increase their acidity in the excited state, while photobases, such as nitrogen aromatics, greatly increase their basicity. Because of its applications, the photoinduced dissociation of a protonic acid in the excited state, or excited-state proton transfer (ESPT), is of special importance in the area of photochemistry. For example, intermolecular ESPT reactions have been used as mechanistic tools in pH jump experiments,¹ as dynamic fluorescent probes in complex systems such as proteins² and micelles,³ in the study of proton hydration dynamics,⁴ and in photolithography applications.⁵

Evidence of excited-state proton transfer (ESPT) was first reported in 1931 by Weber⁶ who noted an emission change with pH of 1-naphthylamine-4-sulfonate while the absorbance spectrum stayed the same. In the following decades, the works of Förster and Weller laid the groundwork for the study of ESPT reactions.⁷ In 1949, Förster^{7a} explained the phenomenon by observing dual fluorescence emission from 2-naphthol, but only single emission from its methyl ether derivative. He attributed this observation to excited-

state intermolecular proton transfer (ESPT). Excited-state proton association and dissociation processes are a function of the excited electronic structure resulting from absorption. Since excited states have inherently short lifetimes, relaxation to the ground-state occurs, thus creating the transient nature of the pH drop. Excited-state proton transfer has been observed in various aromatic compounds including ammonium biaryl systems³ and hydroxyarenes⁴ (ArOH, or AH). Reversible, or transient, photoacids are defined as compounds which exhibit a large, reversible pK_a drop upon excitation but return to the original ground-state pK_a upon removal of the excitation source. Transient photoacids are grouped into two categories: “normal” and “super” photoacids. “Normal” photoacids are limited by excited-state pK_a (pK_a^*) values of greater than zero, whereas “super” photoacids are defined analogously to “super” acids with a $pK_a^* < 0$ and are capable of ESPT in non-aqueous environments. These molecules can reversibly drop as many as 13 pK_a units in the excited state.¹⁰ A general scheme for the reversible proton transfer and decay processes in hydroxyarene photoacids is shown in the Förster cycle represented in Figure 1.1.

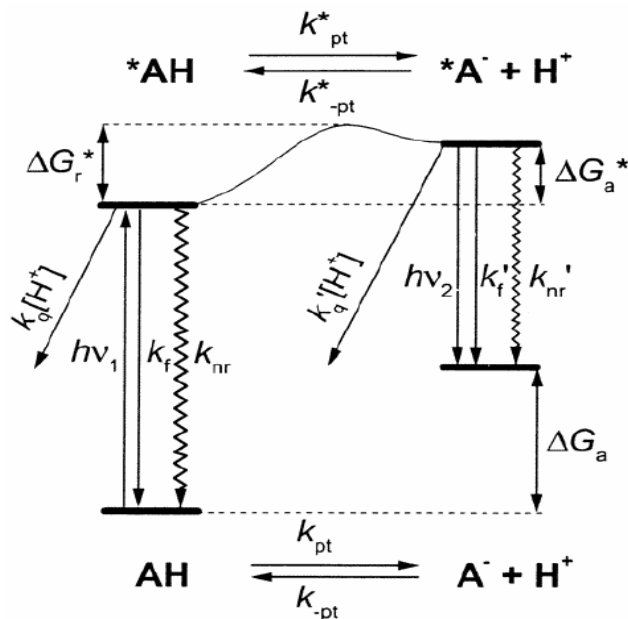


Figure 1.1. Proton transfer and decay processes in reversible photoacids.¹⁰

The processes undergone by reversible photoacids upon photoexcitation can be both radiative and non-radiative. In Figure 1.1, k_{pt} and k_{-pt} are the rate constants of simple ground-state proton dissociation and association, respectively. Acid-base equilibrium may also be established during the lifetimes of the excited states ($1/k_{pt}^*$, $1/k_{-pt}^*$) and result in emission from the neutral (AH^*) or anionic (A^{*-}) species (k_f , k_f'); however, various non-radiative decay processes can quench the fluorescence of the excited states (k_{nr} , k_{nr}'). These processes include, but are not limited to, proton-induced quenching¹¹ (k_q) and radical formation via homolytic O-H bond cleavage.¹⁰ In order to understand the systems studied in this research, it is important to determine the kinetic and thermodynamic parameters of the proton transfer processes using a combination of steady-state and time-resolved spectroscopies.

The enthalpy changes in the ground and excited states are represented by ΔH and ΔH^* , respectively. From the energy relations shown in Figure 1.1,

$$\Delta H^* - \Delta H = N_A h (\nu_{RO-} - \nu_{ROH}) \quad (\text{Eq. 1.1})$$

where N_A is Avogadro's number, h is Planck's constant, and ν_{ROH} and ν_{RO-} are the frequencies of the electronic transitions of the naphthol and its conjugate base. Assuming that

$$\Delta H^* - \Delta H \approx \Delta G^* - \Delta G \quad (\text{Eq. 1.2})$$

where ΔG^* is the free energy of the proton transfer in the ground (excited) state, and

$$\Delta G^* = 2.3RT \text{p}K_a^* \quad (\text{Eq. 1.3})$$

the following relation, known as the Förster equation, is obtained:

$$\text{p}K_a^* = \text{p}K_a + (E_A - E_{HA})(0,0)/2.3RT \quad (\text{Eq. 1.4})$$

This equation assumes that the entropy of protonation, ΔS , is the same in the ground and excited states. Although this is a good approximation for the excited-state acidity enhancement, it does not take into account solvent relaxation or changes in molecular geometry.

The molecule 2-naphthol (2N) is one of the most studied photoacids in the literature to-date and is considered a good model for quantifying these systems.⁵ The hydroxyl moiety is capable of proton transfer to various aqueous organic solvents and although only the neutral species may be observed in the ground-state, dual emission is observed from both the neutral (AH^* , Figure 1.1) and anionic species (A^-* , Figure 1.1)

under ESPT conditions. Like most photoacids, ESPT in 2N is solvent-dependent.

Although 2N is a good model for ESPT reactions, it is only mildly acidic in the excited state with a pK_a^* of 2.5.^{9a}

Applying basic Hückel molecular orbital theory, a simple model to estimate excited-state acidity can be used by calculating the electron redistribution in the excited state.¹⁰ Upon excitation and absorption of a photon, reversible photoacids undergo a transition from the highest occupied molecular orbital (HOMO) to the lowest unoccupied molecular orbital (LUMO). Photoexcited electrons are delocalized throughout the molecule and the electron density shifts away from the acidic hydroxyl moiety towards the ring, thus pulling electron density away from the O-H bond and allowing for easier dissociation of the proton. Upon deexcitation, the electron density returns to its original ground-state distribution, thus creating the transient increase in acidity. The HOMO and LUMO molecular orbital diagrams of 2N can be seen in Figure 1.2.

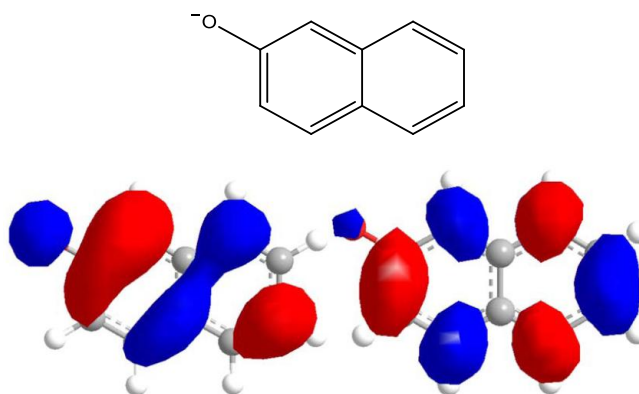


Figure 1.2. Structure and HOMO/LUMO orbital diagrams of 2N. (HOMO/LUMO calculated using semi-empirical method AM1.)

The applications of reversible photoacids are seemingly inexhaustible. Protons are only dissociated during irradiation, creating better time control of the reaction. Production of

acid through irradiation is a relatively recent development, and the most common processes involve irreversible photoacid generators (PAGs). Traditional photoacid generators produce permanent acid upon irradiation via photodegradation. PAGs are important due to their wide range of applications. In photosensitive polymeric systems, they are used as initiators¹² and crosslinkers,¹³ or in the conversion of acid-sensitive functional groups.¹⁴ In the microelectronics industry, PAGs are used in photolithography for the production of photoresists and UV curing materials.¹⁵ A major drawback to these traditional PAGs is the irreversibility of the chemical reaction, resulting in latent acid and byproduct formation. Reversible photoacid systems overcome permanent acid and byproduct formation by their photostability and by returning to neutral conditions upon removal of the irradiation source. While there have yet to be industrial applications to transient photoacids, they are used in a number of basic research settings. As stated above, reversible photoacids and ESPT have been employed as mechanistic tools in pH jump¹ experiments to study proton hydration dynamics,⁴ as well as in technological applications such as photolithography.⁵ Additionally, reversible photoacids can be used as fluorescent labels for studying biological applications and in controlling various biological functions such as protein folding and unfolding.¹⁶ Excited-state proton transfer systems can also be used to study various transport processes such as proton transport in synthetic and biological membranes.

References

1. Clark, J.H., Shapiro, S.L.; Campillo, A.J.; Winn, K.R. *J. Am. Chem. Soc.* **1979**, 101, 746.
2. (a) Loken, M.R.; Hayes, J.W.; Gohlke, J.R.; Brand, L. *Biochem.* **1972**, 11, 4779. (b) Gutman, M.; Nachliel, E.; Huppert, D. *Eur. J. Biochem.* **1982**, 125, 175. (c) Gutman, M. *Methods Biochem. Anal.* **1984**, 30, 1.
3. (a) Politi, M.J.; Chaimovich, H. *J. Phys. Chem.* **1986**, 90, 282. (b) Chattopadhyay, N.; Dutta, R.; Chowdhury, M. *J. Photochem. Photobiol. A: Chem.* **1989**, 47, 249. (c) Bardez, E.; Monnier, E.E.; Valeur, B. *J. Phys. Chem.* 1985, 89, 5031.
4. (a) Huppert, D.; Kolodney, E. *Chem. Phys.* **1981**, 63, 401. (b) Robinson, G.W.; Thistlethwaite, P.J.; Lee, J. *J. Phys. Chem.* **1986**, 90, 4224.
5. Mansueto, E.S.; Wight, C.A. *J. Am. Chem. Soc.* **1989**, 111, 1900.
6. Weber, K.Z. *Phys. Chem., B15* **1931**, 18.
7. (a) Forster, T. *Naturwissenschaften* **1949**, 36, 186. (b) Forster, T. *Elektrochemie* **1950**, 54, 43. (c) Forster, T. *Pure Appl. Chem. Int. Ed. Engl.* **1964**, 3, 1. (d) Weller, A. *Naturwissenschaften* **1955**, 42, 175 (e) Weller, A. *Electrochemistry* **1952**, 56, 662. (f) Weller, A. *Prog React. Kinet.* **1961**, 1, 187.
8. Arnaut, L.G.; Formosinho, S.J. *Photochem. Photobiol. A* **1993**, 75, 1.
9. For reviews see: (a) Ireland, J.F.; Wyatt, P.A.H., *Adv. Phys. Org. Chem.* **1976**, 12, 131. (b) Schulman, S.G. *Fluorescence of Phosphorescence Spectroscopy*; Pergamon Press: Elmsfor, NY, 1977. (c) Shizuka, H. *Acc. Chem. Res.* **1985**, 18, 141.
10. Tolbert, L.M.; Solntsev, K.M. *Acc. Chem. Res.* **2002**, 35, 19.
11. Tsutsumi, K.; Shizuka, H. *Chem. Phys. Lett.* **1977**, 52, 485.

12. Wei, Y.; Wang, W.; Yeh, J.M.; Wang, B.; Yang, D.C.; Murray, J.K. *Adv. Mater.* **1994**, 6, 372
13. (a) Harvard, J.M.; Yoshida, M.; Pasini, D.; Vladimirov, N.; Frechet, J.M.J.; Medeiros, D.R.; Patterson, K.; Yamada, S.; Willson, C.G.; Byers, J.D.J. *Polym. Sci. Part A: Polym. Chem.* **1999**, 37, 1225 (b) Yu, H.S.; Yamashita, T.; Horie, K. *Macromolecules* **1996**, 29, 1144 (c) Chae, K.H.; Park, I.J., Choi, M.H. *Bull. Korean. Chem. Soc.* **1993**, 14, 614
14. (a) Kim, S.T.; Kim, J.B.; Chung C.M.; Ahn, D.D. *J. Appl. Polym. Sci.* **1997**, 66, 2507
(b) Chen, J.P.; Goa, J.P.; Wang, Z.Y.J. *Poly. Sci., Part A: Polym. Chem.* **1997**, 35, 9.
(c) Kim, H.K.; Ober, C.K. *Polym. Bull.* **1992**, 28, 33.
15. Ito, H. *Adv. Polym. Sci.* **2005**, 172, 37.
16. Sato, S.L.; Luisi, D.L. Raleigh, D. P. *Biochemistry* **2000**, 39, 4955

CHAPTER 2

EXCITED-STATE PROTON TRANSFER IN CHIRAL ENVIRONMENTS: PHOTORACEMIZATION OF NOVEL CHIRAL LIGANDS*

*This section is heavily drawn from Solntsev, K.M.; Bartolo (Gould), E-A; Pan, G; Muller, G.; Bommireddy, S.; Huppert, D.; Tolbert, L.M. Excited-State Proton Transfer in Chiral Environments: Photoracemization of BINOLs *Isr. J. Chem.* **2009**, 49, 227.

Introduction

Biological systems involving proton transfer generally exhibit a very high stereoselectivity. A large number of biologically active molecules are chiral, including sugars and natural amino acids. Previous work described pronounced differences in ESPT rates from the “super” photoacid DCN2 to optical isomers of 2-butanol,² where protolytic dissociation was 2.6 times faster in the enantiopure alcohol than in its racemic form. This phenomenon was explained in terms of long-range order and stability of homo- vs. heterodimers of the chiral alcohol, thus adding a unique dynamic approach to the field of chiral recognition using optical tools.³ In search of a stereospecificity in ESPT, the intermolecular ESPT from one of the simplest chiral photoacids known, 1,1'-bis-2-naphthol (BINOL) and its methyl ether was studied. BINOL and its derivatives have been widely used for chiral recognition and as industrial catalysis for asymmetric reactions.³

Iwanek and Mattay⁴ studied the chirality effect on the BINOL neutral band emission quenching by various optically active amines in numerous solvents and in most cases, very small or no enantioselectivity was detected. The maximum ratio of Stern-Volmer constants for the S-(-)- and R-(+)-BINOL fluorescence quenching by chiral

amines was 1.15 for BINOL/1-cyclohexylthylamine and BINOL/N,N-dimethylphenylethylamine in acetonitrile. A significant emission from the anionic BINOLate with an unusually large Stokes shift was observed in various organic solvents with strong proton acceptors (amines), while emission from the neutral form was quenched.

A similar abnormal Stokes shift was also noted by Shi and Wan⁵ for 2-hydroxy-2'-methyl-1,1'-binaphthyl in MeCN/H₂O 1/1 vol mixtures upon ground-state deprotonation. They proposed twisting of the excited-state anionic fluorophore leading to a more planar structure, therefore enhancing the conjugation between the two naphthyl rings. Later, Flegel et al.⁶ proposed a detailed resonance scheme for the excited "BINOLate" planarization that is identical to the scheme reported by the Tolbert Group earlier.⁷ There was not, however, any direct experimental evidence for the proposed mechanism. Flegel et al.⁶ studied the photoracemization of BINOL in methanol and D₂O/MeCN. They proposed that *intramolecular* ESPT was the driving force for the photoracemization. The work presented here, however, demonstrates that *intermolecular* ESPT is the major process contributing to the photoracemization of BINOLs. The photochemistry of BINOL in MeOH and MeCN mixtures with water was studied extensively by Flegel et al.⁶ and by Zandomeneghi et al.⁸ In contrast to the results presented here, no ESPT product was observed in the emission spectra, and the photolysis led to the formation of photoproducts A⁶ or B⁸ (Figure 2.1).

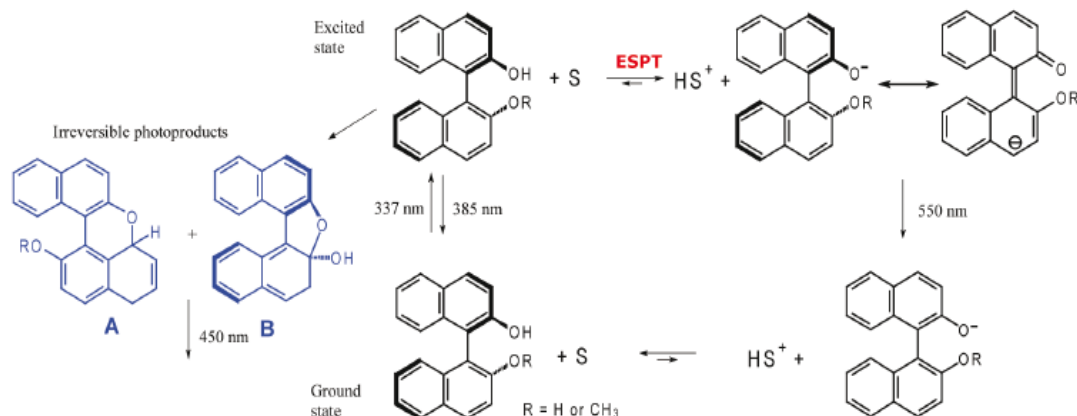


Figure 2.1 Photochemical processes in BINOLs, S is a proton acceptor.

The mechanism of A formation included intramolecular ESPT leading to a planar quinine methide structure, resulting in photoracemization. The mechanism for the formation of B was proposed to be an intramolecular addition of a phenolic OH group to a C-C double bond.

The purpose of this work was to study the ESPT from chiral proton donors to chiral and achiral acceptors, to look for the existence of an enantiomeric effect, and finally to compare the results with these endergonic ($\Delta G > 0$) reactions to the results with “super” photoacids where $\Delta G \ll 0$.

Experimental Protocols

R-(+)- and S-(-)-1,1'-bis-2-naphthol (BINOL), 2-hydroxy-2'-methoxy-1,1'-bi-2-naphthyl (MeBINOL), and 2,2'-dimethoxy-1,1'-bi-2-naphthyl (Me2BINOL) were obtained from Aldrich, SynChem, and Acros, respectively, in 99% purity. R-(+) and S-(-)-3,3'-diphenyl-2,2'-bi-1-naphthol (VANOL) and R-(-) and S-(+)-2,2'-diphenyl-3,3'-4-

biphenanthrol (VAPOL) were obtained from Aldrich in 97% purity. Dry toluene, acetonitrile, and methanol (<30 ppm, 10 ppm, and 50 ppm H₂O, respectively) were obtained from Acros. R-(-)- and S-(+)-1-cyclohexylethylamine and R-(-)- and S-(+)-*sec*-butylamines, 98% purity, were obtained from Aldrich. Photochemical reactions (non-deoxygenated) were performed in Pyrex glass (cutoff <300 nm) vials in a PRP-3000A Rayonet Reactor equipped with 300-nm lamps (emission spectrum centered at 300 nm with 100 nm full width) with a total intensity of 336 watts. Absorbance, fluorescence, and circular dichroism (CD) spectra were recorded on Perkin Elmer Lambda 19, Spex Fluorolog 2, and Jasco J17 spectrometers, respectively.

Samples were prepared from optically pure BINOLs and a measured amount of amine was added with a microsyringe. The samples were irradiated for up to 20 minutes, and aliquots of solution were removed from the photoreactor at fixed time intervals.

The circularly polarized luminescence (CPL) spectra were recorded, operating in a differential photon-counting mode.⁹ The light source for excitation was a continuous wave 450 W xenon arc lamp from a Spex Fluorolog-2 spectrofluorimeter, equipped with excitation and emission monochromators with dispersion of 4nm/mm (SPEX, 1681B). To prevent artifacts associated with the presence of linear polarization in the emission,¹⁰ a high-quality linear polarizer was placed in the sample compartment, and aligned so that the excitation beam was linearly polarized in the direction of emission (*z*-axis). The key feature of this geometry is that it ensures that the molecules that have been excited and that are subsequently emitting are isotropically distributed in the plane (*x,y*) perpendicular to the direction of emission detection.^{11,12} It is common to report the degree of CPL in terms of the luminescence dissymmetry factor, $g_{\text{lum}}(\lambda)$, which is defined as $g_{\text{lum}}(\lambda) =$

$2\Delta I/I = 2(I_L - I_R)/(I_L + I_R)$, where I_L and I_R refer to the intensity of the left and right circularly polarized emissions, respectively. A value of zero for g_{lum} corresponds to no circular polarization, while the absolute maximum value is 2. All the g_{lum} values reported in this work have been measured with a standard deviation of ± 0.0004 .

Results

Quick screening of Various Chiral and Achiral Proton Acceptors

In MeOH/H₂O 1/1 vol solutions, both R- and S-BINOLs demonstrated dual emission, with the dominant peak at 369 nm assigned to the neutral species and the weak emission at 550 nm assigned to the ESPT product (Figure 2.1), consistent with the weak photoacidity of BINOLs.¹³ Even weaker emission from the BINOLate anion was observed in saturated aqueous solutions of α -D-methylglucoside, a known chirality-inducing medium.¹⁴ The ESPT efficiency can be estimated from the steady-state emission data, since the apparent ESPT rate constant k_{PT} is directly proportional to the ratio of fluorescence quantum yields of the neutral, ϕ , and deprotonated, ϕ' , forms:¹⁵

$$k_{PT} = (\phi'/\phi)(k_f/k_f')/\tau'_0 \quad (\text{Eq. 2.1})$$

where k_f/k_f' is the radiative rate constant ratio for the neutral and deprotonated forms and τ'_0 is the fluorescence lifetime of the deprotonated form. Each curve in Figure 2.2 demonstrates BINOL in various chiral/achiral media.

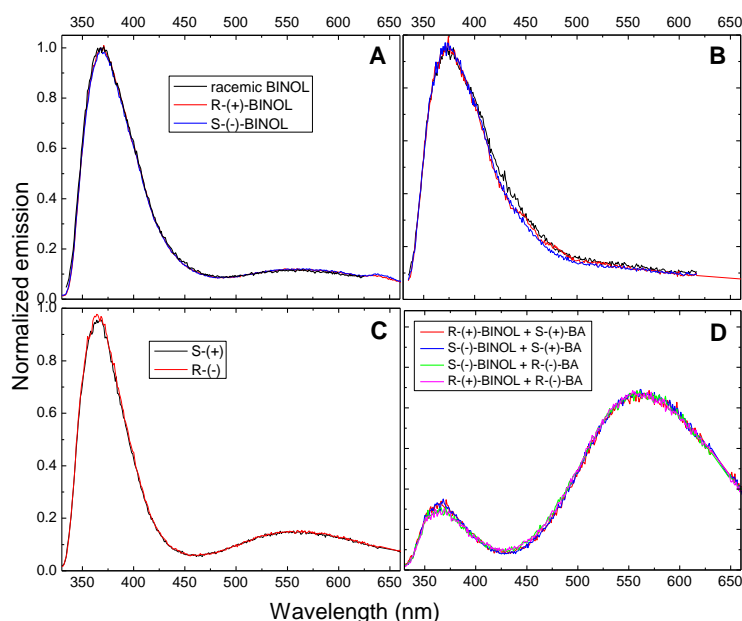


Figure 2.2. Enantioselectivity of BINOL in **A:** MeOH/H₂O 1:1 vol; **B:** Saturated aqueous α -D-methylglucoside; **C:** 0.11 M solution aminobutanol + S-(-)-BINOL in MeCN; **D:** 0.47 M solution sec-butylamine + BINOL in MeCN

In all systems studied, as represented in Figure 2.2, the ratio ϕ'/ϕ was independent of chirality for any proton donor-acceptor pair. Assuming k_f/k_f' independence and experimentally determined invariance of τ'_0 on the optical activity of BINOLs, these data demonstrate a total absence of enantiomeric effects on ESPT from BINOLs to both chiral and achiral proton acceptors. The fluorescence lifetimes of BINOLs in MeCN and toluene measured at the neutral emission band did not change upon addition of amines, indicating a static quenching mechanism.

While no enantioselectivity exists for ESPT from BINOLs to chiral amines, a comparatively large Stokes shift upon excited-state deprotonation is observed from BINOL over the well-studied 2N molecule.¹⁵ This large Stokes shift is indicative of a highly conjugated system, as explained by the planar resonance structure shown in Figure

2.1.⁶ This achiral intermediate has an equal probability to relax to either BINOL enantiomer, thus leading to racemization of the starting BINOL.

General Features of Spectra upon Photolysis

Steady-state absorption and emission of BINOL in various solvents in the presence of amines have been reported previously.⁴ The addition of amine to BINOLs solutions in various organic solvents resulted in a small bathochromic shift of the absorption band, presumably due to the formation of a ground-state hydrogen-bonded complex. The stability constant of the ground-state BINOL-amine complex has complicated solvent behavior,⁴ but in general, the magnitude of the complex is larger for non-polar, non-basic solvents. As a result, the ϕ'/ϕ ratio was larger for non-polar solvents at the same amine concentration. The efficiency of the ground-state hydrogen-bonded

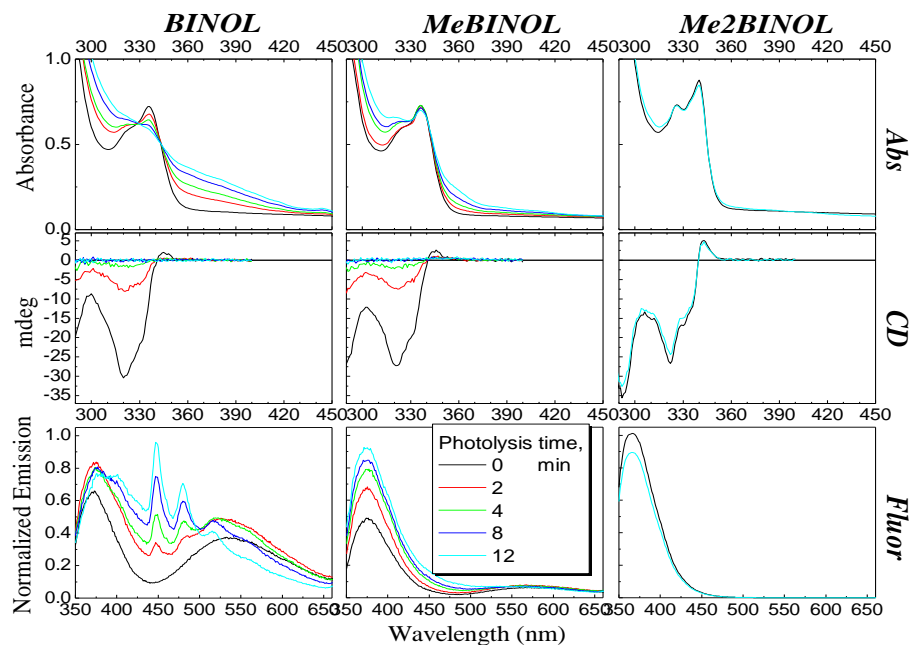


Figure 2.3 Photolysis of S-(-)-BINOLs in toluene + 0.04M 2-butylamine $\lambda_{ex}=337$ nm

complex formation and the ESPT was much lower for MeBINOL than for BINOL due to the extra OH moiety on BINOL. (Figure 2.3)

The nature of the proton acceptor affects the photochemistry of BINOLs. For BINOL and MeBINOL, the ϕ'/ϕ ratios for butylamine (0.795, 0.153, respectively)¹⁶ are much larger than for 1-cyclohexylethylamine (0.280, 0.046, respectively), indicating that 2-butylamine results in more efficient ESPT. This is most likely due to the structures of the proton acceptors, where CHE contains a bulky six-carbon ring causing steric hindrance. The dimethylether derivative, Me2BINOL, exhibited no ESPT and served as a control in all studies.

The results of typical photolysis experiments for BINOL, MeBINOL and Me2BINOL in organic solvents in the presence of proton acceptors are shown in Figure 2.3. Upon irradiation with 300-350 nm light, in the presence of an amine in toluene, the absorption spectrum of BINOL exhibited considerable degradation, complete loss of the characteristic absorption band at 337 nm, and appearance of a red-shifted absorbing structure-less shoulder. In tandem, the initially strong CD signal completely disappeared after 8 min of irradiation. The emission spectra demonstrated complex behavior upon photolysis with a new fine-structured emission band starting at 450 nm growing as irradiation time increased. MeBINOL demonstrated much less photodegradation and no new vibronic product was observed in the emission spectra. However, MeBINOL lost optical activity at the same rate as BINOL. Me2BINOL remained inert under these conditions, as was observed for the compound in organic solvents and their mixtures with water.⁴ Control experiments were performed in toluene without the presence of amine. In the absence of a proton acceptor, MeBINOL was photostable, and much slower

photoreactivity of BINOL was observed; the photolysis products in the latter case were the same as in the presence of amine. Similar results were observed in acetonitrile with CHE and BA. Both enantiomers of BINOL and MeBINOL behaved similarly upon irradiation, losing their optical activity at the same rate. In contrast to previous work⁶ that reported the photostability of BINOL in pure MeCN, a very slow photochemical reaction of BINOL was observed, perhaps due to the presence of residual water (10 ppm). Additional deoxygenation and dehydration by the freeze-pump-thaw technique of freshly prepared samples in anaerobic conditions lowered the decomposition rate even further.

Upon photolysis in the polar solvent methanol, both compounds produced an absorption maximum at 355 nm as well as a long wavelength band from 365 to 400 nm. In contrast to toluene, a shoulder appeared over a broader range of 350-400 nm. It is interesting to note that the emission spectrum of BINOL in a phosphate buffer at pH 6.9 reported by Xu and McCaroll¹⁷ exhibited an identical characteristic vibronic tail starting at 450 nm, most likely due to the photoreaction described previously.

In order to isolate the photoproduct from the fine-structured emission tail, HPLC separation was attempted of the BINOL photolysis reaction mixture in MeOH. Only one product was found using a UV-absorbance detector with an absorption maximum around 355 nm, identical to that reported earlier.^{6,8} The fluorescence spectrum resembled the parent BINOL compound, however the quantum yield was at least a factor of ten lower. The ¹H-NMR spectrum was identical to that of the photoproduct A reported by Fegel et al.⁶

Circularly Polarized Luminescence Studies

CPL spectroscopy, the emission analogue to CD spectroscopy, was used to further investigate the effect of adding chiral amines to BINOLs in toluene. Most importantly, the CPL studies were used to confirm that the loss of chirality of the BINOLs upon irradiation is in fact a consequence of efficient ESPT, as suggested by the CD experiments. If the ESPT in these systems occurs through a planar intermediate leading to photoracemization, one would expect that solutions of neutral chiral BINOLs would exhibit an active CPL signal, while the same solutions would lose CPL activity in the presence of chiral amines. It should be noted that all luminescent organic molecules that are chiral will exhibit a CPL signal, but the extent of circular polarization is almost always less than 1×10^{-2} .¹² Because of this, most of the CPL studies have been conducted on lanthanide(III)-based systems for which g_{lum} values as high as 1.38 were observed.⁹ As expected, the magnitude of the g_{lum} values for the two BINOL enantiomers, R-(+)- and S-(-)-BINOL, are small (-0.0011 and +0.009 at approximately 375 nm, respectively). These results confirm that the neutral BINOL solutions in toluene or MeCN exhibit an active CPL signal and also that the emitted light is polarized in opposite directions for the two enantiomeric forms of BINOL. In contrast, no CPL signal was detected for the racemic BINOL solution. It should be noted that the observation of a photochemical degradation occurring upon extended UV exposure prevented us from recording any CPL spectra for the various BINOL derivative-based systems studied. For this reason, g_{lum} values were only measured for sample solution at the maximum emission spectra over a short UV exposure period.

Unlike the CD measurements, the CPL experiments performed on the BINOL derivative solutions after addition of chiral amines were not conclusive. Since a considerable change in the intensity of the emission signals was observed after addition of a chiral amine to a R-(+)-MeBINOL solution (significant decrease of the emission band around 375 nm and appearance of a weak emission band around 500-550 nm), the required time for each g_{lum} value determined at the maximum of the emission bands corresponding to the neutral and deprotonated forms of MeBINOL (375 nm and 500-550 nm, respectively) was several hours of photon collection. As a result, no CPL signals were detected. These results suggest that in the presence of proton acceptors the BINOLs photoracemize and/or photochemically degrade faster than the CPL signal accumulation. To confirm this, CD spectra were recorded immediately before and after the CPL measurements were done. The CD signal around 322 nm of the MeBINOL solution in the presence of chiral CHE had completely disappeared during the long UV exposure required for CPL measurements. The loss of signal is attributed to a much longer signal accumulation (hours vs. minutes) and a more powerful xenon lamp (450 W vs. 150 W) used for CPL compared to CD, respectively.

Discussion and Conclusions

The discussion will begin with the “cleanest” case presented: the photoracemization of MeBINOL in a toluene/amine system (Figure 2.3). The loss of optical activity is almost complete after just 4 minutes of exposure; however, the absorbance and emission of any new photoproducts are still very weak. Since no photochemical transformation of MeBINOL was observed in pure toluene, this suggests

that *intermolecular* ESPT to amine via the formation of the planar structure suggested in Figure 2.1 is primarily responsible for the racemization. The yield of the irreversible photoproducts was much lower than that of photoracemization. The formation of the photoproducts in BINOL under the same conditions was more effective. It is hard to estimate relative contributions of the *intermolecular* ESPT and photoproduct formation, which may also include *intramolecular* ESPT,⁶ to the apparent photoracemization. However, taking into account the almost identical photoracemization rates for BINOL and MeBINOL and much slower photoracemization in the absence of amine, we conclude that the *intermolecular* ESPT is the major factor for BINOL racemization in the toluene/amine solvents (Figure 2.1). The photoracemization of atropisomeric diaryls is a known phenomenon and several mechanisms have been suggested¹⁸ in addition to those discussed here. However, analysis of the published data evidences that the *intermolecular* ESPT-induced photoracemization is the most efficient mechanism for this process.

Very weak fluorescence of the isolated product of BINOL photolysis and the similarity of the absorbance spectra for BINOL and MeBINOL photolysis products suggest that product A is formed preferentially (Figure 2.1) since product B would have more red-shifted optical spectra due to extended conjugation. The absence of formation of product B in the case of MeBINOL suggests that both protons must be involved in its formation. It is possible that an alternate *intramolecular* ESPT may give rise to intermediate C, which upon hemiketal formation and proton shift could result in the observed product (Figure 2.4). Such an *intramolecular* ESPT has been reported by Wan and coworkers for similar structures.⁶

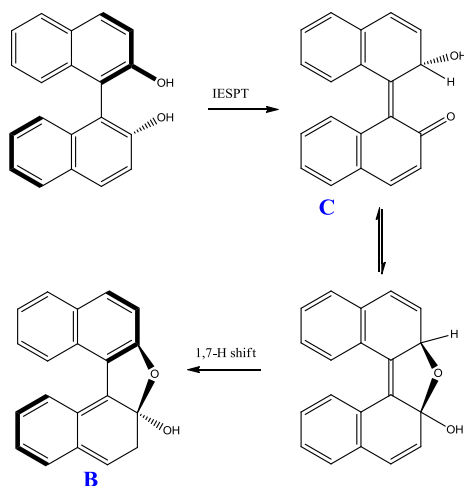


Figure 2.4 Mechanism of BINOL photocyclization.

Time resolved methods¹⁹ are in order to detect the proposed transient structure shown in Figure 2.1. Recent time-resolved CD measurements of Neizborala and Hache²⁰ demonstrated a 20-30° decrease of the dihedral angle in ethanolic BINOL solution. It is interesting that without an appropriate proton acceptor, full planarization is not achieved. This confirms the observation that photoracemization in pure alcohols is comparatively slow.

It is now possible to explain the lack of enantiomeric effects on the ESPT in the BINOL/proton acceptor system. Endergonic ESPT from the weak photoacids has a late transition state that should be similar to the product: planar *achiral* binaphtholate. Thus the geometry of the BINOLs in the ESPT transition state leads to photoracemization in the case of efficient ESPT. In contrast, assumption that the chirality of the transition state is preserved in the ESPT from the much stronger photoacid DCN2 to 2-butanol explains the enantiomeric effects observed for the DCN2 system.²

In order to generalize this phenomenon to other chiral ligands and to shed further light on the dynamic stereochemistry of chiral compounds, similar experiments were performed for the vaulted chiral compounds VANOL and VAPOL, but the results were unexceptional. While there was no enantioselectivity for all systems, substantial photodegradation was observed. VANOL readily decomposed to form an irreversible, fluorescent photoproduct in toluene and to a lesser extent in MeOH, leading to complete photoracemization. VAPOL also showed significant photodegradation and racemization in toluene; however, it was notably stable in MeOH. In the presence of proton acceptors, both compounds exhibited rapid decomposition. VANOL formed a fluorescent photoproduct incapable of ESPT, as could be observed by the loss of the dual emission to one single emission band. A non-fluorescent photoproduct was observed for VAPOL in all systems studied.

Unlike BINOL, VANOL and VAPOL are unstable in toluene and readily decompose as indicated by the loss in the characteristic absorption and emission bands, thus leading to complete isomerization. Presumably, this is the mechanism that leads to photoracemization. Photodegradation is the major process in the photolysis of these compounds. The formation of a substantial irreversible photoproduct is observed, and while the mechanism for this formation is still unclear, it is presumed to be similar to BINOLs due to the similar structure and photoacidity of the compounds.

In short, no significant ESPT enantioselectivity was observed between a given chiral BINOL and the optical isomers of the proton acceptors such as amines and aminoalcohols. In the presence of proton acceptors, BINOLs efficiently photoracemized, presumably through a planar intermediate. The dimethyl ether derivative incapable of

ESPT produced no appreciable racemization. No enantioselectivity was observed with the chiral ligands VANOL and VAPOL and photodegradation of the compounds dominated any other photochemical processes.

The exergonicity of the ESPT reaction and the transition-state position along the reaction coordinate plays the key role for the existence of enantiomeric effects in these systems. Enantioselectivity was observed for “super” photoacids ($\Delta G \ll 0$), but disappeared for endergonic reactions ($\Delta G > 0$) where the intermediate formed was similar to the planar achiral binaphtholate anion. As a result, photoracemization was observed, as confirmed by circular dichroism spectroscopy, and no diastereoselectivity was observed in a wide array of systems studied.

References

1. Solntsev, K.M.; Bartolo (Gould), E-A; Pan, G; Muller, G.; Bommireddy, S.; Huppert, D.; Tolbert, L.M. *Isr. J. Chem.* **2009**, 49, 227.
2. Solntsev, K.M.; Tolbert, L.M.; Cohen, B., Huppert, D.; Hayashi, Y.; Feldman, Yu. *J. Am. Chem. Soc.* **2002**, 124, 9046.
3. Recent reviews: (a) Pu, L. *Chem. Rev.* **2004**, 104, 1687. (b) Speranza, M.; Satta, M.; Piccirillo, S.; Rondino, F.; Paladini, A.; Giardini, A.; Filippi, A.; Catone, D. *Mass Spec. Rev.* **2005**, 24, 588. (c) Alkorta, I.; Picazo, O.; Elguero, J. *Curr. Org. Chem.* **2006**, 10, 695. (d) Zehnacker, A.; Suhm, M.A.; *Angew. Chem., Int. Ed.* **2008**, 47, 6970.
4. Iwanek, W.; Mattay, J. *J. Photochem. Photobiol. A.* **1992**, 67, 209.

5. Shi, Y.; Wan, P. *Chem. Commun.* **1997**, 273.
6. Flegel, M.; Lukeman, M.; Wan, P. *Can. J. Chem.* **2008**, 86, 161–169.
7. The preliminary results including the photoracemization scheme (Figure 1) were reported in parts at the following American Chemical Society National meetings: 225th, New Orleans (2003), PHYS 357; 229th, San Diego (2005), PHYS 456; 233th, Chicago (2007), PHYS 45; 234th, Boston (2007), PHYS 364.
8. a) Cavazza, M.; Zandomeneghi, M.; Ouchi, A.; Koga, Y. *J. Am. Chem. Soc.* **1996**, 118, 9990. (b) Ouchi, A.; Zandomeneghi, G.; Zandomeneghi, M. *Chirality* **2002**, 14, 1.
9. Lunkley, J.L.; Shirotani, D.; Yamanari, K.; Kaizaki, S.; Muller, G. *J. Am. Chem. Soc.* **2008**, 130, 13814, and references therein.
10. Dekkers, H.P.J.M.; Moraal, P.F.; Timper, J.M.; Riehl, J.P. *Appl. Spectrosc.* **1985**, 39, 818.
11. Field, J.E.; Muller, G.; Riehl, J.P.; Venkataraman, D. *J. Am. Chem. Soc.* **2003**, 125, 1808.
12. Riehl, J.P.; Muller, G. In *Handbook on the Physics and Chemistry of Rare Earths*; Gschneidner, K.A., Jr.; Bünzli, J.-C.G.; Pecharsky, V.K., Eds: North-Holland Publishing Company: Amsterdam, **2005**; Vol. 34, Chapter 220, pp 289–357, and references therein.
13. Ismail, L.F.M.; Abdel-Mottaleb, M.S.A. *Int. J. Photoenergy* **2003**, 5, 249.
14. (a) Foher, B.; Savelli, G.; Torri, G.; Vecchio, G.; McKenzie, D.C.; Nicoli, D.F.; Bunton, C.A. *Chem. Phys. Lett.* **1989**, 158, 401. (b) Capozzi, G.; Ciampi, C.; Delogu, G.; Menichetti, S.; Nativi, C. *J. Org. Chem.* **2001**, 66, 8787.

15. Weller, A. *Prog. React. Kinet.* **1961**, *1*, 187.
16. Presented are the relative fluorescence intensity ratios I_0/I .
17. Xu, Y.; McCarroll, M. *J. Photochem. Photobiol. A* **2006**, *178*, 50–56.
18. (a) Irie, M.; Yoshida, K.; Hayashi, K. *J. Phys. Chem.* **1977**, *81*, 969. (b) Burnham, K.S.; Schuster, G.B. *J. Am. Chem. Soc.* **1998**, *120*, 12619. (c) Hattori, T.; Shimazumi, Y.; Yamabe, O.; Koshiishi, E.; Miyano, S. *Chem. Commun.* **2002**, 2234.
19. Augulis, R.; Klok, M.; Feringa, B.L.; van Loosdrecht, P.H.M. *Phys. Stat. Sol. (C)* **2009**, *6*, 181.
20. Niezborala, C.; Hache, F. *J. Am. Chem. Soc.* **2008**, *130*, 12783.

CHAPTER 3

DESIGN, SYNTHESIS, AND PROPERTIES OF A NOVEL

“SUPER” PHOTOACID, *N*-METHYL-6-HYDROXYQUINOLINIUM (MHQ)

Part I: Synthesis and General Characterization

Introduction

As stated previously, electronic redistribution in the excited state causes the pK_a jump observed for photoacids. Careful analysis of the HOMO/LUMO-based electronic distribution in the molecules reveals the positions of increased electron density in the excited state. From these calculations and experimental results, it has been shown that photoacidity is increased by placing electron-withdrawing groups (EWG) on these atoms.¹ It was reported that substituting electron-withdrawing nitriles into the 5- and 8-positions of 2N decreased the pK_a^* from 2.5² for 2N to approximately -4.5 for 5,8-dicyano-2-naphthol (DCN2, Figure 3.1).³

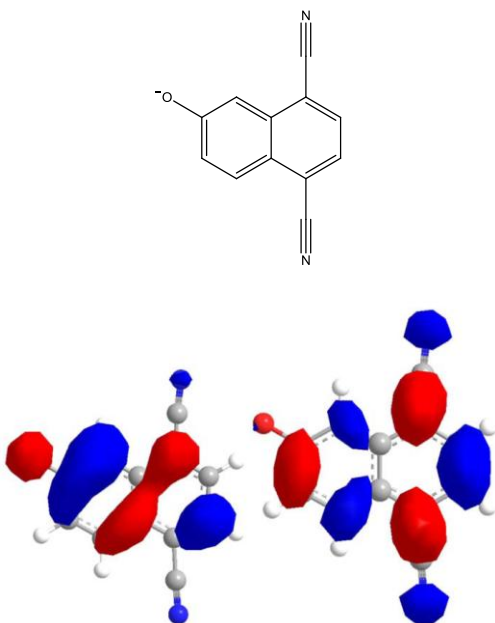


Figure 3.1 Structure and HOMO/LUMO orbital diagrams of DCN2. Calculated using semi-empirical method AM1.^{1b}

Until recently, DCN2 was the strongest photoacid reported with a drop of approximately 13 pKa units.¹ The Tolbert Group has developed several “super” photoacids that allow proton transfer to be studied on an ultrafast timescale.^{1,3} In attempts to avoid ionic compounds, they considered the N-oxides of hydroxyquinolines.⁴ However, the pK_a^* s of these compounds were not low enough and they also underwent additional photochemistry. Still in search for stronger photoacids, this research has focused on investigating aryl systems with strong electron-withdrawing substituents. The initial aim of this project was to explore various salts of 6-hydroxyquinoline (6HQ) in which quaternary nitrogen acts as a strong electron-withdrawing group. Thus, *N*-methyl-6-hydroxyquinolinium (MHQ, Figure 3.2) salts were synthesized.

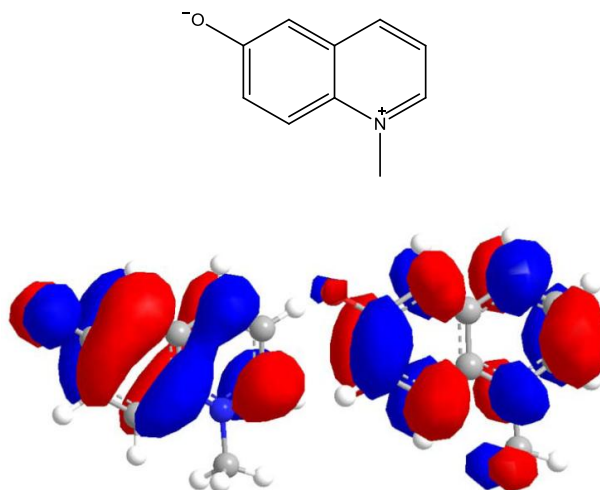


Figure 3.2 Structure and HOMO/LUMO orbital diagrams of MHQ. Calculated using semi-empiric method AM1.^{1b}

Studies report that 6HQ in the cationic form can undergo deprotonation in the excited state even in 10M perchloric acid solutions, making it an extremely strong photoacid.⁵ In addition to showing enhanced acidity in the excited state, the nitrogen on the pyridine ring of 6HQ is capable of accepting a proton in 12M NaOH solutions, making it a very strong photobase.⁵ This photobasicity is the major drawback to utilizing 6HQ in acid-generating capacities. The problem can be overcome by blocking of the basic nitrogen by alkylation and creating a quaternary ammonium salt. Not only does this prevent the nitrogen from accepting a proton, but it also adds a group with an extremely large Hammett substituent constant, σ , to the molecule.⁶

MHQ and its derivatives have been known for some time. Some of them exhibit significant biological activity, making them promising pharmacological agents.⁷ Schulman and Fernando reported the steady-state spectral properties of MHQ-CH₃SO₃ in 1968.⁸ The negative solvatochromism of MHQ-I was demonstrated by Bardez et al. in 1994 and was explained by an intramolecular charge transfer leading to a less dipolar

excited state than ground state.⁵ The authors suggested the presence of two excited-state resonance forms of MHQ: a charge-separated zwitterionic species and a charge-delocalized quinoid-type species. A long-chain derivative of MHQ was used as pH-indicator in microheterogeneous systems.⁹ A few studies on the ESPT kinetics of MHQ have been reported. Kim and Topp studied the ultrafast decay of MHQ and claimed that the observed decay on the picosecond timescale was due to adiabatic electron transfer from the excited-state zwitterion (Z^*) to the quinoid-type structure.¹⁰ Kovalenko et al. reported a similar effect; however, they attributed these short-time dynamics to solvent relaxation.^{11,12} They found the ESPT activation barrier in neat protic solvents to be ~ 2 kJ/mol. The authors also claimed that no intramolecular electron transfer occurs for Z^* and attributed the lack of back proton-transfer to solvent stabilization. Kovalenko et al. further stated that in acetonitrile-water mixtures the ESPT occurs in two timescales: fast (solvation controlled) and slow (diffusion controlled). MHQ was claimed to undergo slow but detectable intermolecular ESPT in a matrix of poly(2-hydroxyethyl methacrylate).¹³ It is also worth noting several other cationic hydroxyaromatic photoacids exhibiting a very strong photoacidity: hydroxyphenylpyridinium,¹⁴ 8-hydroxyacridizinium,¹⁵ hydroxycarboxyflavylium,¹⁶ and cyanine fluorochromes.¹⁷

There are no reports to-date on counteranion effects on the ESPT in the MHQ ionic systems. Aromatic organic salts with counteranion substitutions that do not exhibit ESPT generally only differ in physical properties¹⁸ and in the rate of photobleaching;¹⁹ changes in the ESPT dynamics have not been noted. Further, there have been few reports of the ESPT dynamics of MHQ in nonaqueous environments.

Experimental Protocols

Materials. 6-Hydroxyquinoline (98%), 6-methoxyquinoline (98%), methyl iodide and the silver salts of hexafluoroantimonate, triflate, hexafluorophosphate, tetrafluoroborate and bis(trifluoromethylsulfonyl) amide were purchased from Acros and used without further purification. Methyl trifluoromethanesulfonate (99%) and methyl nonafluorobutanesulfonate (99%) were purchased from Synquest Laboratories and used without further purification.

Synthesis. One molar equivalent of the appropriate quinoline and 1.1 molar equivalent of the desired methylating agent were dissolved in dry acetone (dried over potassium carbonate). The reaction was heated at 70°C for 4 hr in a heating block. After the reaction was complete, the products were precipitated with diethyl ether and filtered. If necessary, the products were dissolved in hot ethanol and hot-filtered from activated carbon and, finally, recrystallized using a binary ethanol-ether mixture. If needed, anion metathesis was performed in water with silver salts containing the desired counterion. Tetrafluoroborate, hexafluorophosphate, hexafluoroantimonate and bis(trifluoromethylsulfonyl) amide containing silver salts (1.1 eq) were stirred with one molar equivalent of MHQ-Br in deionized water. The mother liquor was recovered after filtration of the insoluble AgI, and the water was removed with a rotary evaporator. After dissolving the precipitate in ethanol, the salts were hot-filtered over activated carbon and filtered to remove remaining trace amounts of silver. Recrystallization was from ethanol-ether. All samples were dried for 24 h at 110°C in vacuo over P₂O₅.

Instrumentation. Nuclear magnetic resonance spectra were recorded on a Varian Gemini 300 MHz spectrometer, in acetone-d₆. Mass spectra were obtained by the Georgia

Institute of Technology Bioanalytical Mass Spectrometry Facility on a Micromass AutoSpec spectrometer. Low-resolution electron ionization (EI, 70 eV) spectra were collected at 400 K. Melting points were taken with an Electrothermal capillary melting point apparatus and are reported uncorrected. The organic solvents were used as received from commercial sources without further purification.

Uv-Vis absorption spectra were taken on a Perkin Elmer Lambda 19 and fluorescence measurements were done using a Horiba Jobin Yvon Fluorolog 2 Spectrophotometer. Fluorescence spectra were collected at a right angle from the excitation source. The excitation source was a 1000 W high-pressure Hg-Xe lamp. Entrance and exit slits were set to 1.5 mm. All spectra were collected in quartz cuvettes. Fluorescence emission spectra were excited at the maximum absorption wavelength.

Results

Synthesis of N-methyl-6-hydroxyquinolinium salts

The synthesis of MHQ and MMQ was previously reported in the Tolbert Laboratory.^{1b} The materials were synthesized in good yield using 6-hydroxyquinoline and 6-methoxyquinoline, respectively. The synthetic pathway for the reaction is shown in Figure 3.3.

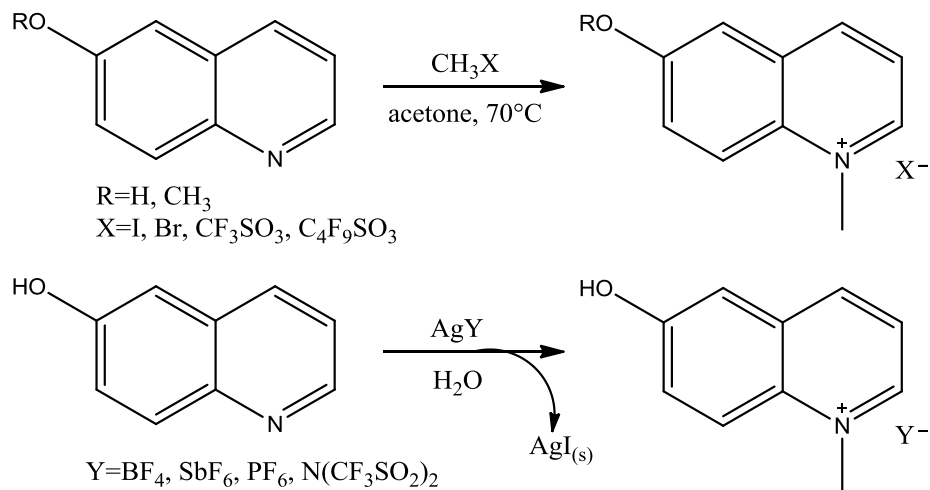


Figure 3.3. Synthetic pathway for preparation of MHQ salts.

The materials were synthesized using a procedure modification of the literature procedure.¹⁰ Acetone was substituted for the literature precedent toluene to favor precipitation of the final products from solution while keeping unreacted reagents soluble. For the anion metathesis, silver salts were chosen because metathesis with sodium and potassium salts did not lead to any observable exchange, most likely due to the similar solubility of KBr, NaBr and MHQ-Br in common organic solvents.

Examination of general spectral characteristics

The absorption spectra of MHQ-Nf in BuOH and DMSO are shown in Figure 3.4. Absorption of the ground-state cationic species, C (AH, Figure 1.1), has a maximum wavelength at around 360 nm. The absorption spectrum did not change by varying the counteranion; however, these salts did exhibit a small solvatochromatic effect. Some ground-state deprotonation resulted in the broad absorption band of the zwitterion, Z (A⁻,

Figure 1.1), centered at 420 nm and the narrow band around 275 nm.

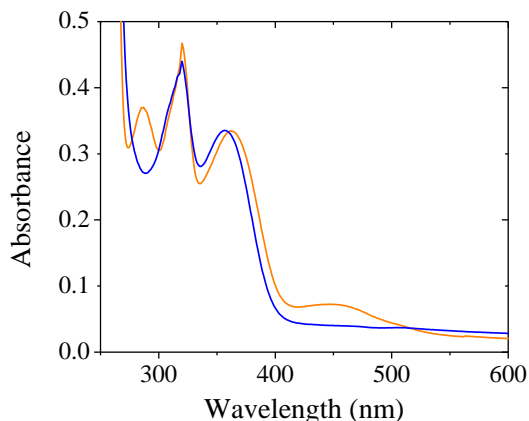


Figure 3.4. Uv-vis absorption spectra of MHQ-Nf in BuOH (orange) and DMSO.

Figure 3.5 shows the steady-state emission spectra of the MHQ salts, with the most dramatic spectral differences seen in BuOH and DMSO. Varying the counteranion and the solvent produces much different emission profiles. In protic solvents, the steady-state emission is heavily counteranion-dependent, with the Nf salt showing the most emission from Z^* (A^* , Figure 1.1) while the weaker-coordinating SbF_6^- and BF_4^- show

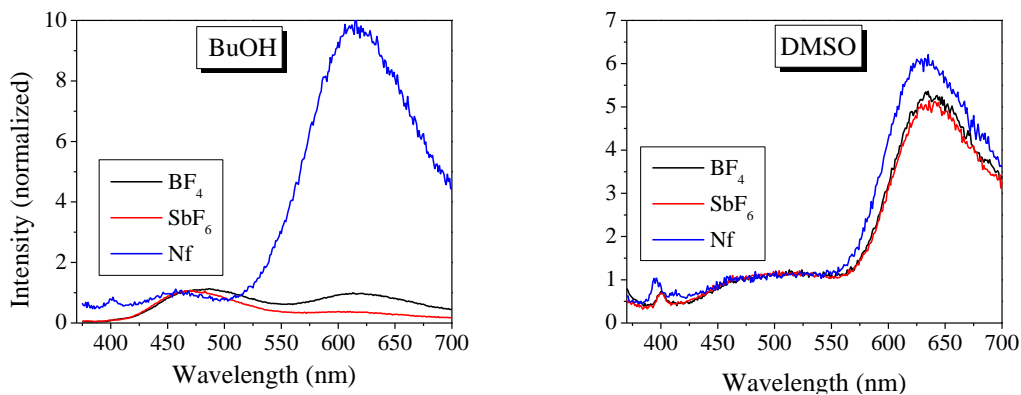


Figure 3.5. Steady-state emission spectra of various MHQ- BF_4 (black), SbF_6 (red), and Nf(blue) salts in BuOH (left) and DMSO (right) Normalized to 460 nm. $\lambda_{ex}=358$ nm.

diminished Z* emission. In aprotic solvents, such as DMSO, the counteranion effect disappears. The emission of MHQ was measured in a variety of organic solvents and solvent mixtures. The fluorescence is heavily quenched by all proton-accepting solvents. This will be addressed in further detail in Chapter 5.

Discussion and Conclusions

MHQ salts were synthesized according to the modified procedure that favored insolubility of the final products over 10-15% yield decrease. The compounds were easily purified, resulting in white solids that had good solubility in most organic solvents studied.

The ground-state cation and zwitterion absorb at approximately 360 and 450 nm, respectively. Consistent with the observation by Bardez et al.,⁵ these salts exhibit a small negative solvatochromism (Table 3.1); that is, the absorption maximum increases with decreasing solvent dielectric constant.

Table 3.1. Solvatochromism of MHQ-Nf.

Solvent	$\lambda_{\text{max}}(\text{nm})$
Methanol	358
Ethanol	362
Propanol	362
CH ₃ CH _n OH(n=3-7)	364
DMSO	357

This effect can be attributed to the decreased dipole moment in the excited state: in less polar solvents there is a decrease in energy between the ground and excited states. In acetonitrile/water mixtures, the absorption maximum does not change considerably with

increasing water concentration; however, significant ground-state deprotonation is observed. As expected, the absorbance spectra are independent of counterion, indicating that the counterion does not affect the ground-state of the MHQ.

The fluorescence decay pathways for MHQ salts are shown in Figure 3.6. Upon excitation, the ground-state cation (C) forms the excited-state cation (C*), which can then undergo deactivation through emission at approximately 460 nm. If ESPT occurs, the excited-state zwitterion (Z*) is formed, which can then undergo fluorescence at approximately 610 nm.

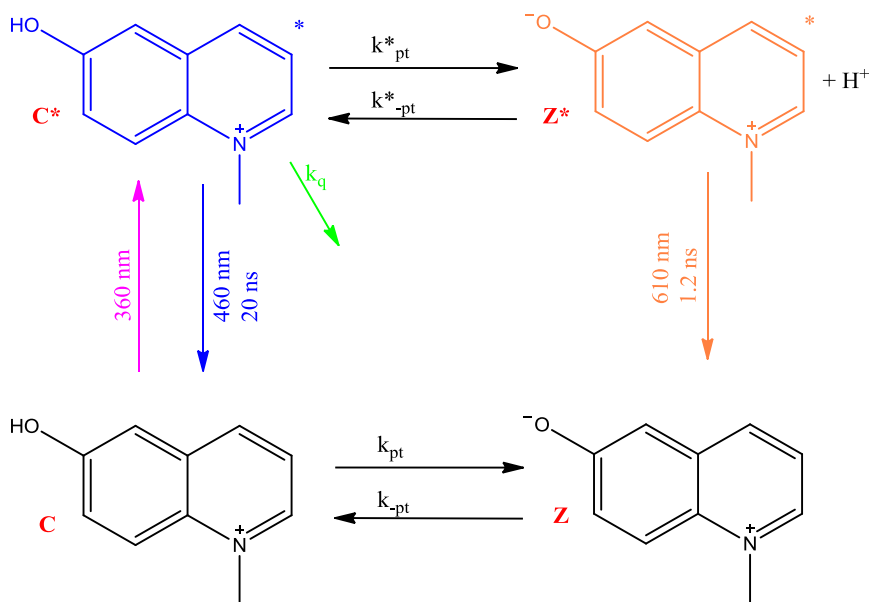


Figure 3.6. Fluorescent pathways of MHQ salts.

The counteranion effect on the fluorescence is dramatic in hydroxylic solvents. The effects of the counteranion have been explored, but have not been fully explained. As discussed in Chapter 2, the ESPT efficiency can generally be estimated from steady-state

emission data (Eq 2.1), so it appeared that the ESPT rate is dramatically affected by the counteranion. Time-resolved measurements were performed to determine the counteranion effects on the proton transfer rate and will be discussed in the next section of this chapter. Experiments investigating aggregation using dynamic light scattering (DLS) indicate that the spectral dependence on the counteranion is not a result of aggregation. In order to further rule out aggregation, dilution experiments were performed; however, ESPT was shown to be independent of photoacid concentration. Passing spectroscopic solutions through 200 nm filters does not affect the Z^*/C^* ratio; i.e., if any aggregates are present, their size is under 200 nm. It should be noted, however, that the DLS experiments do show some increase in scattering with concentration, although it does not correlate with the differences in emission profiles and could have been due to the low solubility of the less hydrophobic salts in alcohols. Ion pairing was studied by adding excess counteranion and shifting the equilibrium of the system far to the left. In all systems studied, the concentration of the counteranion did not affect ESPT dynamics. Either a bound contact-ion pair is already formed, or conversely, a solvent-separated ion pair forms immediately and increasing the concentration of the anion does not affect these processes.

Part II: Excited-State Proton Transfer Kinetics of MHQ Salts:

Experiment and Theory*

*This section was heavily drawn from (a) Gould, E.-A.; Popov, A.V.; Tolbert, L.M.; Presiado, I.; Erez, Y.; Huppert, D.; Solntsev, K.M. Excited-state Proton Transfer in *N*-methyl-6-hydroxyquinolinium Salts: Solvent and Temperatures Effects. *Phys. Chem. Chem. Phys.* **2012**. DOI: 10.1039/C2CP23891H (b) Popov, A.V., Gould, E.-A., Salvitti, M.A.; Hernandez, R.; Solntsev, K.M. Diffusional effects on the reversible excited-state proton transfer. From Experiments to Brownian dynamics simulations. *Phys. Chem. Chem. Phys.* **2011**, 13, 14914.

Introduction

Eigen first proposed a two-step reaction mechanism for protolytic photodissociation, where the first step includes reversible formation of the conjugate base into a contact ion pair and the second step includes diffusional separation of the contact-ion pair.²⁰ Depending on pH, the time evolution of the excited species involved in this scheme can be described by mono- or biexponential decay.²¹ However, in 1986 Pines and Huppert²² first noted the non-exponential decay behavior of 8-hydroxypyrene-1,3,6-trisulfonic acid (HPTS). They explained this phenomenon using the geminate recombination (GR) scheme (Figure 3.7).

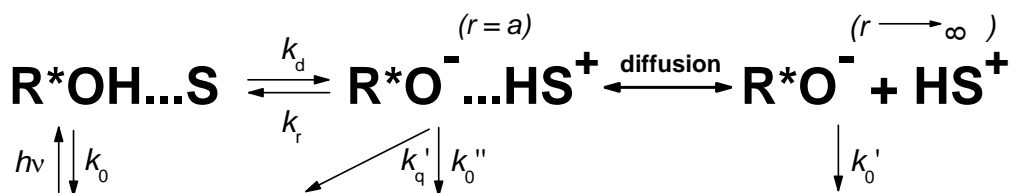


Figure 3.7. Geminate recombination reaction scheme.

In the GR model, the photoprotolytic cycle is still subdivided into two consecutive steps after excitation: reaction and diffusion. The first step is a rapid proton transfer creating a solvent-stabilized ion pair ($R^*O^- \dots HS^+$), followed by the diffusive step in which the proton and the anion diffuse from each other due to the random thermal motion of each

species. The reverse process is the adiabatic GR of the proton with the anion. Therefore, GR from the geminate proton reconstitutes the bound excited state (R^*OH), leading to the non-exponential decay observed in these systems. Pines and Huppert suggested that dissociation and GR of the proton occur consecutively and reversibly following the initial dissociation from the photoacid, forming a “geminate ion pair”.^{22a} A true equilibrium cannot be established, and therefore true exponential decays are not observed. For the ESPT reaction, *ROH typically decays faster than $^*RO^-$, allowing for the diffusional effects to progress, which then leads to a $t^{-3/2}$ asymptotic power-law decay for the *ROH time-resolved fluorescence.²³ The nature of this decay stems from the proton diffusion that is a random walk in 3-dimensional space.

In search of analytical solutions to the proton dissociation kinetics in photoacids, Pines, Huppert, and Agmon^{23a} analyzed the problem using the Debye-Smoluchowsky equation (DSE).²⁴ This model assumes that diffusion of a dissociated geminate proton is random motion in the field of the anion and allows the pK_a^* of photoacids to be estimated from one kinetic measurement at neutral pH and is described using Eq. 3.1: where a is the contact distance, k_d and k_r are the dissociation and recombination rates, respectively, and R_D is the Debye radius.

$$pK_a^* = -\log \frac{k_d \exp(-R_D/a)}{k_r} \quad (\text{Eq. 3.1})$$

While the DSE can be a useful tool to describe analytically the evolution of the excited photoacid and its conjugate anion, in many cases no analytical solution exists, so the Spherically Symmetric Diffusion Problem (SSDP) application, developed by Krissinel and Agmon, is employed to solve the problem numerically.²⁵ The SSDP

program solves a spherically symmetric diffusion problem using two coupled DSEs, which are needed to describe the time evolution of two electronic states; that is, the excited-state acid and its conjugate base.

The SSDP approach is both fast and accurate and has been used successfully for various photoacids in varying systems.²⁶ Unfortunately, the scenario that describes the reversible ESPT from MHQ is more complicated than others previously studied. The time-dependent charge interaction between Z^* and the proton is not trivial. The force field of a complex of the zwitterion and counteranion is (i) dynamic owing to a moving counteranion, and (ii) anisotropic due to a strong dipole nature of the conjugate base. Because of the high anisotropy of the system, it is not possible to use SSDP to accurately describe the kinetics of this system.^{23a} It is this problem that led to modeling the proton transfer kinetics of the MHQ system using Brownian Dynamics simulations.

Experimental Protocols

Room-temperature time-correlated single photon counting (TCSPC) measurements were taken using a LifeSpec TCSPC setup with a picoseconds pulse diode laser providing 372 nm excitation. A high speed microchannel plate Hamamatsu 3809U photomultiplier tube cooled to -20°C to reduce dark counts (noise) was used to detect the incoming photons. The pulses were communicated to the hardware controller by a constant fraction discriminator (CFD). A second CFD was used to obtain a timing reference pulse from the light source. The amplified signal was fed to an analog-to-digital converter. The instrument response function (IRF) of the setup was obtained using

titanium dioxide and non-dairy creamer dissolved in water to act as a light-scattering sample.

Low-temperature TCSPC measurements were performed using excitation from a cavity dumped Titanium:Sapphire femtosecond laser, Mira Coherent, which provides short, 80 fs pulses at approximately 800 nm. The laser third harmonic (THG), operating over the spectral range of 260-300 nm, was used to excite the samples. The cavity dumper operated with a relatively low repetition rate of 500 kHz. The TCSPC detection system was based on a Hamamatsu 3809U photomultiplier and Edinburgh Instruments TCC 900 computer module for TCSPC. The overall instrument response was approximately 35 ps (full width half maximum, FWHM) where the excitation pulse energy was reduced to about 10 pJ by neutral density filters. The temperature of the irradiated sample was controlled by placement in a liquid N₂ cryostat with a thermal stability of approximately 1.5 K.

All of the TCSPC data were fit using the Spherical Symmetric Diffusion Problem (SSDP) program, developed by Krissinel and Agmon and implemented in our laboratory.^{23a} The effective potential derived in this work, discussed below, was used as the potential input for SSDP.

Ultrafast kinetic measurements were performed using the fluorescence upconversion technique with femtosecond resolution. The samples were excited using a Titanium:Sapphire femtosecond laser, Mira Coherent, which provides short, 120 fs, pulses. The second harmonic, between 380-420 nm, was used to excite the solutions. The upconversion system (FOG-100, CDP, Russia) operated at 76 MHz. Excitation pulses were approximately 20 mW at the second-harmonic generation (SHG) frequency.

The fluorescence upconversion data were fit using the FFIT program, written by N. Tkachenko in 1995 in which the spectra are corrected according to the IRF. The fitting error is embedded in the number of significant figures and is between 5-10% for all lifetime values. All organic solvents were used as received from commercial sources without further purification.

The upconversion measurements and TCSPC measurements with the cryostat were taken in the laboratory of Dr. Dan Huppert at Tel Aviv University in Tel Aviv, Israel.

Results

ESPT kinetics in the picosecond to nanosecond regime

The time-resolved emission spectra shown in Figure 3.8 correlate well with the steady-state spectra discussed in Part I. Decays at 460 nm correspond to C* and show multi-exponential decays that in protic solvents depend on the counteranion (Figure 3.8,

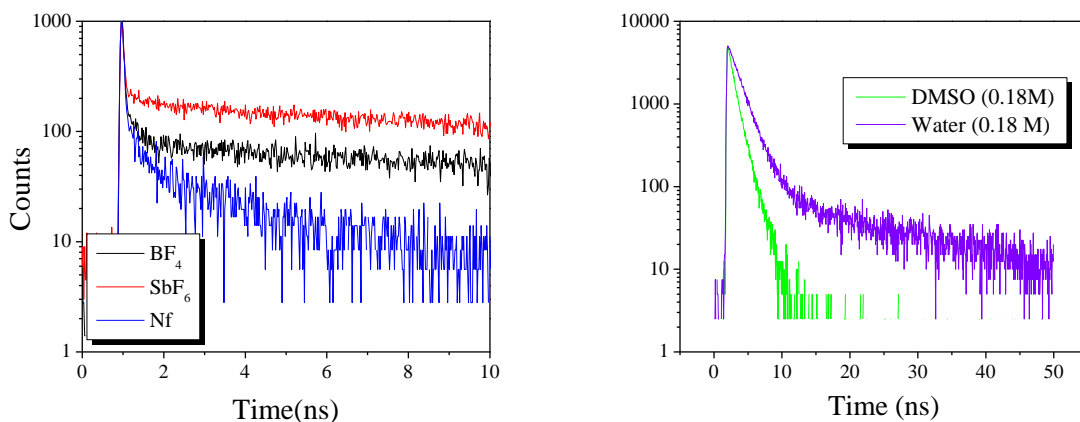


Figure 3.8. Left: Time-resolved decay curves monitored at 460 nm for MHQ-BF₄(black), SbF₆(red), and Nf(blue) salts in BuOH Right: Decay curves monitored at 460 nm for MHQ-Nf in MeCN/DMSO (green) and MeCN/water (purple) (0.18 M DMSO and water).

left). At this time resolution, it appears that for all compounds, an initial fast decay of 20 ps occurs suggesting an independence of k_{pt} on the nature of the counteranion. Decays at 610 nm (bottom), corresponding to Z^* , are single-exponential with a lifetime of 1.2 ns in BuOH. A long-lifetime tail of 20 ns is observed at 460 nm, which accounts for ~10% of the overall decaying species for the SbF_6 and BF_4 salts. This long-lifetime species is present only in protic solvents, where in aprotic solvents, such as DMSO, it is diminished (Figure 3.8, right). Finally, the decays in DMSO are faster than the decays in water for the same concentration of DMSO and water.

ESPT kinetics in the femtosecond to picoseconds regime

The ultrafast ESPT kinetics in various short-chain alcohols are shown in Figure 3.9 (left). The average decay is longer as the alcohol chain-length increases where the average lifetimes are 11, 20, 35, and 76 ps for MeOH, EtOH, PrOH, and BuOH, respectively. For EtOH and PrOH, the fast component is nearly indistinguishable.

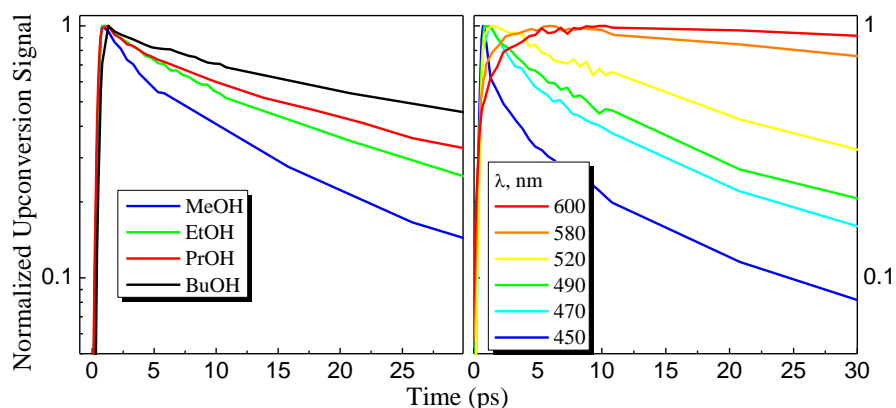


Figure 3.9. Fluorescence upconversion of MHQ-Nf in various alcohols (left) and in EtOH monitored at various wavelengths (right).

Figure 3.9 (right) shows the wavelength-dependence on the ultrafast decays in MHQ in EtOH. The amplitude of the short time decreases with increasing wavelength and the overall decay exhibits faster kinetics at shorter wavelengths.

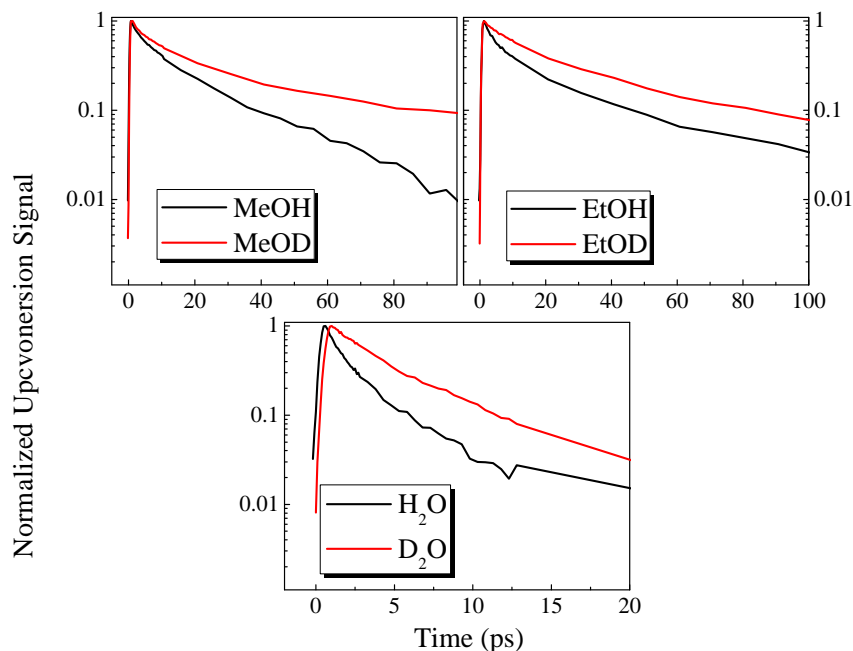


Figure 3.10. H/D isotope effect on the ESPT of MHQ in MeOH/D (top left), EtOH/D (top right) and H/D₂O.

The deuterium isotope effect on the ESPT rate was studied and can be seen in Figure 3.10 for MeOH/D, EtOH/D and H/D₂O. The decays of water, MeOH, and EtOH show an isotope effect calculated to be 1.4, 1.6, and 1.9, respectively, indicating that recombination is slower in deuterated versus fully hydrogen-rich solvents. To confirm that the proton transfer is independent of counteranion, upconversion measurements were done using Nf and BF₄ salts. Their lifetimes in EtOH were found to be 17.6 and 17.8 ps, respectively, verifying that the primary protolytic photodissociation step is unaffected by counteranion. As noted in the experimental protocols, a preferential solvation by water

was observed. As expected by the relative lifetimes, the decays are faster when water is present in the system. It was therefore necessary to be vigilant about water content and ensure the dryness of all solvents. The lifetimes for all systems studied are presented in Table 3.4.

Temperature dependence on the ESPT rate

Figure 3.11 shows the time-resolved emission measured by TCSPC of the R^*OH/C^* species of DCN2 and MHQ in ethanol at temperatures from 173-297 K. The R^*OH/C^* decay rate of MHQ is faster than DCN2 at all temperatures above 173 K. The

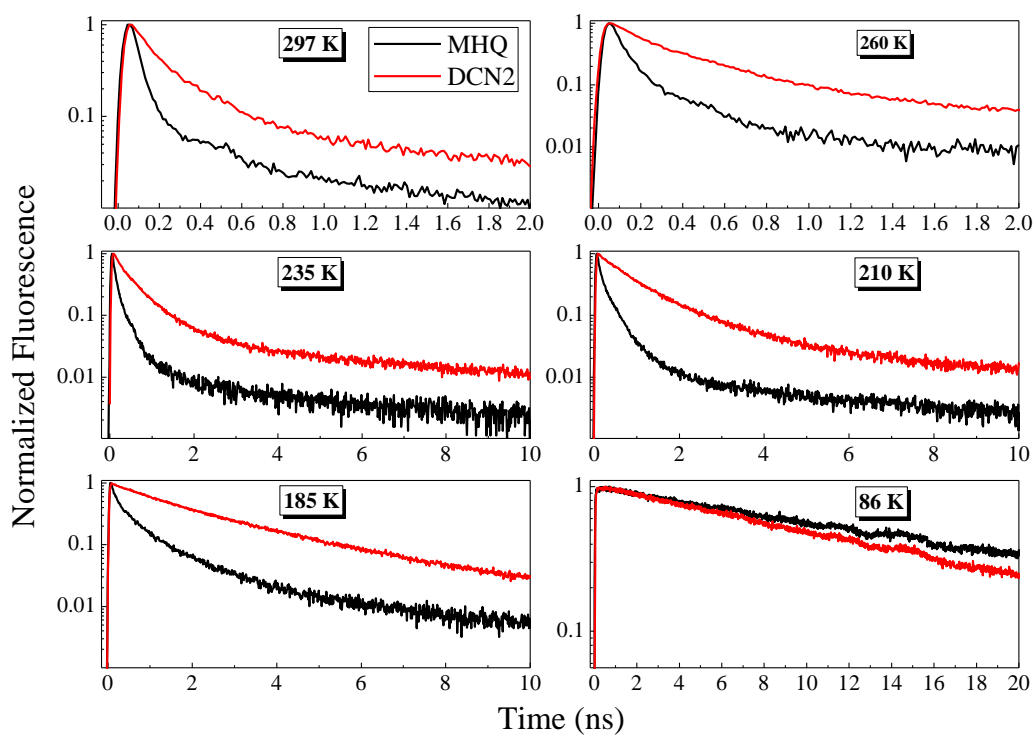


Figure 3.11 ROH*/C* decays of DCN2(red)/MHQ(black) in EtOH at temperatures from 86K-297K.

phase transition to solid occurs for EtOH at approximately 173 K at which point the decay rate decreases dramatically and is approximately the same from 80-170 K. The C^* decay for MHQ is even slightly slower than the R^*OH decay for DCN2 (see 86 K, Figure 3.11).

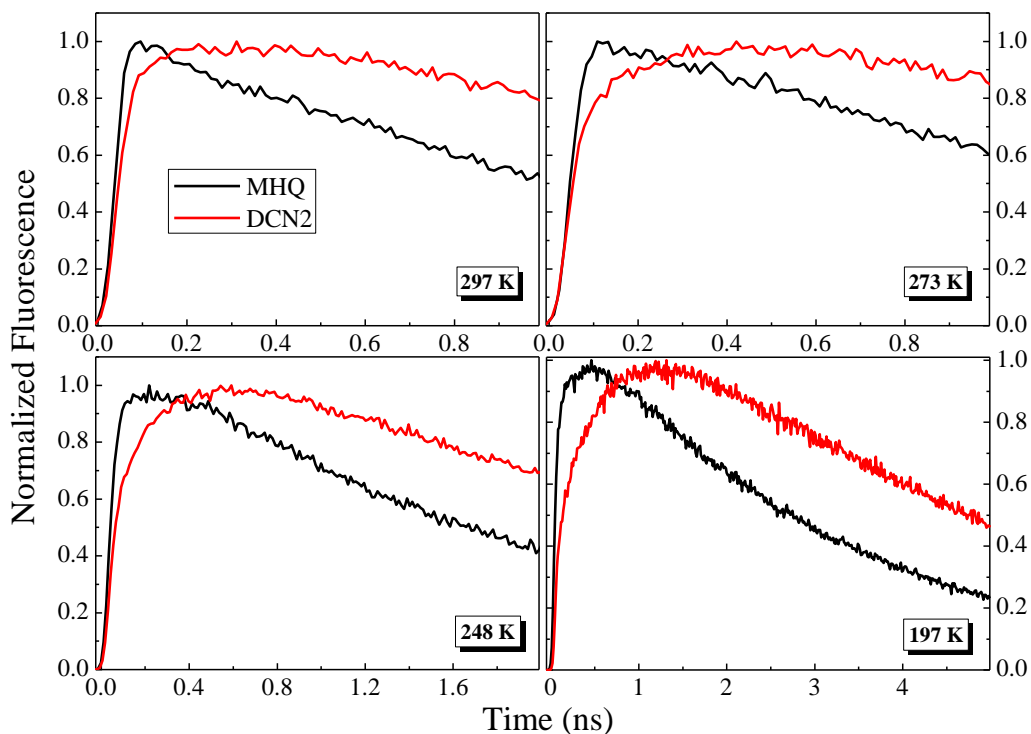


Figure 3.12 RO^*/Z^* decays of DCN2(red)/MHQ(black) in Ethanol at temperatures from 197K-297K.

Figure 3.12 shows the analogous time-resolved emission of the ESPT products of both photoacids. At short times, the rise-times of R^*O^- and Z^* signals are highly temperature dependent, where the rise time gets longer as the temperature decreases. At long times, the R^*O^-/Z^* signals decay exponentially where the lifetime increases with decreasing temperature. For MHQ at temperatures below the phase-transition, the decay of Z^* decreases by approximately a factor of 4. The signal also lacks the characteristic

rise time of photoprolytic processes ($R^*OH \rightarrow R^*O^- + H^+$), and the lifetimes match those of the C^* species. Because it appears that the ESPT is halted at $T < 173$ K, it is appropriate to assign the decays observed at 610 nm at temperatures below 173 K as the red-tail from the C^* fluorescence band, and not to a true Z^* emitting species.

The TCSPC decays of the C^* form of follow the order $PrOH > EtOH > BuOH$, where the decays are slowest in BuOH. The variable k_d is less dependent on the temperature at higher temperatures, while the rate decreases with a larger slope at lower temperatures. The dependence on the temperature is higher for shorter-chain alcohols, as observed by Cohen and Huppert.²⁷ All curves were fitted with the SSDP package using the MHQ ESPT kinetic model derived by Popov et. al.,⁴⁰ which is described further in this chapter. The fitting parameters are listed in Appendix B, Table B.1 and all fitted experimental kinetic curves are presented in Table B.2.

ESPT kinetics using Brownian Dynamics Simulations

The experiments and results described in this section were done in collaboration with Dr. Alexander Popov of Georgia Institute of Technology. All experimental results and BD simulations were obtained in the Tolbert laboratory. Dr. Popov's contributions included development of the BD simulations and the theoretical model and calculations used to describe the ESPT kinetics that were experimentally derived in the Tolbert laboratory (see Appendix C).

As stated above, the kinetic scheme describing ESPT from MHQ (Figure 3.13) is more complicated than for general photoacid systems (Figure 3.8).

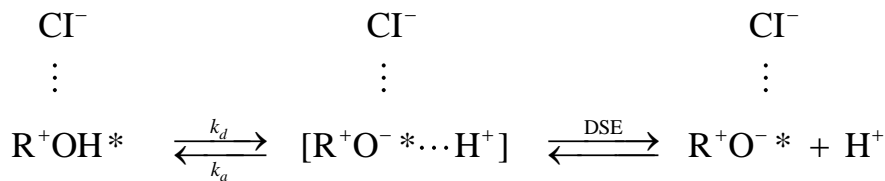


Figure 3.13 MHQ kinetic scheme.

The two main differences in the system stem from: (a) the potential force between the MHQ Z^* and the proton is anisotropic because of the large dipole moment of Z^* in the excited state, and (b) the counteranion (Cl^-) introduces a third body into the system, which strongly interacts with both the acid molecule and the proton. Because treating the system using SSDP assumes the proton is attracted to the Cl^-Z^* complex by pure Coulomb forces, attempts at fitting these data using the SSDP package were unsuccessful. It was therefore necessary to treat the Cl^-Z^* -proton interaction with weaker interactions.

The specific algorithm of the Brownian Dynamics simulation method that was used can be found in Appendix C. The results described in this section are based on the exact BD algorithm illustrated in Appendix C that were developed by Alex Popov of Georgia Institute of Technology. The curves presented in Figure 3.14 show the results of the BD simulations described in Appendix C. For all of the simulations, the lifetimes of the C^* and Z^* were taken to be , $\tau_0^1=20$ and 1.25 ns, respectively. These values are based on the estimates from the real MHQ-BuOH system. Other fitting parameters are listed in Table 3.2.

Table 3.2. Parameters used for calculating the curves in Fig. 3.14 and the acid dissociation constant for the C*, pK_a^* , Eq. 3.2. W_a is calculated by use of Eq. 3.3.

$R_{\text{reac}}, \text{\AA}$	2.9	3.5	4.5	5.5	6.0	7.0	8.0
κ_d, ns^{-1}	13	12	12	12	12	12	12
κ_a, ns^{-1}	0.6	1.45	8.5	15	21	40	50
$W_a, \text{M/ns}$	47.2	8.95	6.18	3.83	3.93	5.12	5.31
pK_a^*	0.56	-0.13	-0.29	-0.50	-0.48	-0.37	-0.35

The value of κ_a , found to be close to 12 ns^{-1} , can be defined directly from experiment where it is the initial descending slope of the bound-state (C*) population (C* curve, Figure 3.14). The rate κ_a increases with R_{reac} , or the reaction zone to where the proton can travel, where a shallow depth of the potential well at large reaction distances is compensated by a faster reaction. The results for the unbound-state (Z*) are nearly the same except for the largest value of R_{reac} . This indicates that the accuracy of the fitting is indicated by the fast decaying C*-state. The best fitting results correspond to the solid curves where $R_{\text{reac}} = 3.5\text{-}4.5 \text{ \AA}$. This means that the “contact” reaction mechanism, or the distance of closest proximity, $R_{\text{reac}} = R_{Z^*} + R_{H^+} = 2.9 \text{ \AA}$, is not suitable for this reaction and that the correct reaction distance should be between $3.5\text{-}4.5 \text{ \AA}$.

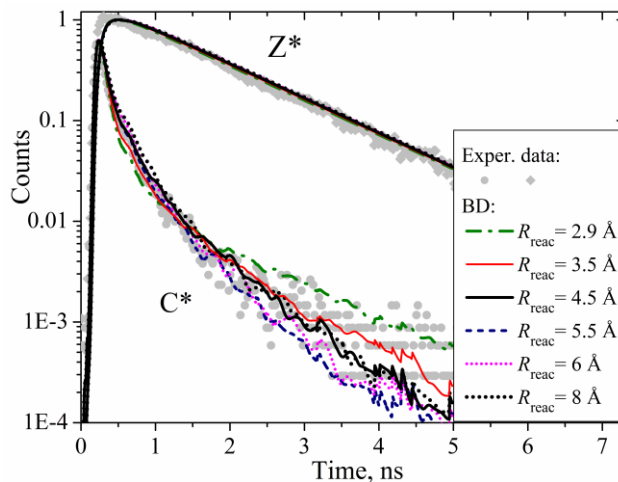


Figure 3.14. Experimental fluorescence decays (dots) of MHQ in BuOH and results of BD simulations (lines) at different R_{reac} .

From this information, the excited-state dissociation constant, $\text{p}K_{\text{a}}^*$ can be calculated for C^* by:

$$\text{p}K_{\text{a}}^* = -\log \frac{\kappa_d 10^{27}}{W_a N_A} \quad (\text{Eq. 3.2})$$

(for κ_d and W_a expressed through Å and ns), where W_a is taken from Eq. 3.3,

$$W_a = \int w_a(\mathbf{r}) \exp(-U(\mathbf{r})/k_B T) d\mathbf{r} \quad (\text{Eq. 3.3})$$

with $U(\mathbf{r})$ being the zwitterionic dipole potential. The averaging over the Boltzmann distribution within the reaction zone is performed numerically; the results presented in Table 3.2, and will be discussed below.

The results obtained at $R_{\text{reac}} = 3.5 \text{ Å}$ will be used to discuss some salient features of the reaction process (Figure 3.15).

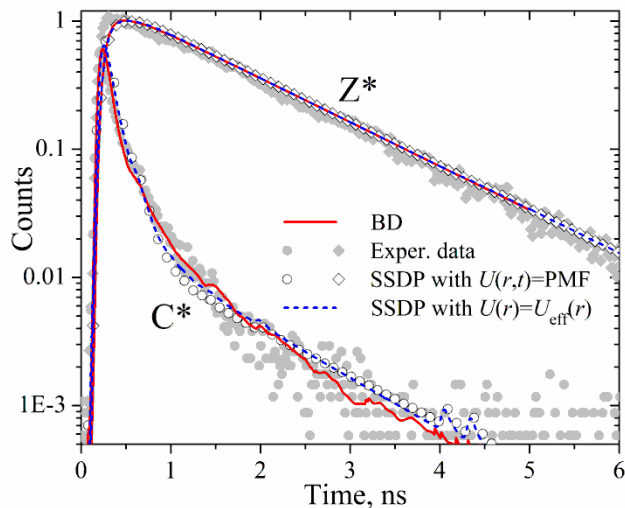


Figure 3.15. Experimental fluorescence decays of MHQ in BuOH (filled symbols) and results of BD simulations (solid lines), fittings using SSDP with time-dependent PMF taken from BD simulations (open symbols, See Appendix C.5) and fittings using SSDP with Kirkwood’s effective potential, Eq. 3.4 (dotted lines).

The mean-square displacements (MSDs) of all the particles and the mean-square distances between them are presented in Figure 3.16. Panel A shows that the proton diffuses similarly to Z^* , while Panel B indicates that it stays close to Z^* during the whole simulation. Therefore, the proton resides mostly near the reaction site due to the Coulomb attraction, so that the average $H^+ - Z^*$ distance does not exceed $\sqrt{300} < 20$ Å, meaning that any processes occurring outside the local area around Z^* can be ignored. This is a very important finding, which will be used later when determining the effective spherically symmetric potential.

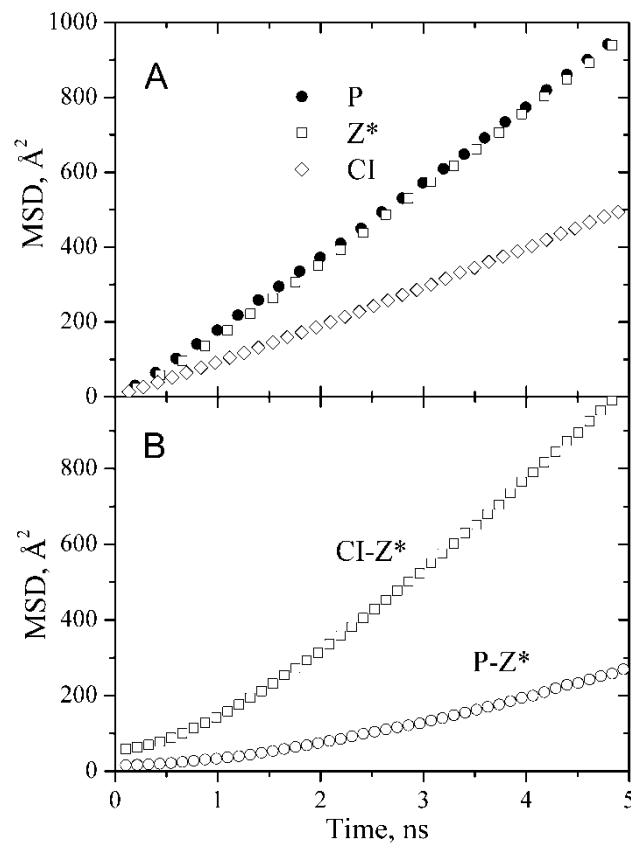


Figure 3.16. MSDs from BD simulations. (A) Mean-square displacements of the proton, zwitterion and counterion (B) Mean-square distances between the zwitterion-counterion (squares) and the zwitterion-proton (circles).

The CI moves approximately two times slower than the H^+ -Z* pair and is responsible for the quick nonlinear increase in the CI-Z* distance. The overall picture is rather complicated and despite straight lines in Panel A, one cannot assume that the particles move with constant diffusion coefficients.

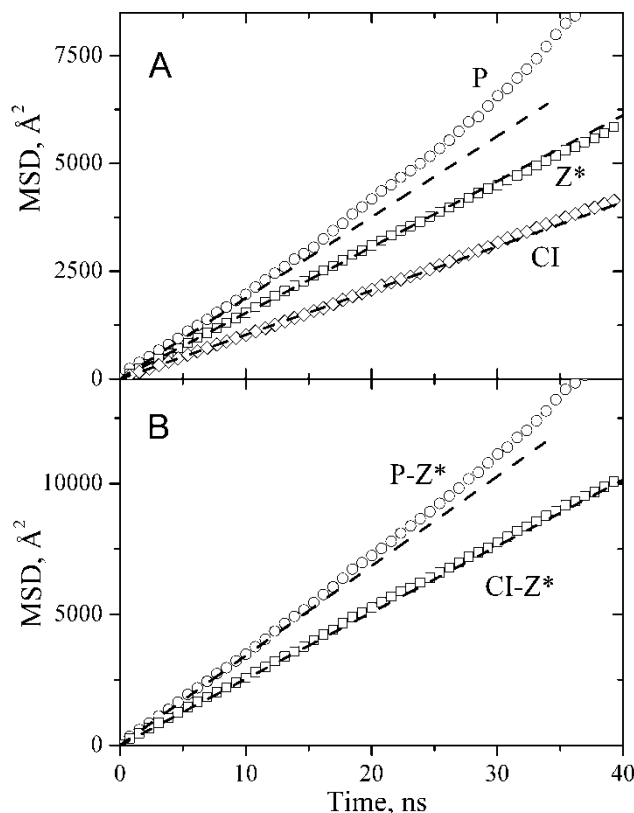


Figure 3.17. MSD from BD simulations without reaction and with interaction only between the proton and counterion. (A) MSD of proton, zwitterion and counterion. (B) MSD between zwitterion-counterion (squares) and zwitterion-proton (circles). Dashed lines are slopes at small times.

As stated above, SSDP requires a diffusion coefficient as an input value; however, it only takes into account mutual motion of two particles. This 3-body system is unique due to the presence of the counteranion and its possible effects on the diffusional motion of the proton. In order to test the Coulomb force on the proton diffusion coefficient, simulations were performed in which no ESPT or decay processes were present and therefore the charges were left only on the proton and the CI. Figure 3.17 shows the MSDs of the proton, Z* and CI (panel A), and the mean-square distances between the particles, assuming that they start with the initial configuration described in Appendix

C.6. For $t < 15$ ns, the functions are straight lines suggesting that within the time window of the MHQ protolytic photodissociation (~ 5 -10 ns), the motion of the particles is a diffusion process with effective diffusion coefficients. However, these diffusion coefficients may not be the self-diffusion ones explained in Appendix C.3, and are found from the slopes of the MSDs at small times. The slopes (dashed lines) are calculated by fitting the MSDs between $0 < t < 10$ ns, where the corresponding diffusion coefficients are listed in Table 3.3.

Table 3.3. Diffusion coefficients (in $\text{\AA}^2/\text{ns}$): “self” – used as input parameters in the BD simulations; “effective” – obtained by calculating the slopes of the MSDs in Fig. 5 at $0 < t < 10$ ns.

	D_P	D_{Z^*}	D_{CI}	D_{P-Z^*}	D_{CI-Z^*}
self	85	25	30	110 ($\equiv D_P + D_{Z^*}$)	55 ($\equiv D_{CI} + D_{Z^*}$)
effective	31.3	25.5	17.1	57.1	42.3

As expected, the resulting diffusion of Z^* does not change because no interaction is imposed on the particle. However, the diffusion coefficients of both the proton and CI decrease because the Coulomb attraction forces the particles to orbit around each other. The effective P- Z^* and CI- Z^* diffusion coefficients are: $D_{P-Z^*}^{\text{eff}} \approx D_P^{\text{eff}} + D_{Z^*}^{\text{eff}}$ and $D_{CI-Z^*}^{\text{eff}} \approx D_{CI}^{\text{eff}} + D_{Z^*}^{\text{eff}}$. This indicates that the relative motion of each pair is independent of the third particle. The mutual diffusion coefficient of the proton and Z^* , $D_{P-Z}^{\text{eff}} = 57.1 \text{ \AA}^2/\text{ns}$ can be used as an input parameter in SSDP.

An effective symmetric potential is also an input requirement for the SSDP program. The potential was derived by two different methods: (a) as an effective potential of mean force (PMF) between the proton and Z^* obtained by averaging the actual

potential with respect to the relative distribution of the CI, and (b) using Kirkwood's averaging to develop a method of calculation of the potential. The first method uses the full BD simulations and the latter method exploits the finding that the dynamic part of the problem can be reduced to just consideration of the proton motion in the vicinity of the reaction site, that is, we are only concerned about short distances from the reaction site. The derivations for these potentials can be found in Appendix C.8. Using a modified approach for calculating the radial distribution of a proton on an ensemble of diffusion Z^* -proton pairs (modified Kirkwood's averaging, see Appendix C.8), the effective potential was found to be:

$$\frac{U_{\text{eff}}(r)}{k_{\text{B}}T} \approx \frac{R_D p}{2r^2} (1 + \cos \theta_c) - \frac{R_D^2 p^2}{24r^4} (1 - \cos \theta_c)^2. \quad (\text{Eq. 3.4})$$

The U_{eff} from Eq 3.4 takes into account only the static dipolar part of the potential. The more complicated, non-stationary potential was also derived from the BD simulations (Appendix C.8). The simplified effective potential determined by Kirkwood's averaging is very close to that of the short-ranged PMF found from the full BD simulations (Figure 3.15). These findings allowed us to take into account the CI only by way of its influence on the motion of the proton, i.e., utilizing the mutual diffusion coefficient, $D_{\text{P-Z}^*}^{\text{eff}}$, but keeping only the simpler, static dipolar part of the potential (U_{eff}).

Discussion and Conclusions

ESPT kinetics in the picosecond to nanosecond regime

The ESPT kinetics of MHQ can be described using the geminate recombination (GR) scheme, where non-exponential decay behavior is observed in all systems. In protic solvents, the decays at 460 nm also show a tail with a similar lifetime (~20 ns) to the methyl ether derivative; that is, to the non-reacting analogue. This tail accounts for ~10% of the overall decaying species for the weaker-coordinating counteranions. Theory does not predict this long-lifetime tail and its explanation remains elusive. The emission profiles in protic versus aprotic solvents have provided some explanation for the counteranion effects. The long-lifetime tail mentioned above is only seen in protic solvents and disappears in solvents such as DMSO. Because aggregation has been ruled out, the presence of this tail indicates a kinetic effect. The long tail, presumably activated by the hydrogen-bond donation ability of the solvent, could be due to unreacted neutral MHQ. Its lifetime is very similar to the lifetime of the methyl ether derivative and to MHQ in acetonitrile, in which no reaction can occur. This observation further supports the hypothesis that this tail represents the neutral form that has either not undergone a reaction or has undergone a reverse reaction. Curiously, the lifetime of MHQ in water is longer than in DMSO. This may be explained by the decreased dipole moment of the MHQ excited state. For naphthols, the dipole moment increases upon excitation.²⁸ The roles of the solvent are not only to solvate the proton, but also are to solvate and stabilize the conjugate base through hydrogen-bond donation. Because the hydrogen-bond donation ability of water is so high, ESPT in naphthols is fastest in water.²⁶ For MHQ, however, the dipole moment decreases upon excitation. This indicates that hydrogen-

bond donation ability is not an important factor in ESPT dynamics. The faster lifetimes in DMSO can be explained in terms of proton solvating ability as opposed to hydrogen-bond donation ability, where DMSO is more basic and can therefore solvate the acidic proton more readily.

ESPT kinetics in the femtosecond to picoseconds regime

Similar to other “super” photoacids, the fluorescence decay of C* (for MHQ) and R*OH (for DCN2) was highly non-exponential. For this kinetic behavior Agmon et al. demonstrated²³ that the initial slope of such decay is governed mainly by the elementary proton dissociation event, while the subsequent curvature is caused by diffusion-assisted geminate recombination. Therefore, the femtosecond resolution of the fluorescence upon conversion gave more insight into kinetics of the proton photodissociation, the fastest

Table 3.4. Multiexponential decays (lifetimes and preexponential factors) of MHQ in various solvents. Debye relaxation times of these solvents.

Solvent	ϵ	$\tau_n(A_n)$, ps	τ_{avg} , ps	τ_D , ps ²⁹
MeOH	32.6	0.11(0.23), 3.1(0.39), 17.6(0.34), 88.9(0.04)	11	5.0
EtOH	24.3	0.14(0.25), 3.8(0.31), 16.3(0.23), 72.1(0.20)	20	16
PrOH	21.8	0.19(0.14), 1.4(0.11), 16.7(0.50), 107(0.25)	35	26
BuOH	17.8	0.21(0.03), 3.1(0.06), 19.7(0.34), 120(0.58)	76	63
Water	80.1	0.10(0.13), 0.65(0.42), 2.7(0.42), 79.0(0.03)	3.0	~1

intermolecular chemical process in these systems. The increasing lifetimes with increasing alcohol chain length for MHQ is expected. The decays are generally longer in longer-chain alcohols due to the decreased solvent polarity, which is manifested by a

lower dielectric constant. That is, increasing polarity accounts for a larger stability of the conjugate base and a more facile solvation of the proton.³⁰

The lifetimes in water and alcohols of MHQ* are comparable to and of the same order of magnitude as the dielectric relaxation times of the solvents as reported by Horgn and coworkers (Table 3.4).²⁹ The 3.0 ps lifetime in water is also similar to the value of 2.0 ps reported by Kim and Topp for MHQ in acidic solution.¹⁰ This suggests that the solvent relaxation dynamics control the proton transfer rate in the MHQ system. The wavelength dependence on the proton transfer kinetics essentially shows the solvent relaxation behavior. The solvation dynamics of polar photoproducts is associated with a red shift in the emission; therefore the faster relaxation at shorter wavelengths is due to MHQ-solvent interactions contributing to the dependence on wavelength that is observed in this system.³¹ Both solvation and proton transfer cause the blue edge to increase and the red edge to decrease.

The recombination in deuterated solvents is generally slower than in hydrogen-rich solvents because H(D) is involved in the rate-limiting step (i.e., the proton transfer). An H/D kinetic isotope effect (KIE) on the average lifetimes in similar hydroxyarene photoacid systems is generally around 3.³² The decays of water, MeOH, and EtOH show diminished isotope effects of 1.4, 1.6, and 1.9, respectively. The decreased isotope effect confirms the asymmetric and highly exergonic nature of the reaction and provides further evidence that the solvent controls the proton transfer rate. The KIE in these systems is close to the isotope effect for the proton mobility (1.4),³³ which suggests a small barrier for proton dissociation and almost no barrier for its recombination. Finally, the KIE has

been shown to increase the long-lifetime in geminate recombination systems,²² which confirms that MHQ systems fit the geminate recombination scheme.

Although there appears to be a lack of dependence on the counteranion on the ESPT as observed by TCSPC methods (Figure 3.8), the time resolution capable by the TCSPC setup is not fast enough to truly characterize the proton transfer step as the initial fast time could be heavily influenced by the instrument response function. Upon analysis of the fluorescence upconversion signals for the Nf^- and BF_4^- salts in EtOH, the lifetimes were determined to be almost identical (20 and 18 ps for Nf^- and BF_4^- , respectively). This confirms that in fact the nature of the counteranion is not influencing the proton transfer dynamics.

In short, the ultrafast kinetics of the MHQ systems in hydroxylic solvents appears to be solvent-controlled, as evidenced by the lifetimes and H/D isotope effect. This is in agreement with the claim by Kovalenko et al. that ESPT is governed by solvation in protic solvents.¹¹ The lifetime determined by us in water (3.0 ps) is close to that reported by Kim and Topp¹⁰ (2.0 ps), however we saw no indication of an intramolecular electron-transfer occurring in these systems. The ultrafast kinetics, and thus the proton-transfer rate, were determined to be solvent-controlled, where the lifetimes approached the dielectric solvent relaxation times, τ_D .

Temperature dependence on the ESPT rate

This part of the discussion will begin with a comparison of MHQ to the well-known “super” photoacid DCN2. Huppert and coworkers³⁴ first reported the temperature dependence on the ESPT rate for the “super” photoacid DCN2. They concluded that the

activation energy of the proton-transfer rate is temperature dependent; where the rate at low temperatures is solvent-controlled and therefore the ESPT time coefficient is comparable to the dielectric relaxation times of the solvent, while the rate at higher temperatures becomes controlled by a very low activation energy needed to cross the

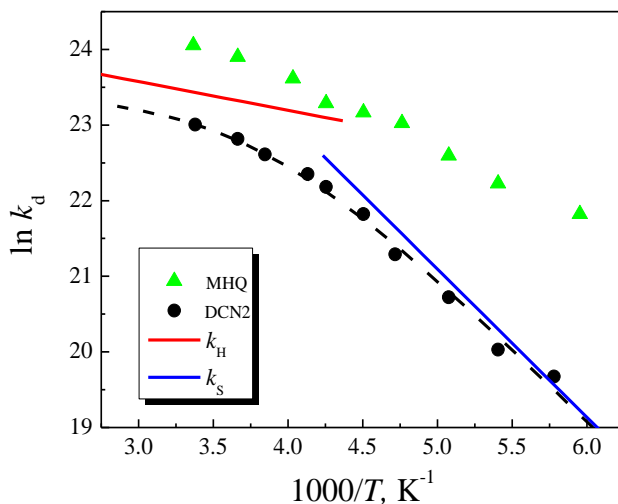


Figure 3.18. Arrhenius plot of protolytic photodissociation for MHQ (triangles) and DCN2 (circles) in EtOH. Symbols: calculations of the SSDP software. Fit for DCN2 obtained using Eqs. 3.5 and 3.6 is shown as a dashed line. Solvent coordinate (k_s , blue) and proton coordinate (k_H , red) are shown as straight lines. See Figure 3.19 for proton transfer coordinate fit for MHQ.

barrier for the proton transfer reaction.

The Arrhenius plot, $\ln(k_{PT})$ vs. $1/T$, of MHQ and DCN2 in EtOH is shown in Figure 3.18. The values of k_d are found by comparison of the experimental kinetics with the kinetics obtained by use of the SSDP technique. Huppert and coworkers found that k_d for DCN2 in EtOH and MeOH is almost independent of temperature in higher temperature ranges (293-333 K). At lower temperatures, the ESPT rate of DCN2

decreases rapidly with decreasing temperature. Such behavior is not observed for the MHQ system, where k_d decreases more or less linearly with decreasing temperature.

Similar plots for MHQ are shown in Figure 3.19 for k_d at different temperatures. The trend is similar to EtOH and is conserved for all alcohols, with the proton transfer rate decreasing relatively linearly with decreasing temperature. The slope at higher temperatures for shorter-chain alcohols appears to be slightly less than the slope at higher temperatures for longer-chain alcohols. This phenomenon was reported in previous work, where the independence of temperatures observed at higher temperatures becomes less pronounced as the alcohol chain length increases.³⁴

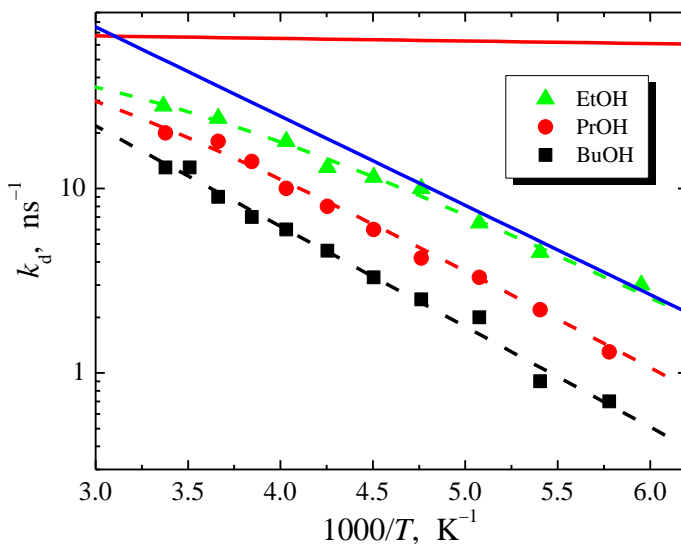
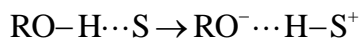


Figure 3.19. The protolytic photodissociation rates of MHQ at different temperatures in BuOH, PrOH and EtOH solutions. Symbols: calculations of the SSDP software (here and at the following figures the 298 K data point for MHQ/BuOH is taken from Ref. 40). Dashed curves: Fits resulted from Eqs. 3.5 and 3.6. Solvent coordinate (k_s , blue) and proton coordinate (k_H , red) for EtOH solution are also shown as straight lines.

Huppert and coworkers proposed a model to explain the unusual ESPT temperature dependence of “super” photoacids³⁴ where the proton transfer reaction depends on two coordinates: the solvent configuration and the proton translation motion along the reaction path. The solvent configuration can be thought of as the relative orientation of the hydrogen bonded solvent molecule with respect to the OH bond of the photoacid molecule where the energy is minimized when the oxygen-proton-oxygen connection is 180°. Previously, the solvent coordinate characteristic time was found to be within the range of the dielectric relaxation time τ_D and the longitudinal relaxation τ_L .³⁴ The actual proton translational motion along the reaction path, or



restricts the proton transfer process to be stepwise. This coordinate is dependent on the first solvation shell because the proton will only move adjacent to the hydrogen bonded solvent molecule when the solvent configuration brings the system to an energy minimum, or the lowest energy barrier of the proton coordinate. The model includes only the energy-minimized solvent configuration and thus excludes alternative routes for ESPT, for which other solvent configurations may cause the reaction to have many reaction rates. Thus the kinetics of the reaction can be described as the sum of two characteristic times, $\tau = \tau_1 + \tau_2$, accounting for the solvent reorganization time (τ_1) and the time for the proton to pass over the energy barrier (τ_2). The overall rate constant $k_d(T)$ at a given T becomes

$$k_d(T) = \frac{k_H(T)k_s(T)}{k_H(T) + k_s(T)} \quad (\text{Eq. 3.5})$$

for which k_s is the solvent coordinate rate constant, and k_H is the proton coordinate rate constant. Similar expressions for an overall rate constant are used for several important phenomena, such as the overall rate constant for electron-transfer³⁵ and a diffusion assisted chemical reaction.³⁶

The temperature dependence of k_d was fitted using Eq. 3.5 given that both solvent and proton rate constants, k_s and k_H , obey the Arrhenius law,

$$k_{s(H)} = A_{s(H)} \exp(-E_{s(H)}/k_B T) \quad (\text{Eq. 3.6})$$

The preexponential factors, $A_{s(H)}$, and the activation energies, $E_{s(H)}$, are presented in Table 3.5. The high energies are associated with the solvent modes and are calculated with 5% percent accuracy, whereas the small energies are not well defined and fall within a 50% accuracy range.

Table 3.5. Parameters of the proton and solvent coordinate rates, k_H and k_s Eq. 3.6 used for calculating the dissociation rate, k_d , Eq. 3.5.

	A_s, ns^{-1}	$E_s, \text{kJ/mol}$	A_H, ns^{-1}	$E_H, \text{kJ/mol}$
MHQ in BuOH	940	10.4	--	--
MHQ in PrOH	1,800	10.3	99	0.22
MHQ in EtOH	2,100	9.3	74	0.27
DCN2 in EtOH	20,900	16.0	16.3	0.32

The activation energy of k_d for DCN2 in EtOH as a function of $1/T$ is shown in Figure 3.20 as obtained by differentiating a fit to the data shown in Figure 3.18

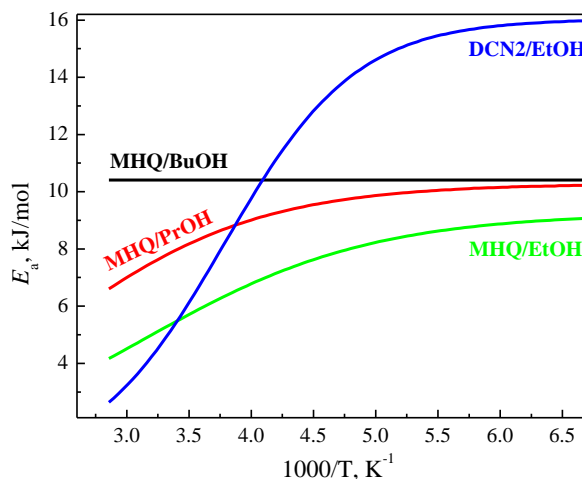


Figure 3.20. Protolytic photodissociation activation energies for MHQ and DCN2 in various alcohols as derived from Eqs. 3.5 and 3.6.

(Arrhenius plot), $E_a = k_B T^2 d \ln k_d(T) / dT$. The activation energy for the photoacid increases monotonically as the temperature decreases and approaches a value similar to the solvent dielectric relaxation time. The literature value of the activation energy of τ_D in EtOH is 16 kJ/mol.³⁷ The ESPT activation energy at low temperatures was determined to be 16.0 kJ/mol for DCN2 (see Table 3.5).

Analogously, the activation energies for MHQ in EtOH, PrOH and BuOH as a function of $1/T$ are shown in Figure 3.20 as obtained in the same fashion as described above. Two observations can be made. First, these energies directly correlate with the mass (or the chain length) of the solvent molecules. Second, at higher temperatures they

decrease, facilitating the motion (except BuOH for which this behavior should be expected). Note that for BuOH, a possible curvature of the line is obscured by the experimental errors, leaving E_H indeterminate. Therefore, only one component, solvent, can be obtained. The literature values of the activation energy of τ_D in PrOH and BuOH are 21 and 31 kJ/mol and the ESPT activation energies of MHQ in EtOH, PrOH and BuOH were determined to be 9.3, 10.3, and 10.4 kJ/mol, respectively. These values somewhat differ because not only the rotational (dielectric), but also the translational coordinate can assist the ESPT, thus facilitating dissociation.

The recombination rate, k_r , cannot be treated separately from the contact radius, since in all the equations they appear together via the association rate constant,

$$k_a = 4\pi a^2 k_r \quad (\text{Eq. 3.7})$$

The temperature behavior of this constant is shown in Figure 3.21. Analogously to Eqs. 3.5 and 3.6, we suggest that the association is caused by two sequential processes. Corresponding values of A_1 , E_1 and A_2 , E_2 for these processes are presented in Table 3.6. Process “1” is the slowest one and should be associated with the solvent coordinate. Note that in this case it is possible to identify two-rate behavior only for BuOH solution: the other curves appear linear on the Arrhenius plot.

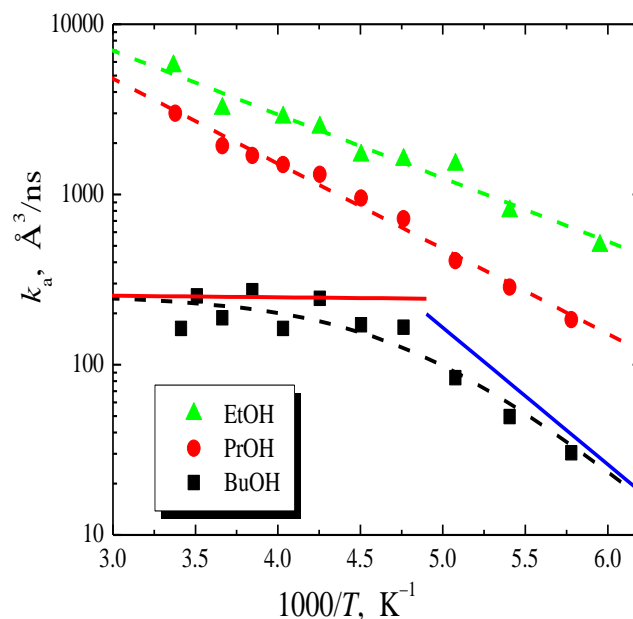


Figure 3.21. The association rates of MHQ protolytic photodissociation in BuOH, PrOH and EtOH solutions at different temperatures. Symbols: calculations of the SSDP software. Dashed curves: Fits resulted from Eqs. 3.5 and 3.6. Solvent coordinate (k_s , blue) and proton coordinate (k_H , red) for EtOH are also shown as straight lines.

Table 3.6. Parameters of the proton and solvent coordinates rates used for calculating the association rate, k_r .

	A_1, ns^{-1}	$E_1, \text{kJ/mol}$	A_2, ns^{-1}	$E_2, \text{kJ/mol}$
MHQ in BuOH	$1.7 \cdot 10^6$	15.4	270	0.17
MHQ in PrOH	$1.5 \cdot 10^5$	9.6	--	--
MHQ in EtOH	$9.2 \cdot 10^4$	7.2	--	--

Butanol is special in this case: *dissociation* is a one-step process, whereas for propanol and ethanol *association* is a one-step process. We believe, however, that two steps are necessary for the reaction to occur. In terms of the theory of diffusion-controlled reactions, this requires that the solvent coordinate is the slowest for dissociation in butanol and for association in the two other liquids.

The pK_a^* can be obtained directly from Eqs. 3.4 and 3.5. Using our choice of units (\AA and ns), 3.4 can be written in the form

$$pK_a^* = \log \frac{k_a N_A 10^{-27}}{k_d \exp(U_{\text{eff}}(a)/k_B T)}. \quad (\text{Eq. 3.8})$$

The values of pK_a^* are shown in Figure 3.22. Table 3.7 presents enthalpy, ΔH , and entropy, ΔS , of the proton transfer reaction.

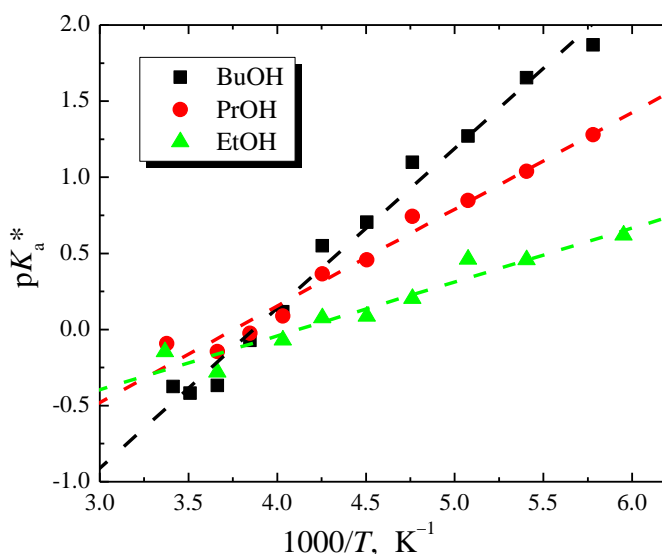


Figure 3.22. MHQ pK_a^* values at different temperatures in BuOH, PrOH and EtOH solutions. Symbols: calculations according to Eq. 3.8. Dashed curves: linear fits which were used to calculate enthalpy, ΔH , and entropy, ΔS in Table 3.7.

Table 3.7. Values of the enthalpy, ΔH , and entropy, ΔS , of the proton transfer reaction obtained as slopes and intercepts of the pK_a^* curves in Fig. 3.22.

	ΔH , kJ/mol	ΔS , J/mol/K
MHQ in BuOH	20.1	78
MHQ in PrOH	12.2	46
MHQ in EtOH	6.8	28

As described in previously in this chapter, the counterion, while in the vicinity of the proton, decreases the diffusion of the proton in n-butanol by 50% in the first 20-30 ns of the ESPT reaction time. Since the experimental data covered only 5-6 ns, the diffusion coefficient was assumed to be constant, constituting half of its value in the bulk. However, quantitatively this picture can be incorrect. Indeed, since the actual behavior of the counteranion was not known, it was modeled as a spherical particle with some estimated properties. In the current paper we also attempted to employ a changing diffusion coefficient, but we fitted major parameters to get a better coincidence with the experiment. To do this, we implemented the formula

$$D(t) = D_0 + (D_1 - D_0)\exp(-t/\tau) \quad (\text{Eq. 3.9})$$

where D_0 and D_1 are the initial and final diffusion coefficients and τ is the characteristic time during which the counterion affects the proton motion (in Ref. 40 $\tau \approx 20\text{-}30$ ns).

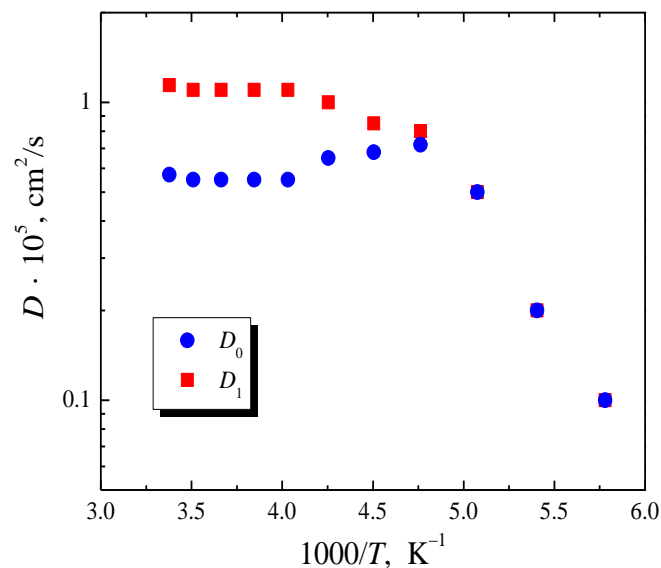


Figure 3.23. Mutual diffusion coefficients of a proton-zwitterion pair at different temperatures in BuOH. Both D_0 (circles) and D_1 (squares) are shown.

Starting with BuOH, we found that the idea of splitting the diffusion coefficient was very helpful for high temperatures. For low temperatures and for the two other solvents, one coefficient adequately fit the data. Figure 3.23 depicts both D_0 and D_1 for BuOH solution. The characteristic times τ are taken in the range from 2 to 3 ns. To check the consistency between current calculations and those from Ref. 40, the mean square displacement (MSD) calculated from Eq. 3.9 was compared with the analogous MSD from Ref. 40. The result is displayed in Figure 3.24. Although the estimated Brownian dynamics underestimated the diffusion rate, the difference between two MSDs at $t < 6$ ns was not large.

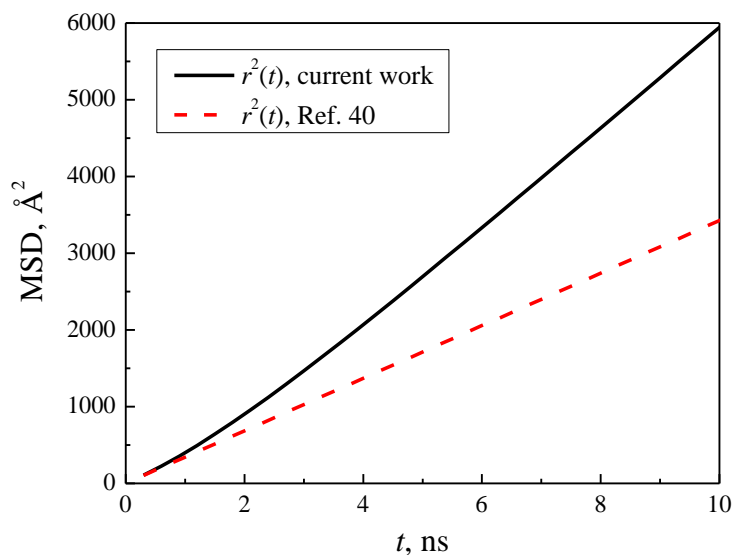


Figure 3.24. The mean square displacement of a proton-zwitterion pair at $T=293$ K in BuOH. Solid line: according to 3.9. Dashed line: MSD from Ref. 40.

The temperature dependence of the mutual diffusion coefficient for the pair “proton-Z*” is depicted in Figure 3.25. While at lower temperatures, D increased linearly with temperature, at higher temperatures the diffusion coefficient remained almost constant. Fitting gave the highest activation energy (Table 3.8): it was not possible to extract the low energy from the data, so we set $E_1^D = 0$ and used the following form of Eq. 3.5:

$$D(T) = \frac{D_\infty}{c_1 + c_2 \exp(E_2^D / k_B T)}, \quad c_2 = 1 - c_1 \quad (\text{Eq. 3.10})$$

where D_∞ is the asymptotic value of the diffusion coefficient at $T \rightarrow \infty$, E_2^D is the remaining activation energy and $c_{1,2}$ are the weights with which two hypothetical processes contribute to the overall effect. Interestingly, while the potential barrier practically disappeared for one of the processes, its weight, c_1 , was very close to unity.

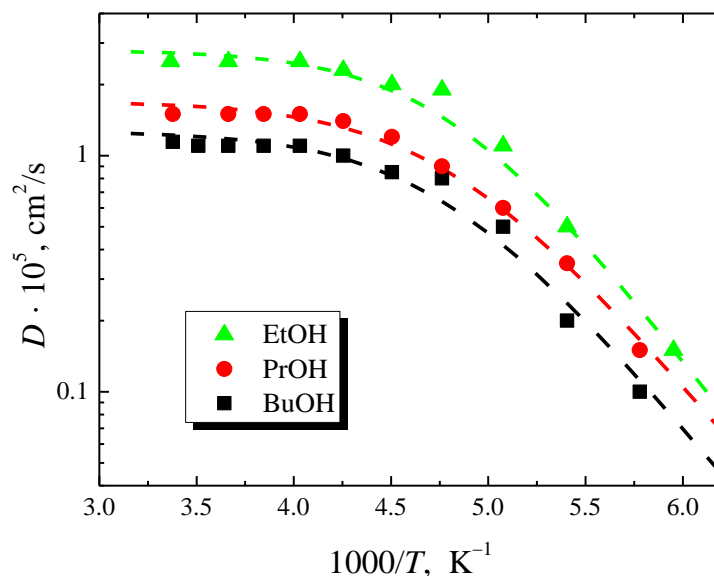


Figure 3.25. Mutual diffusion coefficients of a proton-zwitterion pair at different temperatures for BuOH, PrOH and EtOH solutions (for BuOH D_1 is shown). Dashed curves: fits performed in accordance with the help of Eqs. 3.5 and 3.6.

Most probably, this barrierless process belongs to translational motion, which lowers the ESPT activation energies as compared with the activation energies of dielectric relaxation – i.e., rotation. The solvent characteristic times, thus, become less than the dielectric relaxation ones: $\tau_s < \tau_D$.

Table 3.8. Values of the parameters in Eq. 3.9 used for fitting the diffusion coefficients.

	D_{∞} , cm ² /s	E_2^D , kJ/mol	c_2 ($c_1 = 1 - c_2$)
MHQ in BuOH	1.3e-5	19.2	1.7e-5
MHQ in PrOH	1.7e-5	18.8	2.0e-5
MHQ in EtOH	2.8e-5	20.7	6.7e-6

The temperature dependence of k_d for MHQ did not follow the previously described model for DCN2 precisely, suggesting that the model fails for MHQ in long-chain alcohols. The ESPT rate of DCN2 at low temperatures is governed by the solvent relaxation, because solvent reorientation is slower than the proton transfer while at higher temperatures the rate becomes controlled by the intrinsic barrier (activation energy) of the photoprolytic dissociation process. MHQ does not exhibit the same plateau in ESPT rate at higher temperatures and the rate is relatively constant. The rate in longer-chain alcohols becomes less independent of temperature at higher temperatures in both DCN2 and MHQ. The activation energies for MHQ in alcohols are less than those for DCN2 and less than the activation energies for τ_D . This is not unexpected because generally the faster the process, the lower the activation energy. Since the ESPT process is faster in MHQ than in DCN2, the activation energy for the process is less and thus does not correlate to the activation energy for the dielectric relaxation time. With respect to the thermodynamic parameters, ΔH and ΔS , the lower the enthalpy, the less enthalpic/entropic barrier for the recombination process.³⁸ Thus, we expect the lowest barrier for recombination in ethanol (see Table 3.7). The three unit pK_a^* difference between these photoacids drove the notable difference in the change in kinetic behavior. Due to the differences in their excited-state acidities, the relative contributions of the

solvent-coordinate and the proton-transfer coordinate change for DCN2 versus MHQ.

The temperature dependence for MHQ is slightly less than for DCN2 and we are unable to observe biexponential behavior consistent with the qualitative model previously described by Huppert and coworkers.

Describe ESPT kinetics using Brownian Dynamics Simulations

When the kinetics of photoacid systems cannot be solved analytically, the SSDP package is typically utilized. However, due to the highly asymmetric nature of the MHQ system, the time evolution of the bound (C^*) versus unbound (Z^*) pair cannot be solved using SSDP. The anisotropic, dynamic, three-body problem does not allow one to treat the cation, zwitterion, and proton as symmetric point-charges, as needed to effectively use SSDP. Using Brownian Dynamics simulations to describe the MHQ system resulted in the set of ESPT rate constants and gave unique information about the time-dependent mutual diffusion coefficients and interaction potentials in the three-body system. The role of the CI on the protolytic photodissociation was determined to be an effective slowing down of the proton. The extent to which the proton is slowed down can be revealed by effectively eliminating the coordinates of the CI molecule. The simulations showed that the proton diffusion coefficient becomes three times less, where the mutual H^+-Z^* coefficient decreases by a factor of two. The highly asymmetric force field between the proton and Z^* was adapted to a spherically-symmetric potential using the idea of relative equilibrium in the vicinity of the reaction zone. Therefore the original, highly complex problem was reduced to a class of a spherically symmetric parameters. One can now apply the very efficient SSDP problem to obtain desired kinetic and thermodynamic data in a matter of minutes in contrast to the BD simulations which take days or weeks to

obtain enough statistics to accurately model the MHQ system. The pK_a^* value for MHQ in BuOH was determined to be in the range of -0.3 to -0.5. It is known that for DCN2, the difference of pK_a^* in water and butanol is³⁹

$$pK_a^*(H_2O) - pK_a^*(BuOH) = -6.6.$$

It can therefore be determined that for MHQ, the $pK_a^* \approx -7$ in water, an unprecedented pK_a jump in the excited state!

References

1. (a) Tolbert, L.M.; Haubrich, J.E. *J. Am. Chem. Soc.* **1994**, 116, 10593 (b) Salvitti, M. (2008) *N-Methyl-6-hydroxyquinolinium: An investigation into the spectroscopy and applications of excited-state proton transfer*. (Master's Thesis) Retrieved from SMARTech.
2. Forster, T. *Naturwiss.* **1949**, 36, 186.
3. Tolbert, L.M.; Solntsev, K.M. *Acc. Chem. Res.* **2002**, 35, 19.
4. Solntsev, K.M.; Clower, C.E.; Tolbert, L.M.; Huppert, D. *J. Am. Chem. Soc.*, **2005**, 127, 8534
5. Bardez, E.; Chatelain, A.; Larrey, B.; Valeur, B. *J. Phys. Chem.* **1994**, 98, 2357
6. Hansch, C.; Leo, A.; Taft, R.W. *Chem. Rev.* **1991**, 91, 165
7. (a) Maglothin, J.A.; Chen W.-S.; Wilson, I.B. *Mol. Pharmacol.*, **1976**, 12, 658. (b) Lasslo, A.; Quintana, R.P.; Dugdale, M.; Johnson, R.W.; Naylor, J.L. *ASAIJ*, **1983**, 6, 47. (c) Barthelmes, H.U.; Niederberger, E.; Roth, T.; Schulte, K.; Tang, W.-

- C., Boege, F.; Fieberg, H. –H.; Eisenbrand, G.; Marko, D. *Brit. J. Cancer*, **2001**, 85, 1585.
8. Schulman, S.; Fernando, Q. *Tetrahedron* **1968**, 24, 1777
 9. Drummond, C.J.; Grieser, F.; Healy, T.W. *J. Phys. Chem.*, **1988**, 92, 2604.
 10. Kim, T.G.; Topp, M.R. *J. Phys. Chem. A* **2004**, 108, 10060
 11. Perez-Lustres, J.L.; Kovalenko, S.A.; Mosquera, M; Senyushkina, T.; Flasche, W.; Ernsting, N.P. *Angew. Chem. Int. Ed.* **2005**, 44, 5635
 12. Perez-Lustres, J.L.; Rodriguez-Prieto, F.; Mosquera, M; Senyush, T.; Ernsting, N.P.; Kovalenko, S.A. *J. Am. Chem. Soc.*, **2007**, 129, 5408.
 13. Park, S.Y.; Lee Y.S.; Jang, D.J. *Phys. Chem. Chem. Phys.*, **2008**, 10, 6703.
 14. Malval, J.P. ; Diemer, V. ; Morlet-Savary, F. ; Jacques, P. ; Chaumeil, H. ; Defoin, A. ; Carre C. ;. Poizat, O. *J. Phys. Chem. A*, **2010**, 114, 2401.
 15. Ihmels, H. K. Schäfer, K. *Photochem. Photobiol. Sci.*, **2009**, 8, 309.
 16. (a) Paulo, L.; Freitas, A.A; da Silva, P.F.; Shimizu, K.; Quina, F.H.; Maçanita, A.L. *J. Phys. Chem. A*, **2006**, 110, 2089; (b) Quina, F.H.; Moreira, P.F.; Vautier-Giongo, C.; Rettori, D.; Rodrigues, R.F.; Freitas, A.A.; da Silva, P.F.; Maçanita, A.L. *Pure Appl. Chem.*, **2009**, 81, 1687.
 17. Karton-Lifshin, N.; Presiado, I.; Erez, Y.; Gepshtein, R.; Shabat, D.; Huppert, D. *J. Phys. Chem. A*, ASAP DOI: 10.1021/jp2095856.
 18. Van den Berg, O.; Jager, W.F.; Picken, S.J. *J. Org. Chem* **2006**, 71, 2666
 19. Van den Berg, O.; Jager, W.F.; Cangialosi, D.; vanTurnhout, J.; Verheijen, P.J.T.; Wubbenhorst, M.; Picken, S.J. *Macromolecules*, **2006**, 39, 224
 20. Eigen, M.; Kruze, W.; Maas, G.; De Maeyer, L. *Prog. React. Kinet.* **1964**, 2, 285-318

21. Martynov, I.Y.; Demyashkevich, A.B.; Uzhinov, B.M.; Kuzmin, M.G. *Russ. Chem. Rev.* **1977**, 46, 3.
22. (a) Pines, E.; Huppert, D. *J. Chem. Phys.* **1986**, 84, 3576 (b) Pines, E.; Huppert, D. *Chem. Phys. Lett.* **1986**, 126, 87.
23. (a) Pines, E.; Huppert, D.; Agmon, N. *J. Chem. Phys.* **1988**, 9, 5620. (b) Agmon, N. *J. Phys. Chem. A* **2005**, 109, 13.
24. (a) von Smoluchowski, M. *Z. Phys. Chem.* **1917**, 92, 129. (b) Debye, P. *J. Electrochem. Soc.* **1942**, 82, 265
25. Krissinel', E.B.; Agmon, N. *J. Comp. Chem.* **1996**, 17, 108.
26. Solntsev, K.M.; Huppert, D.; Agmon, N. *J. Phys. Chem A* **1999**, 103, 6984.
27. (a) Carmeli, I.; Huppert, D.; Tolbert, L.M.; Haubrich, L.E. *Chem. Phys. Lett.*, **1996**, 260, 109. (b) Cohen, B.; Huppert, D. *J. Phys. Chem. A*, **2000**, 104, 2663. (c) Cohen, B.; Huppert, D. *J. Phys. Chem. A*, **2001**, 105, 2980. (d) Cohen, B.; Huppert, D. *J. Phys. Chem. A*, **2002**, 106, 11115. (e) Cohen, B.; Huppert, D. *J. Phys. Chem. A*, 2003, 107, **1433**.
28. Agmon, N.; Rettig, W.; Groth, C. *J. Am. Chem. Soc.*, **2002**, 6 1089.
29. Horgn, M.L.; Gardecki, J.A.; Papazyan, A.; Maroncelli, M. *J. Phys. Chem.*, **1995**, 99, 17311. (a) Jimenez, R.; Fleming, G. R.; Kumar, P. V.; Maroncelli, M. *Nature (London)* **1994**, 369, 473. (b) Jarzeba, W.; Walker, G. C.; Johnson, A. E.; Kahlow, M. A.; Barbara, P. F. *J. Phys. Chem.* **1988**, 92, 7039. (c) Rips, I.; Klafter, J.; Jortner, J. *J. Chem. Phys.* **1988**, 88, 3246. (d) Rips, I.; Klafter, J.; Jortner, J. *J. Chem. Phys.* **1988**, 89, 4299.

30. (a) Solntsev, K.M.; D. Huppert, D.; Agmon, N. *J. Phys. Chem. A.*, **1998**, 102, 9599
 (b) Solntsev, K.M.; Huppert, D.; Agmon, N. *J. Phys. Chem. A.*, **1999**, 103, 6984.
31. Radoszkowicz, L.; Presiado, I.; Erez, Y.; Nachliel, E.; Huppert, D.; Gutman, M.
PCCP **2011**, 13, 12058-12066
32. E. Pines in *Isotope Effects in Chemistry and Biology*. Eds. A. Kohen and H.-H. Limbach. CRC Press, Boca Raton. **2005**. pp. 451-464.
33. Solntsev, K.M.; Huppert, D.; Agmon, N.; Tolbert, L.M. *J. Phys. Chem. A.* **2000**, 104, 4658-4669
34. (b) B. Cohen and D. Huppert, *J. Phys. Chem. A*, **2000**, 104, 2663. (c) B. Cohen and D. Huppert, *J. Phys. Chem. A*, **2001**, 105, 2980. (d) B. Cohen and D. Huppert, *J. Phys. Chem. A*, **2002**, 106, 11115. (e) B. Cohen and D. Huppert, *J. Phys. Chem. A*, **2003**, 107, 1433.
35. Rips, I.; Jortner, J. *J. Chem. Phys.* **1987**, 87, 2090
36. (a) Szabo, A. *J. Phys. Chem.* **1989**, 93, 6929. (b) Collins, F.C. and Kimball, G.E. *J. Colloid Sci.*, **1949**, 4, 425.
37. (a) C. F. J. Böttcher and P. Bordewijk in *Theory of Electric Polarization*; Elsevier: Amsterdam, **1978**; vol. 2, p 254. (b) M.W. Sagal, *J. Chem. Phys.*, **1962**, 36, 2437.
38. G.W. Robinson, *J. Phys. Chem.*, **1991**, 95, 1038.
39. K. M. Solntsev, L. M. Tolbert, B. Cohen, D. Huppert, Y. Hayashi and Y. Feldman, *J. Am. Chem. Soc.*, **2002**, 124, 9046.
40. Popov, A.V.; Gould, E.-A.; Salvitti, M.A.; Hernandez, R.; Solntsev, K.M. *Phys. Chem. Chem. Phys.* **2011**, 13, 14914.

CHAPTER 4

MHQ AS A PHOTOCHEMICAL AGENT IN VARIOUS MICROHETEROGENEOUS SYSTEMS

Part I. Studies of the Photoinduced Cationic Polymerization of Cyclohexene Oxide using MHQ*

*This section is heavily drawn from Gould, E.-A.; Salvitti, M.A., Kowalik, J., Solntsev, K.M., Tolbert, L.M. Cationic polymerization via direct excited-state proton transfer: A cautionary tale. *Macromol.* Submitted.

Introduction

Initiating polymerization via transient acid production is an intriguing idea, but elusive in practice. The literature is replete with photoinduced cationic polymerizations; however, these reactions involve photoacid generator (PAGs) use.¹ The general mechanism of polymerization with PAGs involves PAG photodegradation resulting in irreversible acid production. Irreversible acid generation is the major drawback to the current PAG applications² and has prompted work to find a transient photoacid catalyst. Reports of photopolymerization without photodegradation used a sulfonium salt “proton cascade” where the excited proton is transferred to a tetrafluoroborate counteranion, leaving a relatively stable quinoid-type structure.³ These authors reported that thermal recombination was slow enough to allow for the solvated fluoroboric acid to catalyze polymerization. Hino and Endo⁴ reported the only example of photopolymerization via

photoinduced direct proton transfer to the monomer to catalyze the reaction. They claimed that various fluorophenols were capable of photopolymerizing the simple monomer, glycidyl phenyl ether, via an excited-state hydrogen bonded intermediate.

The possibility of using the strongest reversible photoacid to initiate direct ESPT-induced cationic photopolymerization is intriguing, so the polymerization of the simple epoxide monomer cyclohexene oxide (CHO, Figure 4.1) using MHQ was explored. Reactions were attempted with CHO because it is fairly sensitive to acid generation at room temperature and is an industrial and academic standard for testing cationic photoinitiators;⁵ additionally, the literature contains many examples for comparison.

Experimental Protocols

Quinoline (98%), 6-hydroxyquinoline (98%) and 6-methoxyquinoline (98%) were purchased from Acros and used without further purification. Methyl nonafluorobutanesulfonate (nonaflate) was purchased from Synquest Laboratories and used without further purification. Cyclohexene oxide (CHO) (98%) was purchased from Sigma-Aldrich and used without further purification. *N*-Methyl-6-hydroxyquinolinium (MHQ) and *N*-methyl-6-methoxyquinolinium (MMQ) salts were synthesized according to the method described in Chapter 3. *N*-Methylquinolinium nonaflate (MQ) was synthesized with the procedure described for MHQ and MMQ using quinoline as the starting material.

A 5% wt. sample of the photoacid (1 mg) and CHO (20 μ L) was added to an NMR tube in 0.75 mL d_6 acetone (99%, Cambridge Isotope Laboratories). The sample was irradiated in the Hanovia photoreactor equipped with a 450 W medium-pressure

mercury lamp at room temperature. A combination of MHQ absorption spectrum in acetone, the transmission spectrum of the NMR tube, and the emission spectrum of the Hg lamp, leads to the conclusion that the photochemical processes are induced by the strong 365 nm mercury spectral line. The NMR spectra were recorded at various intervals in order to determine the kinetics of polymerization. Rates of polymerization were determined by calculating the integration of peaks between 1.0-1.5 ppm to the disappearance of the peak representing the proton alpha to the epoxide at 3.05 ppm. Pentafluorophenol (PFP), bis(trifluoromethyl)phenol (BTFMP), and 2,3-difluorophenol (DFP) were purchased from Sigma-Aldrich and used without further purification.

Aliquots (0.5 mL) of the reaction mixtures were mixed with DI water in a 1:1 ratio. The pH of the mixture was then determined using a VWR SympHony detector with an Ag/AgCl electrode.

A VWR Symphony Fluoride I ISE was used to determine the presence of fluoride ions in the reaction mixtures. Aliquots (0.5 mL) were mixed in a 1:1 ratio with a low-level Total Ionic Strength Buffer as prepared per the manual accompanying the ISE. The voltage was measured and converted to concentration using a calibration curve for the instrument.

Molecular weights of the photoproducts were measured using gel permeation chromatography (GPC). Polystyrene standards were used to create a calibration curve used for analyzing retention times of polymers. The GPC was composed of a Waters 2410 Separations Module and was equipped with Waters Styragel HR 4, 3, and 1 THF columns with detection performed by a Waters 410 refractive index detector.

Results

Various photoacid (5% w/w MHQ to CHO) and monomer samples were irradiated and the reaction progress was monitored via ^1H NMR spectroscopy (Figure 4.1) The peak at

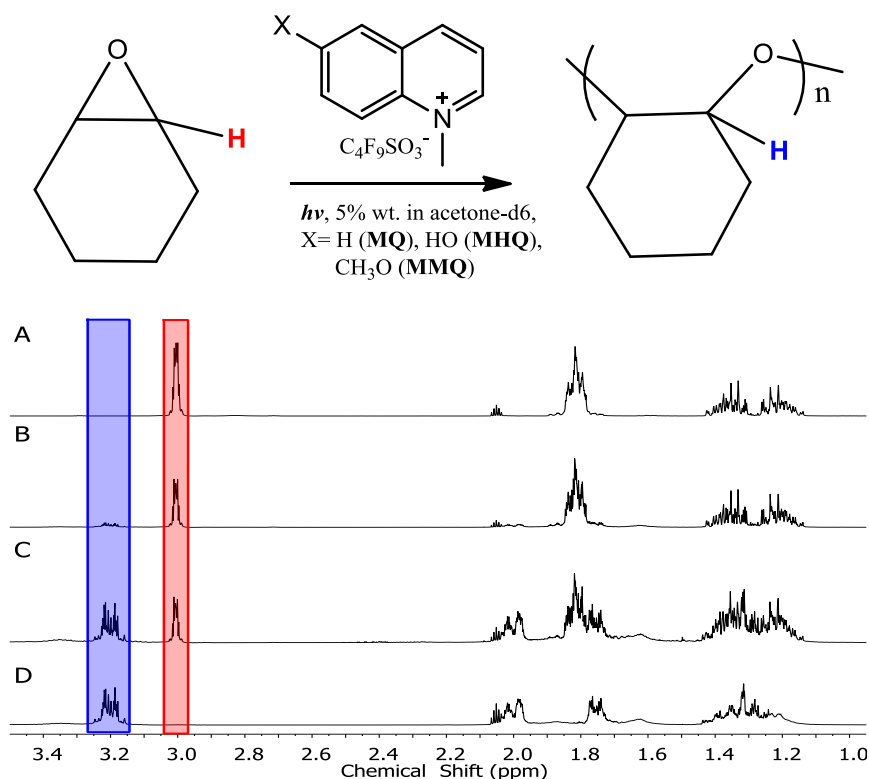


Figure 4.1. Top: Reaction scheme of polymerization of CHO by MQs. Bottom: NMR spectra of reaction mixture taken after $t=0$ (A), 1 (B), 2 (C), 5 (D) hours photolysis.

3.0 ppm was assigned to the proton alpha to the epoxide and therefore the constant integration of the NMR peak at 3.0 ppm compared to the peak shifted slightly downfield at 3.2 ppm was used to determine the rate of polymerization. Spectra were taken every hour until the monomer was completely consumed. As monitored by NMR, CHO polymerization in the presence of MHQ occurred readily, with complete conversion after just three hours. The reaction did not proceed in the dark, nor did CHO polymerize in

acetone by irradiation in the absence of the quinolinium salts. The molecular weights of the polymers were determined via GPC analysis to be 847 g/mol, i.e., oligomers with a degree of polymerization (DOP) of 4-5.

Polymerizations were carried out using a variety of MHQ salts with different counteranions. Only the fluorine containing salts catalyzed the polymerization (Figure 4.2). The rate of the polymerization was dependent on the counteranion, where the presence of more strongly coordinating counteranion induced faster reaction times. This also corresponded to the relative counteranion conjugate acid strengths. The fluorinated

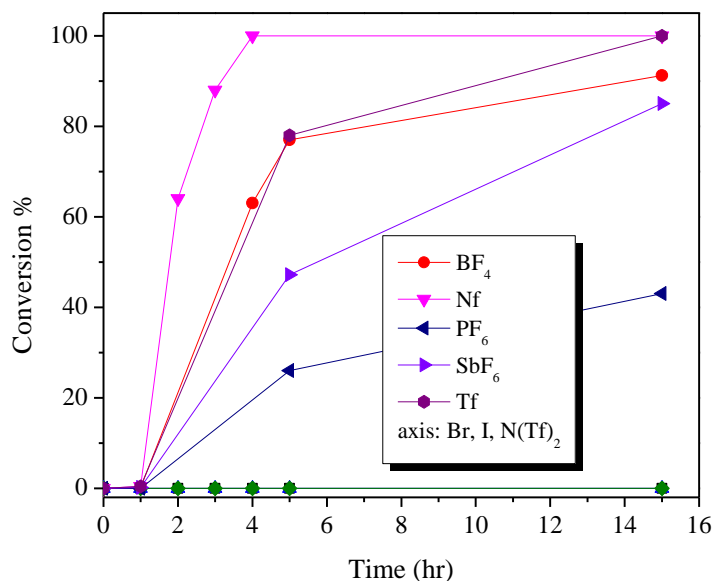


Figure 4.2. Kinetics of polymerization of CHO by MHQ+ Br-(filled squares), BF₄-(filled circles), I- (hexagons), Nf-(pink triangles), N(Tf)₂-(open triangles), PF₆-(blue triangles), SbF₆-(purple triangles), Tf-(purple circles).

sulfonyl counteranions, nonaflate ($C_4F_9SO_3^-$, Nf) and triflate ($CF_3SO_3^-$, Tf), produced the fastest polymerization rates. The more weakly coordinating⁶ fluorinated counteranions,

tetrafluoroborate, hexafluoroantimonate, and hexafluorophosphate, did in fact initiate polymerization, however, at slower rates compared to Nf and Tf. No reaction occurred in the presence of the non-fluorinated salts, iodide and bromide, or in the presence of the amide ionic liquid salt, bis(trifluoromethylsulfonyl)amide.

A strong solvent-dependence was also noted. The reaction occurred neither in polar protic solvents, such as alcohols, nor in polar aprotic solvents such as DMSO. A separate study demonstrated that these solvents quench the emission of MHQ (See Chapter 5) and this phenomenon is most likely related to the lack of photopolymerization reactivity in these solvents. Curiously, the reaction was quenched by very small additions (<10 vol%) of acetonitrile, a solvent which does not quench the emission. The reaction readily occurs in acetone, and therefore all of the studies were performed in acetone.

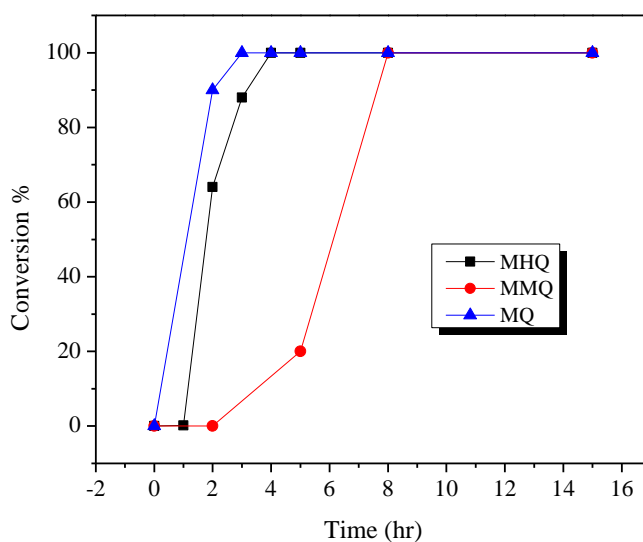


Figure 4.3. Kinetics of polymerization of CHO by MHQ (squares), MMQ (circles) and MQ (triangles).

Upon irradiation of the methyl ether derivative, MMQ-Nf, under the same conditions as MHQ-Nf, conversion to the polymer occurred; however, a very long induction period was observed (Figure 4.3). To test the possibility of latent acid formation, the MHQ salt was irradiated and CHO added after the light was turned off. Under these conditions polymerization still occurred. Upon irradiation of tetrabutylammonium triflate with CHO, no conversion to polymer was detected. Finally, in order to definitively rule out ESPT as the mechanism of polymerization, experiments were attempted using the nonaflate salt of N-methylquinolinium (MQ) as the catalyst. MQ did in fact initiate the polymerization of CHO. A comparison of the kinetics of the three different quinolinium derivatives can be seen in Figure 4.3. The reaction rates and most specifically, the induction times are dependent on the substituent in the 6-position. The catalysis mechanism clearly involves the fluorinated counteranion, along with direct irradiation of a quinolinium salt without any free acidic protons being a requirement. Further, the study suggests that the reaction is solvent-mediated as the polymerization only occurs in acetone. The possibility of the acetone triplet state was explored by irradiating the solution with a filter that cut out wavelengths under 350 nm, thus disallowing acetone from any light absorption. The polymerization still occurred under these conditions.

In order to further explore the mechanism of catalysis, several pH studies were performed. A significant decrease in pH upon irradiation was observed for compounds with fluorinated counteranions (Figure 4.4). Irreversible acid was generated for all three quinolinium compounds studied. The photolysis of MQ resulted in a lower pH than MHQ, where MMQ produced the least amount of protons. Further, a larger pH decrease was observed in the presence of CHO for all systems. The production of irreversible acid

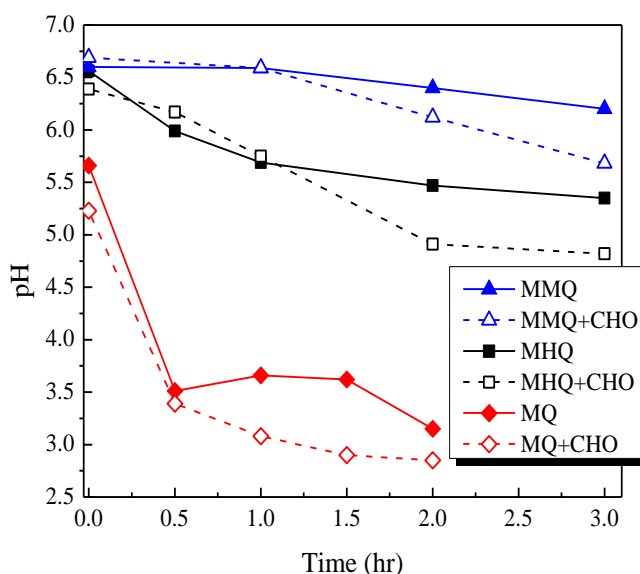


Figure 4.4. pH change upon irradiation of MHQ and its derivatives with and without CHO in acetone.

upon photolysis of these salts indicates that ESPT is not the cause of the polymerization and that some irreversible photodegradation is responsible for the reaction. Exhaustive irradiation of the quinolinium salts in the absence of monomer, however, failed to reveal any detectable photoproducts.

The observation by Hino and Endo⁴ that only fluorinated phenols catalyze the polymerization of GPE led us to question the mechanism, proposed by Hino and Endo, of direct ESPT-induced polymerization. While Hino and Endo claim that the polymerization

occurs through direct ESPT, our results indicate that permanent acid formation causes the polymerization. Pre- and post-irradiation pH measurements were done and a considerable drop in pH was observed for all polymerization-initiating compounds (Figure 4.5). Further, the long-initiation time of 3,5-bis(trifluoromethyl) phenol that Hino observed corresponds to the long irradiation time needed to observe a significant pH drop observed in our laboratory.

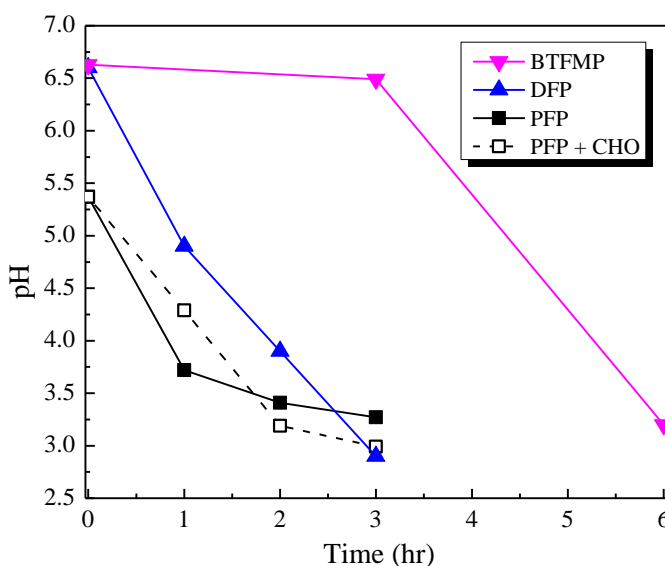


Figure 4.5. pH change upon irradiation of pentafluorophenols in acetone.

The photoinduced defluorination of several fluorine-containing compounds is known,⁷⁻¹⁰ and therefore the dependence on fluorine containing counteranions led to the consideration that HF may be the catalytic acid. The production of fluoride ions was measured by a fluoride ISE and shown to be 1×10^{-4} M fluoride. However, fluoride was not detected via ^{19}F NMR or via mass spectrometric analysis.

Discussion and Conclusions

The primary distinction between an ESPT-catalyzed and a PAG-catalyzed polymerization is the production of a latent acid. In PAG-catalyzed reactions, the acid is produced irreversibly, sometimes in a latent form which must be revealed by heating, e.g., “post-exposure baking”, or PEB. Polymerization resulting from production of a latent acid is almost invariably accompanied by an induction period, during which the acid concentration increases sufficiently to initiate polymerization. Notably, the shortest induction period occurs for MQ, which has no obvious proton for ESPT-initiated polymerization. In the case of acetonitrile, which quenches polymerization without quenching fluorescence, preferential solvation by acetonitrile may occur, making the photoacid unavailable for polymerization. It is also possible that acetonitrile, an uncommon solvent for cationic polymerization, terminates the reaction by reacting with the growing chain through a nucleophilic process.

A remaining question is the source of the proton and the identity of the counterion. A surprising, and still unexplained phenomenon is the failure of non-fluorinated counterions to sustain polymerization. Rates of cationic polymerization are known to be strongly anion dependent.¹¹ However, this is not entirely unexpected due to the low concentration of fluoride determined by the ISE and the relatively modest pH change produced by photolysis. If F^- were present, it could only be produced by decomposition (reduction or hydrolysis) of the counterion. It has been previously shown that a very strong reductant is needed to reduce perfluorinated alkyl sulfates, such as a solvated electron.¹² There is no obvious source for such a stronger reductant in this system, where the singlet excited-state quinolinium radical has been reported to have a

reduction potential of 2.7 V (vs. SCE), making it a very powerful oxidant.¹³ If in fact free fluoride is present, it is most likely a secondary reaction and not responsible for the polymerization. The counteranions which are not perfluorinated alkane sulfonates (PF_6^- , SbF_4^- , BF_4^-) are better sources of fluoride and the reaction is slower using salts with these counterions. This suggests that even if fluoride is present, that it is not playing a role in the polymerization. Rather, the failure of some counterions to initiate polymerization may reflect strong ion-pairing in acetone solvent.

Several other mechanisms for the production of protons are possible. Proton abstraction from the MHQ methyl group could occur and may possibly go undetected by NMR, since only catalytic amounts are needed to initiate the reaction. Noting that more

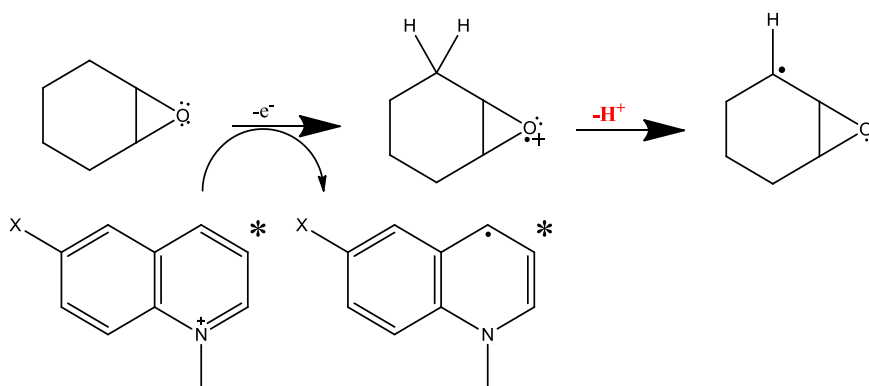


Figure 4.6. Proposed mechanism of acid production via electron transfer from CHO to MQ followed by proton abstraction from CHO.

protons are produced in the presence of CHO, it is possible that there are two mechanisms of acid formation. Electron transfer from the CHO to the quinolinium may occur which would then be followed by a proton abstraction from the CHO (Figure 4.6). The initial excited-state electron abstraction from CHO would not be surprising since it is known that MQ derivatives exhibit an enormous electron affinity upon photoexcitation.¹⁴

We note that photoinitiation by photoacid generators has been the subject of numerous investigations, and that the mechanisms in even the most widely-used commercial examples have been the subject of controversy.¹⁵

Chemistry involving the excited state of acetone was studied by Porter and coworkers¹⁶ and the necessity for acetone as a solvent in the reaction lead us to consider a mechanism involving acetone as an indirect electron donor (Figure 4.7). Acetone is a very good hydrogen atom abstractor,¹⁵ so it is possible that a hydrogen is abstracted from a quinolinium or CHO molecule, thus forming the acetone ketyl radical, which then donates an electron to the excited-state quinolinium, forming protonated acetone, a very good proton source. However, the use of filters to exclude light absorption by acetone suggests that its excited state does not play a role.

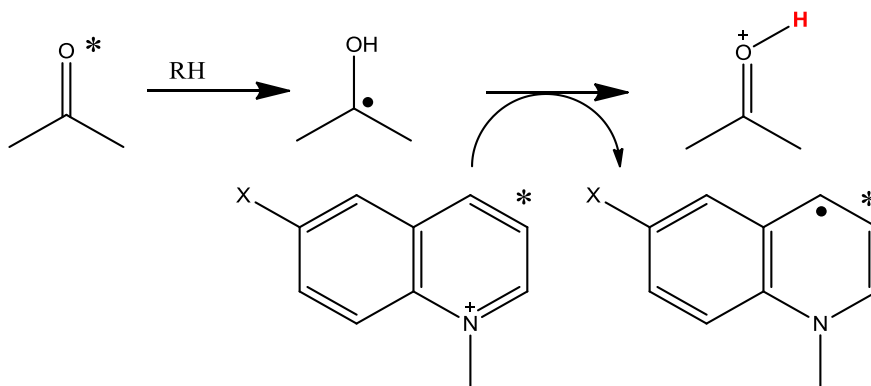


Figure 4.7. Proposed mechanism of acid production via excited-state acetone.

Aromatic fluoroorganics are known to undergo light-induced defluorination. In 1968 Seiler et al. first reported⁷ a hydrolysis mechanism for trifluoromethyl phenols; later Seiler and Wirtz reported⁸ the mechanism for various trifluoromethyl 1-naphthol derivatives. In 1997, Dubnack and Kreisel reported⁹ the photolytic degradation of mono-

and difluorophenols. Subsequently, in 2009, Dichiarante et al. reported the UV-light-induced defluorination of para-fluorophenol.¹⁰ Further, the reductive defluorination of aqueous perfluorinated alkyl surfactants was reported by Park et al. in 2009.¹² The mechanism involved the production of aquated electrons generated from the photolysis of iodide followed by the reduction of the perfluorinated alkanes. These results led us to question Hino's results and to perform the missing control experiments. We are forced to conclude that, in this case as well, the proposed ESPT-initiation, in fact, involves latent acid formation.

The photoinduced CHO polymerization by various *N*-methylquinolinium salts occurs via photodegradation of the acid generator involving both the quinolinium component and a fluorinated counteranion. Through pH studies and other controls, these studies have shown that direct ESPT is not responsible for the polymerization in these salts. Contrary to previous reports, this research also indicates that the photopolymerization of various fluorophenols is also due to degradation of the phenol and presumably loss of the fluoride ion, thus generating the true catalyst, HF. ESPT-induced polymerization is still an unproven technology, and such claims must be met with caution, particularly when proper controls are absent, i.e., irradiation in the absence of monomer followed by addition of monomer in the dark to test for the production of latent acid. The steady-state production of protons, even with a high-yield reversible photoacid, is necessarily a convolution of the light intensity and the lifetime of the protons produced. Invariably, such production is a minor perturbation of the unirradiated pH.

References

1. Recent reviews: (a) Prabhu, V. M.; Kang, S. H.; VanderHart, D. L.; Satija, S. K.; Lin, E. K.; Wu, W. L. *Adv. Mater.* **2011**, *23*, 388. (b) Nishikuboand, T.; Kudo, H. *J. Photopolym. Sci. Technol.* **2011**, *24*, 9.
2. (a) Wei, Y.; Wang, W.; Yeh, J.M.; Wang, B.; Yang, D.C.; Murray, J.K. *Adv. Mater.* **1994**, *6*, 372.(b) Harvard, J.M., Yoshida, M.; Pasini, D.; Vladimirov, N.; Frechet, J.M.J.; Medeiros, D.R.; Patterson, K.; Yamada, S.; Willson, C.G.; Byers, J.D.J. *Polym. Sci. Part A: Polym. Chem.* **1999**, *37*, 1225. (c) Yu, H.S.; Yamashita, T.; Horie, K. *Macromolecules* **1996**, *29*, 1144. (d) Chae, K.H.; Park, I.J., Choi, M.H. *Bull. Korean. Chem. Soc.* **1993**, *14*, 614. (e) Kim, S.T.; Kim, J.B.; Chung C.M.; Ahn, D.D. *J. Appl. Polym. Sci.* **1997**, *66*, 2507. (f) Chen, J.P.; Goa, J.P.; Wang, Z.Y.J. *Poly. Sci., Part A: Polym. Chem.* **1997**, *35*, 9. (g) Kim, H.K.; Ober, C.K. *Polym. Bull.* **1992**, *28*, 33. (h) Ito, H. *Adv. Polym. Sci.* **2005**, *172*, 37.
3. Crivello, J.V.; Lam, J.H.W. *Polym. Sci. Polym. Chem. Ed.*, **1980**, *18*, 1021.
4. Hino, T.; Endo, T. *Macromolecules* **2004**, *37*, 1671.
5. Odian, G. *Principles of Polymerization*, 4th ed; John Wiley & Sons: New Delhi, **2004**; Ch. 7, pp. 544-569.
6. Koppel, I. *J. Am. Chem. Soc.*, **2000**, *122*, 5114
7. Grinter, R.; Heilbronner, T.; Petrzilka, T.; Seiler, P. *Tetrahedron Lett.* **1968**, *9*, 3845.
8. Seiler, P.; Wirz, J. *Tetrahedron Lett.* **1971**, *20*, 1683.
9. Dubnack, K.; Kreisel, G. *Z. Umweltchem. Okotox.* **1997**, *9*, 303.
10. Dichiarante, V.; Fagnoni, M.; Albini, A. *Green Chem.* **2009**, *11*, 942.

11. Lawson, R. A.; Lee, C.-T.; Tolbert, L. M.; Henderson, C. L. *Microelec. Eng.* **2009**, 86, 738.
12. Park, H.; Vecitis, C. D.; Cheng, J.; Choi, W.; Mader, B. T.; Hoffmann, M. R. *J. Phys. Chem. A* **2009**, 113, 690.
13. Guirado, G.; Fleming, C. N.; Lingenfelter, T. G.; Williams, M. L.; Zuilhof, H.; Dinnocenzo, J. P. *J. Am. Chem. Soc.* **2004**, 126, 14086.
14. Ohkubo, K.; Kobayashi, T.; Fukuzumi, S. *Angew. Chem. Int. Ed.* **2011**, 50, 8652.
15. (a) Crivello, J. V. *J. Polym. Sci., Part A: Polym. Chem.* **1999**, 37, 4241. (b) Hacker, N. P.; Hofer, D. C.; Welsh, K. M. *J. Photopolym. Sci. Technol.* **1992**, 5, 35. (c) Ito, H.; Willson, C. G. *ACS Symp. Ser.* **1984**, 242, 11. (d) Kasapoglu, F.; Aydin, M.; Arsu, N.; Yagci, Y. *J. Photochem. Photobiol. A.* **2003**, 159, 151. (e) Lee, M. S.; Frechet, J. M. J. *Polym. Mater. Sci. Eng.* **1993**, 68, 32. (f) Tagawa, S.; Nagahara, S.; Iwamoto, T.; Wakita, M.; Kozawa, T.; Yamamoto, Y.; Werst, D.; Trifunac, A. D.. *SPIE-Int. Soc. Opt. Eng.* **2000**, 3999, 204. (g) Tsuda, M.; Oikawa, S. *J. Photopolym. Sci. Technol.* **1990**, 3, 249. (h) Welsh, K. M.; Dektar, J. L.; Hacker, N. P.; Turro, N. *Polym. Mater. Sci. Eng.* **1989**, 61, 181.
16. Porter, G.; Dogra, S. K.; Loutfy, R. O.; Sugamori, S. E.; Yip, R. W. *J. Chem. Soc., Faraday Trans. 1* **1973**, 69, 1462.

Part II. A Fluorescence Tool for Understanding ESPT in Supercritical Media

Introduction

Supercritical carbon dioxide (scCO₂) is a liquid-like form of carbon dioxide when it is held above the critical temperature and pressure of CO₂. It is becoming an important “green” solvent in industrial processes due to its low environmental impact and toxicity.¹ scCO₂ is growing in importance as a processing solvent and as a reaction medium, where the addition of cosolvents can tailor the properties of scCO₂. Thus, there has been some study on the ESPT of “super” photoacids in the medium.^{2,3} ESPT in MeOH/CO₂ mixtures was attempted using 2-naphthol and 5-cyano-2-naphthol, but the authors failed to detect any naphtholate emission, thus ruling out the possibility of ESPT under the reported conditions.^{4,5} Previous work by Nunes, et al. showed that ESPT is in fact possible in gas expanded liquids, however it is tied to the much higher excited-state acidity of the “super” photoacid DCN2.² They observed that while DCN2 has only one emission band in scCO₂, upon addition of MeOH, a naphtholate emission band was observed, confirming ESPT in the system. ESPT was noted even at very low concentrations of methanol and attributed to MeOH aggregates and the preferential solvation of DCN2 by those aggregates. They also reported that while temperature plays only a small role in the system, an increase in pressure significantly decreases the proton transfer rate as observed by a decrease in the fluorescence intensity ratios of $^*RO-/^*ROH$ while observing a significant increase in the *ROH emission. The effect of pressure on the ESPT of DCN2 in pure methanol was also reported by Huppert et al.^{6,7} who observed that the proton transfer rate increased with pressure at low pressures, while at high pressures the rate constant decreased as the pressure increases. They suggested an analogous two-

coordinate mechanism to the temperature dependence described in Chapter 3, Section II. They also reported an increase in the *ROH fluorescence intensity with pressure. While Nunes and coworkers attributed the increase in *ROH fluorescence to less efficient ESPT, Huppert and coworkers suggested the presence of more efficient proton tunneling at higher pressures. Nunes et al. explained the disagreement by the high compressibility of the MeOH/CO₂ mixtures. The authors suggested that the pressure would actually disrupt the MeOH clusters rather than decrease the distance between the methanol and DCN2 molecules. These discrepancies can be attributed to the substantial difference on the ESPT of DCN2 between pure MeOH and in scCO₂ mixtures as a function of pressure.

MHQ was of interest for use as a probe in the scCO₂ system because of its extremely strong photoacidity. We have previously shown that the ESPT rates of MHQ have a strong response to the solvent environment and therefore we were interested to see if MHQ would provide any insight into the microheterogeneous environment of scCO₂ mixtures. Methanol/dioxane mixtures have been shown to have similar dielectric constants to gas-expanded MeOH mixtures⁸ and therefore the ESPT of MHQ was monitored in mixtures of MeOH/dioxane with varying compositions.

Experimental Protocols

The ESPT reaction of MHQ in MeOH/CO₂ was studied using methanol mole fractions ranging from 0.4 – 0.7. Mole fractions were calculated from the MeOH volume in the cell at room temperatures and the density of MeOH/CO₂ mixtures at the defined temperature.⁹ Steady state and time resolved fluorescence measurements were taken with

pressures ranging from 100 – 250 bar and temperatures ranging from 307 – 330 K. Visual inspection ensured the presence of a one phase homogeneous system. For these measurements, MHQ was dissolved in methanol and added to the desired quantity of the solution in a high-pressure cell. The cell was cooled to 190 K and evacuated to less than 1 Pa for 30 min. The cooled cell was pressurized and brought to the desired temperature. Each experimental run started at the highest temperature and lowest pressure. Cooling and CO₂ pressure adjustments were made between the measurements to construct a grid with pressure, temperature and composition as variables. The experimental error with each run was relatively small, but larger experimental errors must be included in the comparison between independent runs. These larger experimental errors are associated with the inaccuracies in estimation of methanol concentration following the removal of the air dissolved in the methanol and its evaporation, while the system was under vacuum at low temperatures.

Fluorescence decay times with picoseconds time resolution were obtained by using a home-built picosecond time-correlated single photon counting (TCSPC) apparatus. The excitation source consisted of a picosecond Spectra Physics mode-lock Tsunami laser (Ti: sapphire) model 3950 (repetition rate of about 82 MHz, tuning range 700-1000 nm), pumped by a Millennia Pro-10s, frequency-doubled continuous wave (CW), diode-pumped, solid-state laser (λ_{em}) 532 nm). A harmonic generator model GWU-23PS (Spectra-Physics) was used to produce the second and third harmonic from the Ti:sapphire laser exciting beam frequency output. The samples were measured with excitation at 395 nm and the horizontally polarized output beam from the GWU (second harmonic) was first passed through a ThorLabs depolarizer (WDPOL-A) and after by a

Glan-Thompson polarizer (Newport 10GT04) with vertical polarization. Emission at 90° geometry collected at magic angle polarization was detected through a double subtractive Oriel Cornerstone 260 monochromator by a Hamamatsu microchannel plate photomultiplier (R3809U-50). Signal acquisition and data processing were performed employing a Becker & Hickl SPC-630 TCSPC module. Fluorescence decays and the instrumental response function (IRF) were collected using 4096 channels in a 0.814 ps/channel scale, until 5×10^3 counts at maximum were reached. The full width at half-maximum (fwhm) of the IRF was about 22 ps and was highly reproducible with identical system parameters.

The temperature dependence of the ESPT reaction of MHQ in MeOH/dioxane mixtures was also studied using methanol mole fractions ranging from 0.4 – 0.7 and using temperatures from 283 – 333 K. The steady-state emission was obtained on a Horiba Jobin Yvon Fluorolog 2 Spectrophotometer. Fluorescence spectra were collected at a right angle from the excitation source. The excitation source was a 1000 W high-pressure Hg-Xe lamp. Entrance and exit slits were set to 1.5 mm. All spectra were collected in quartz cuvettes. Fluorescence emission spectra were excited at the maximum absorption wavelength.

Spectroscopic grade, extra-dry organic solvents were used from commercial sources without further purification.

All of the MeOH/scCO₂ measurements were performed in the laboratory of Dr. Luis Arnaut at University of Coimbra by Rui Nunes.

Results

Steady-state behavior

As discussed previously, the MHQ emission in pure alcohols, including MeOH, exhibits dual emission: the band at 460 nm is assigned to C^* and the red-shifted band at 610 nm is assigned to Z^* (Figure 3.5). The steady-state emission of MHQ in MeOH/scCO₂ (Figure 4.8) also shows two fluorescence bands, indicating that the ESPT reaction occurs under these conditions. The C^* maximum is at 445 nm which shifts to longer wavelengths with increasing temperature, while the Z^* maximum shows no shift with temperature. The overall emission in the system decreases with increasing temperature.

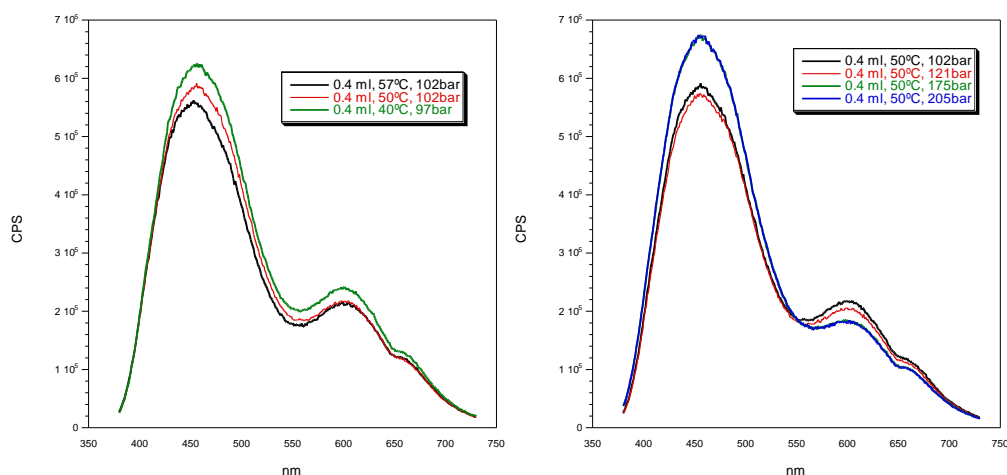


Figure 4.8. Steady-state emission of MHQ in MeOH/scCO₂ at various temperatures (left) and pressures (right) ($X_{\text{MeOH}} = 0.66, 0.65, 0.60$).

Increasing the pressure in the system causes no shift in the C^* emission band, however a slight increase in C^* and decrease in Z^* emission is observed with increasing pressure.

The steady-state behavior of MHQ in MeOH/dioxane ($X_{\text{MeOH}} = 0.60$) is presented in Figure 4.9. Similar to the behavior of MeOH/scCO₂ mixtures, the C* band is slightly red-shifted compared to MHQ in pure MeOH and the overall emission of MHQ in MeOH/dioxane decreases with increasing temperature.

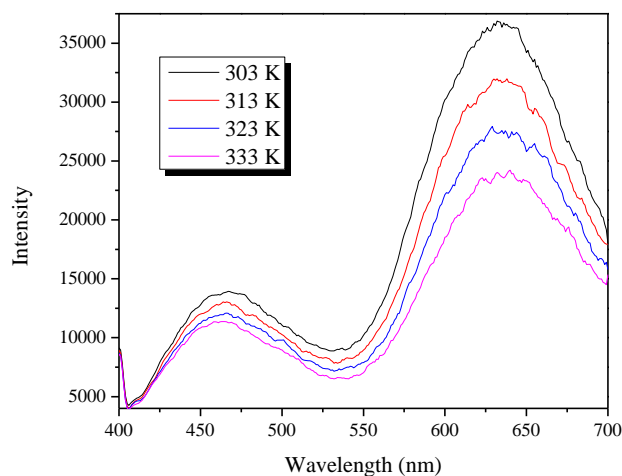


Figure 4.9. Steady-state emission of MHQ in MeOH/dioxane ($X_{\text{MeOH}} = 0.60$) at various temperatures.

Kinetic behavior

Figure 4.10 shows the C* decays, monitored at 450 nm of MHQ in MeOH/scCO₂ mixtures where each graph represents a different volume of MeOH. At short times ($t < 1.25$ ns), the kinetic behavior for all curves within the same volume of MeOH is nearly the same. For longer times ($t > 1.25$ ns) the amplitude of the longer-lifetime tail changes upon addition of CO₂.

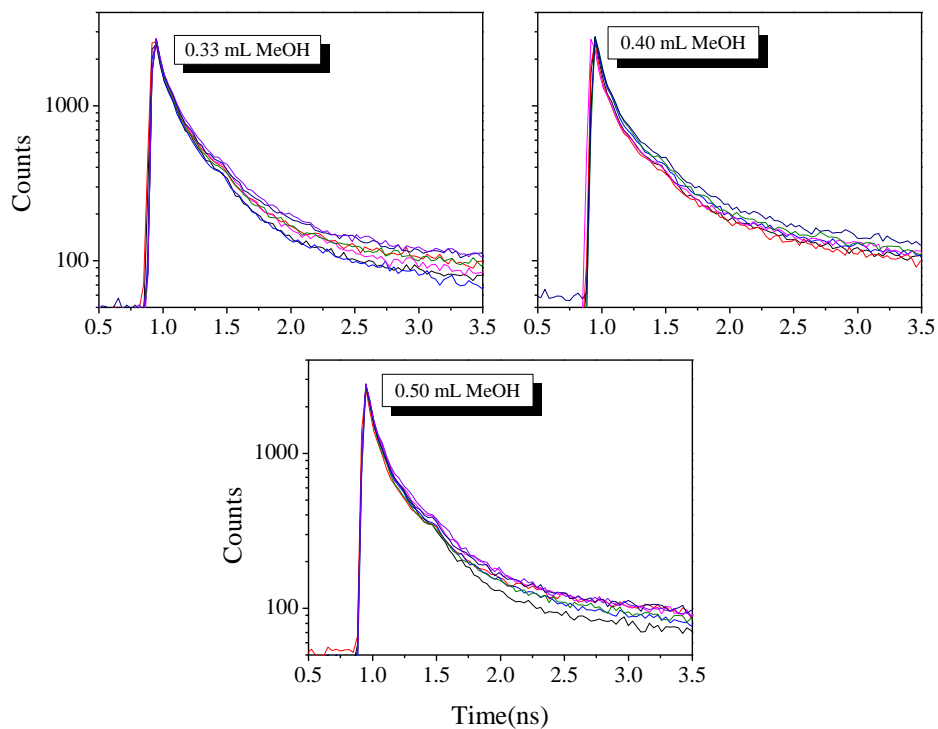


Figure 4.10. C^* (450 nm) decays of MHQ in MeOH/scCO₂. X_{MeOH} : 0.25-0.61
Pressure:129-215 bar; Temperature: 313-300K.

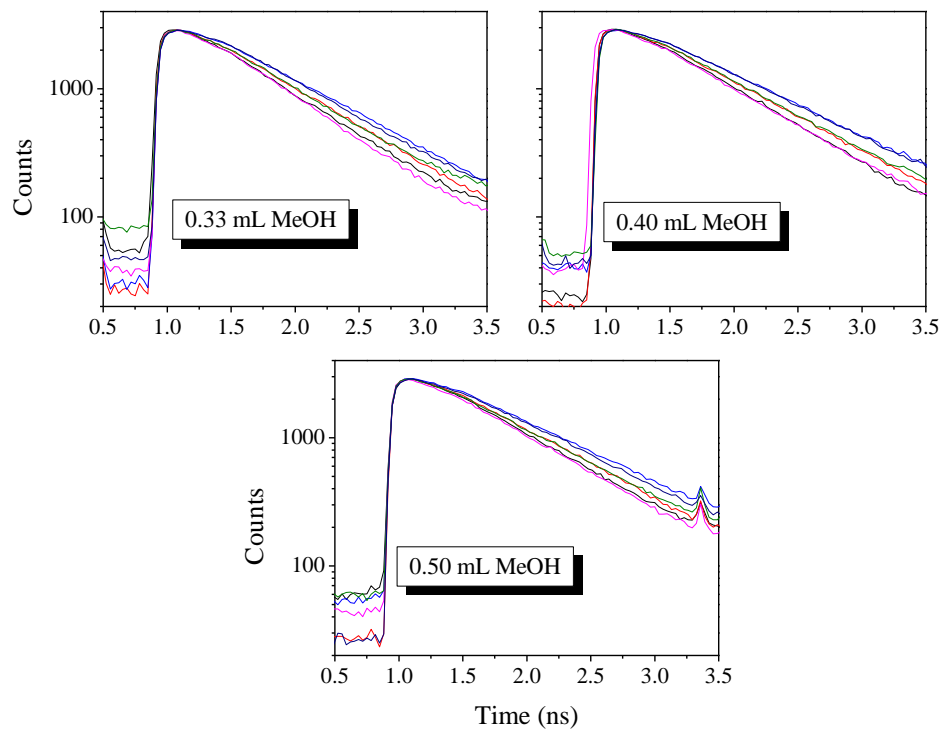


Figure 4.11. Z^* (610 nm) decays of MHQ in MeOH/scCO₂. X_{MeOH} : 0.25-0.61
Pressure:129-215 bar; Temperature: 313-300K.

Figure 4.11 shows the analogous Z^* decays monitored at 610 nm. While the shapes of the curves do not change, the Z^* decays change more dramatically than the C^* decays with the introduction of CO_2 into the system.

Figure 4.12 shows the C^* decays of MHQ, monitored at 450 nm, in MeOH/dioxane mixtures. The various graphs represent different temperatures. The C^* decays do not change significantly as a function of temperature. For all X_{MeOH} , the very short time decays ($t < 0.3$ ns) do not change significantly, however the amplitude of the decays at $t > 0.3$ ns increases for $X_{\text{MeOH}} = 0.55$. Of note is the behavior of $X_{\text{MeOH}} = 0.72$ at

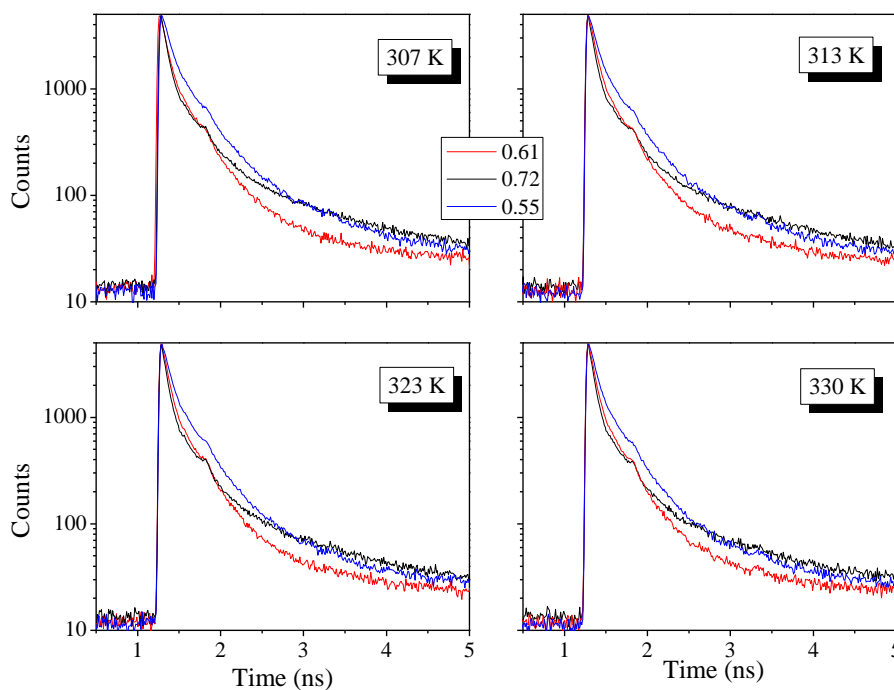


Figure 4.12. C^* (450 nm) decays of MHQ in MeOH/dioxane. X_{MeOH} : 0.55-0.72; Temperature: 307-330 K.

$t > 2$ ns, where the amplitude of a long-time decaying species is much greater than for the lower mole fraction samples.

Figure 4.13 shows the Z^* decays at different temperatures for the same system where each graph represents a different mole fraction of MeOH. Unlike C^* , the kinetics do not change with X_{MeOH} , however the decays are temperature dependent. The lifetime of Z^* appears to decrease with increasing temperature.

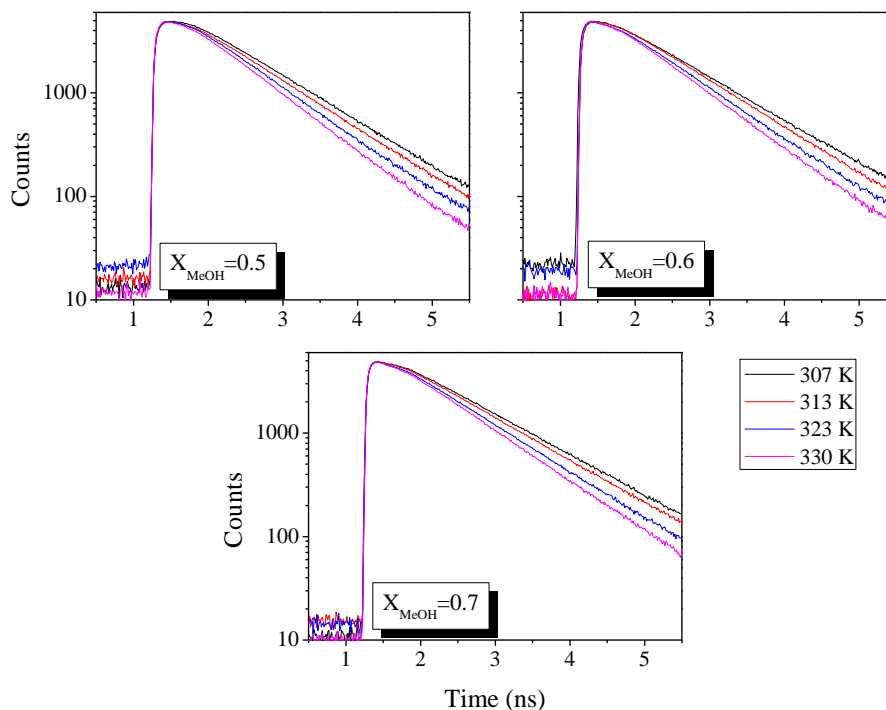


Figure 4.13. Z^* (610 nm) decays of MHQ in MeOH/dioxane. X_{MeOH} : 0.50-0.70; Temperature: 307-330 K.

The kinetic data were fit using the SSDP software package. The full table of parameters and fit figures can be found in Appendix B. Several different approaches were used in an attempt to fit the kinetics in these systems. For the MeOH/scCO₂ system, visual inspection of the decays indicates that the protolytic dissociation rates, k_d , should

be constant. It is also clear from inspection that the recombination (association) rates, k_r , vary only slightly. The first attempt at fitting the kinetics involved keeping k_d and k_r constant while using Debye radii (R_D) values calculated from the literature values of the dielectric constants under these conditions. (For full explanation of parameters, see Chapter 3, Section II and Appendix C). To accurately fit the system, the diffusion coefficient, D , had to be increased substantially from the coefficient D of MHQ expected in pure MeOH. The diffusion coefficient in pure MeOH was derived from the value of 5-cyano-2-naphthol in MeOH as reported by Solntsev et al.¹⁰ and then decreased by one-half according to the findings discussed in Chapter 3, Section II. It is unlikely that D would increase under these conditions because injecting CO_2 into the system would break the MeOH/proton network, therefore if D does vary from that of pure MeOH, one would expect it to be lower than that in pure MeOH.

The second fitting attempted to keep the diffusion coefficients lower than the expected D of MHQ in pure MeOH. In order to keep such a low D , R_D had to be lowered substantially from literature values. Unfortunately, the fits using these parameters were not very good and it appeared as though 3 kinetic parameters were required to reproduce the shape of the C^* as it was impossible to fit accurately solely using k_d and k_r .

The final attempt involved keeping the diffusion coefficient constant at the value expected for MHQ in pure MeOH ($1.85 \times 10^{-5} \text{ cm}^2/\text{s}$). The diffusion was kept constant under the assumption that D does not change in this temperature range, as was observed in Chapter 3, Section II. The R_D values were calculated from the dielectric constants in pure MeOH at the appropriate temperatures. Using this rationale, the kinetics of MHQ in

both gas-expanded MeOH and MeOH/dioxane mixtures were fit with excellent results (See Appendix B).

Discussion and Conclusions

Steady-state behavior

A red fluorescence shift of 1000 cm^{-1} has been attributed to the formation of a hydrogen bond in basic solvents.¹⁰ However, this explanation does not seem plausible under these conditions because the isothermal pressure change, essentially a dilution of MeOH, does not cause any shift or any change in the half-height bandwidth in the system. The dielectric constant of MeOH/scCO₂ mixtures decreases with rising temperature as a result of changes in the permanent dipole concentration and specific interaction, such as H-bonding and pair wise association.¹¹ These types of interactions are important in systems such as MHQ where polar and charged groups are present; the blue-shift observed for the MHQ fluorescence could be due to a decrease of the solvation capacity of MeOH as a function of the decreased dielectric constant. However, changing the pressure in the system does not cause a similar effect, which suggests that the change in the dielectric constant does not affect the fluorescence emission of MHQ in MeOH/scCO₂. From the normalized emission of MHQ at various pressures (Figure 4.14), a slight decrease in ESPT efficiency is observed as a decrease in the Z* emission. Increasing the pressure in these systems can be understood as a dilution of MeOH, and therefore a decrease in ESPT is expected under these conditions.

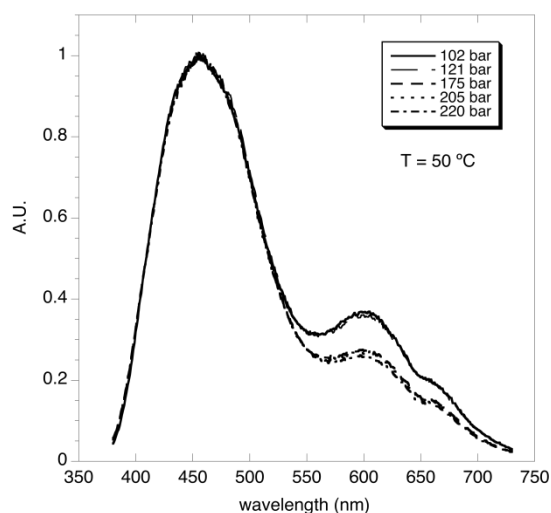


Figure 4.14. Normalized steady-state emission of MHQ in MeOH/scCO₂ mixtures at various pressures.

The overall decrease in emission as a function of increasing temperature is expected. Fluorescence intensity is known to be sensitive to changes in temperature.¹² In general, as temperature increases, emission decreases due to an increase of temperature dependent non-radiative rate constants. The overall rate constants generally increase with temperature, so any fluorescence quenching process that may be occurring may be sped up by the increase in temperature. Further, MHQ is known to be quenched by MeOH. The ESPT in MeOH/dioxane is roughly twice as efficient as the ESPT in MeOH/scCO₂, as measured by the ratio of Z*/C* fluorescence intensities. The ESPT process is expected to be less efficient in the scCO₂ medium because the supercritical fluid may break up the methanol regions, which is the only area in which the ESPT can occur.

MHQ in MeOH/scCO₂

The rationale for the fittings described above can be explained in terms of preferential solvation of MHQ by MeOH. Presumably, the amount of methanol is high enough that the preferential solvation by MeOH overcomes any breaking of the MeOH/proton network. That is, the system is solely in the exergonic regime.

According to the analysis above, the protolytic dissociation rate, k_d , should not be affected by the introduction of CO₂ into the system. In fact, k_d , as determined by the SSDP fits, remains constant for each volume of methanol due to the very strong preferential solvation by MeOH. (Table 4.1) There is no apparent trend in the k_d as a function of volume of MeOH, and the values are within a ~20% range, suggesting that the differences are due to experimental error as the different volumes of MeOH represent different samples.

Table 4.1. Protolytic dissociation constants, k_d , for MHQ in MeOH/scCO₂

Vol MeOH (mL)	k_d
0.33	12.0
0.40	14.6
0.50	13.0

The dissociation rate was compared to the ratio of $Z^*/C^*\tau_{Z^*}$, emission intensities from the steady-state data. The lifetime of Z^* was accounted for according to Eq. 2.1. Figure 4.15 shows the effective ESPT rate as determined by both methods as a function of temperature (Arrhenius plots) where each graph represents a different volume of MeOH. The steady-state data correlate well with the time-resolved data where the dissociation rate is independent of temperature under these conditions. The slopes of the Arrhenius plots from the time-resolved data are constant at zero, however very small slopes are calculated from the steady-state data (Table 4.2). The reason for these differences in slopes can be explained by the varying association rate constants, k_r . The

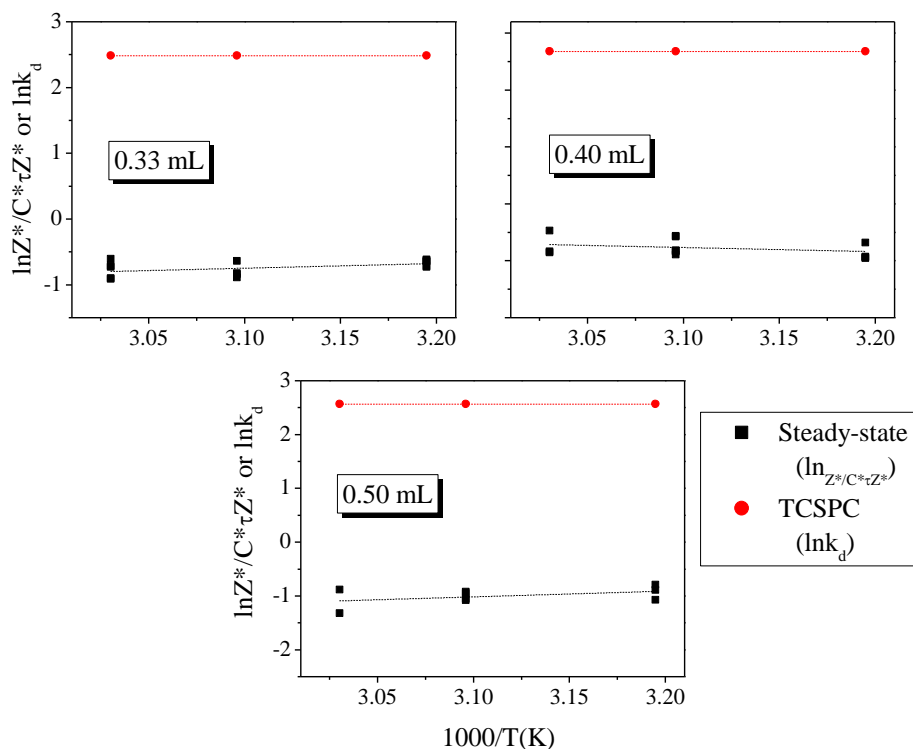


Figure 4.15. Arrhenius plots for MHQ in MeOH/scCO₂ mixtures as determined by steady-state and time-resolved measurements.

values for k_f and k'_f from Eq. 2.1 are unknown, accounting for the differences in the values of the overall rates (Figure 4.15, y-axis). The relative independence of k_d on temperature is not unexpected and in fact, Nunes et al.² reported the same phenomenon for the “super” photoacid DCN2.

Table 4.2. Slopes of Arrhenius plots for MHQ in MeOH/scCO₂.

Vol MeOH	TCSPC	Steady-state
0.33	0	0.70
0.40	0	-0.74
0.50	0	0.90

While the kinetic fits revealed a constant dissociation rate for the ESPT reaction, the recombination rate varied. Figure 4.16 shows the k_r as a function of temperature, X_{MeOH} , and pressure. While no trend is observed with temperature, the recombination rate increases with increasing pressure and decreases with increasing mole fraction of MeOH. The decrease in the rate of recombination with an increase in X_{MeOH} can be thought of in terms of the solvation of the Z^* by MeOH. With less MeOH in the system, there will be less solvation of the Z^* , leading to a faster recombination. The increase in pressure corresponds to a dilution of MeOH, so presumably the increase in k_r could come from the weaker solvation of Z^* by MeOH at higher pressures.

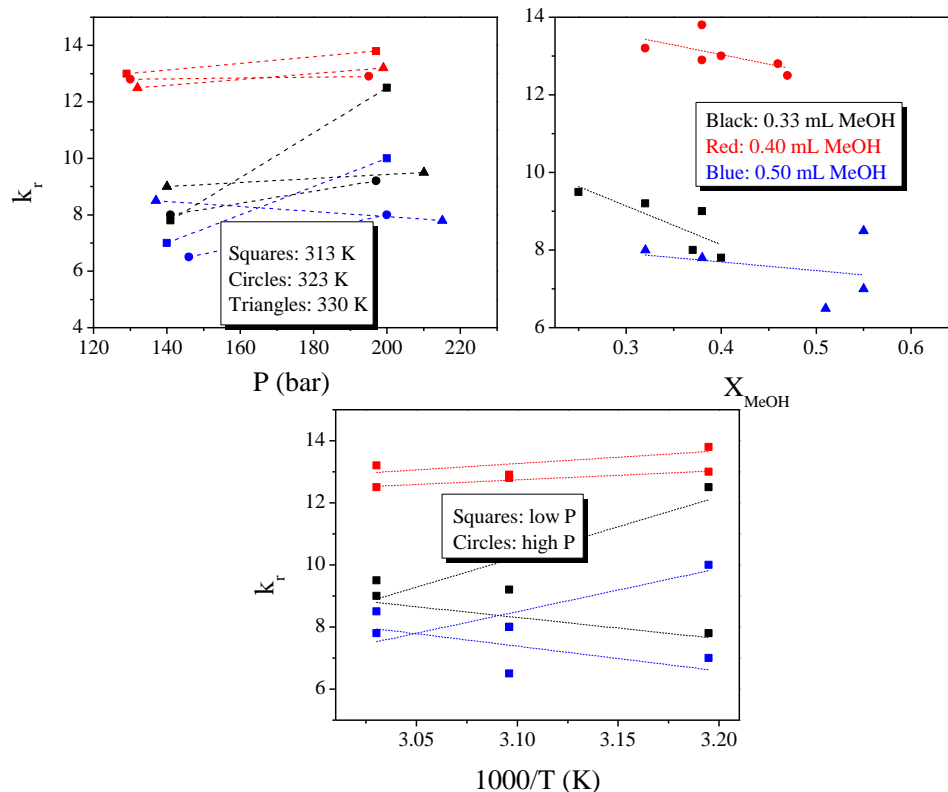


Figure 4.16. MHQ in MeOH/scCO₂: recombination rate, k_r , at various pressures (top left), X_{MeOH} (top right), and T (bottom).

Using the same method described in Chapter 3, Section II, the pK_a^* values were calculated from the kinetic fits and determined to be $-2.2 < \text{pK}_a^* < -2.4$. These values are in good agreement with the idea of a very strong preferential solvation by MeOH, where one would expect the pK_a^* in pure MeOH to be approximately -3 .¹³ While the steady-state spectra show a diminished emission from Z^* , suggesting that such a low pK_a^* value should not be possible, this can be accounted for by the shorter lifetime of the Z^* in scCO₂ mixtures. A shorter lifetime would lead to a smaller yield of Z^* emission in the steady-state spectra. While thermodynamic data can be obtained from the temperature dependent plot of pK_a^* using the Van't Hoff relation, the error associated with the enthalpy and entropy is too great to comment on the magnitude of the parameters.

However, the positive entropic factor and negative enthalpic factor indicate that the reaction is spontaneous (i.e. $\Delta G < 0$) which is consistent with the negative pK_a^* values and with the formation of two species, C^* and Z^* . These results, however, are not consistent with the results for the temperature-dependence of the ESPT in pure alcohols (Chapter 3, Section II). While a positive entropic factor is expected, the enthalpic factor is also expected to be negative, i.e. the reaction is exergonic at high temperature, while at low temperatures $\Delta G > 0$. This discrepancy, however, could be attributed to the very large error associated with the calculations.

MHQ in MeOH/dioxane

Figure 4.17 shows Arrhenius plots for MHQ in MeOH/dioxane mixtures as calculated from steady-state and TCSPC methods. Similarly to the MeOH/scCO₂ systems, k_d is independent of temperature using both methods of calculation. The slopes of the plots using the kinetic data are constant at zero, where a small negative slope is

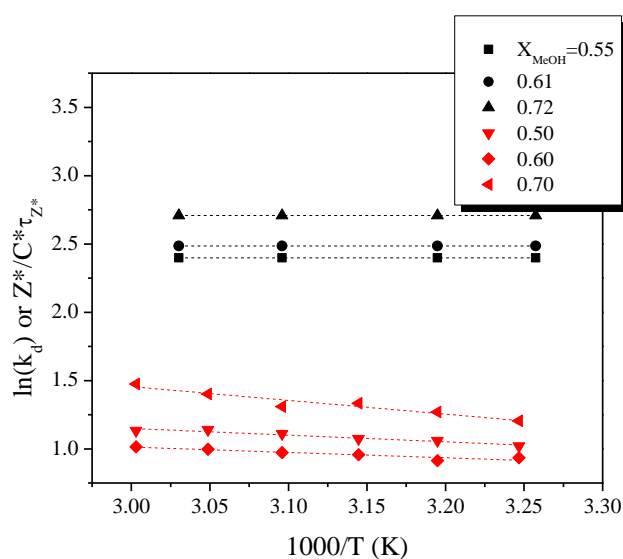


Figure 4.17. Arrhenius plots for MHQ in MeOH/dioxane calculated from steady-state (red) and time-resolved (black) methods.

observed from the steady-state data (Table 4.3). Again, these small slopes can be explained by the slightly varying k_r , as the steady-state data do not account for the recombination rate.

Table 4.3. Slopes of Arrhenius plots in MeOH/dioxane mixtures.

X_{MeOH}	SSDP	Steady-state
0.50	0	-0.43
0.60	0	-0.50
0.70	0	-0.89

Figure 4.18 shows the ESPT as calculated from protolytic dissociation rate constant, k_d , and from the C^* and Z^* fluorescence intensities as a function of MeOH mole fraction. Unlike the gas expanded MeOH, this system shows a relatively strong dependence of k_d on X_{MeOH} where the proton transfer rate increases with methanol mole fraction. This result is consistent with preferential solvation by MeOH where increasing the concentration of MeOH in the system, increases the ESPT rate.

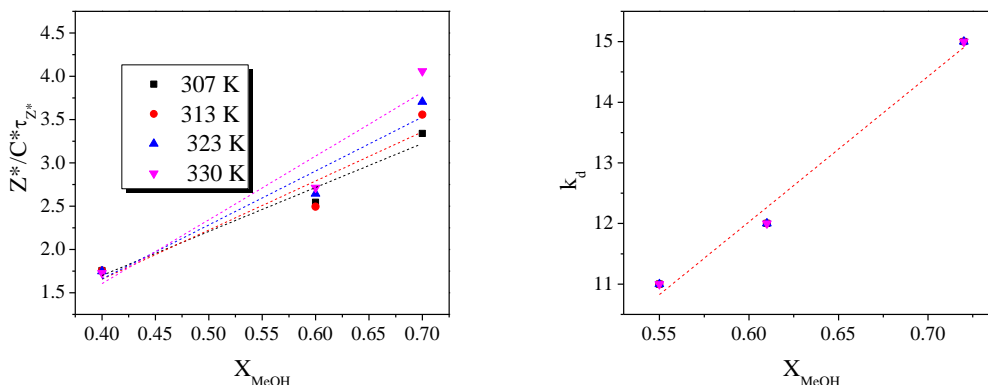


Figure 4.18. MHQ in MeOH/dioxane: ESPT rates, k_d and $Z^*/C^*\tau_{Z^*}$, vs. X_{MeOH} from steady-state (left) and time-resolved (right) methods.

The temperature dependence on the lifetime of Z^* is shown in Figure 4.19. The lifetime of Z^* decreases with increasing temperature. This temperature dependence is not unexpected due to the non-radiative processes causing deactivation through collisions.

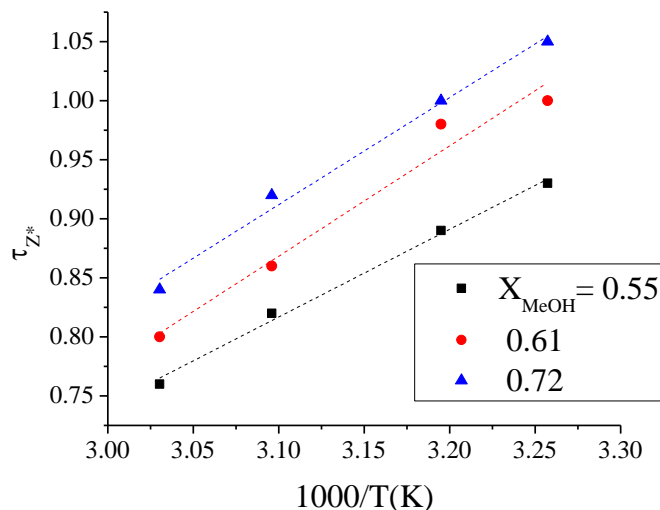


Figure 4.19. MHQ in MeOH/dioxane: Z^* lifetime, τ_{Z^*} , vs. $1000/T$.

A small temperature dependence is observed for the recombination rate in this system (Figure 4.20). The k_r decreases slightly with increasing temperature. However, unlike gas-expanded MeOH, the k_r does not decrease monotonically with mole fraction. This is most likely due to the unexplained odd long-time behavior exhibited by $X_{MeOH}=0.7$ (see Figure 4.12).

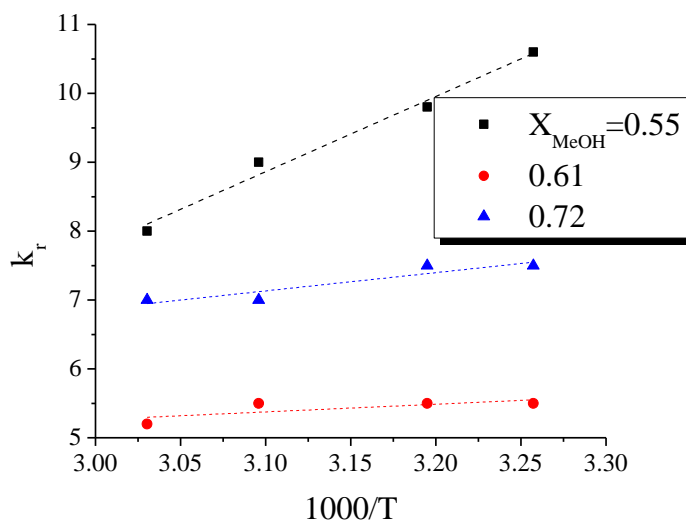


Figure 4.20. MHQ in MeOH/dioxane: recombination rate, k_r , vs. $1000/T$.

The pK_a^* values for the MeOH/dioxane system were determined to be $-2.3 < \text{pK}_a^* < -2.6$, similar to those in the gas-expanded methanol mixtures. Again, these values suggest that there is an extremely strong preferential solvation by MeOH where the values are close to those expected in pure MeOH. Thermodynamic data were obtained using the Van't Hoff relation,

$$\text{pK}_a^* = \Delta H/2.3RT - \Delta S/2.3R. \quad (\text{Eq. 4.1})$$

The values obtained from these calculations for the MeOH/dioxane system are summarized in Table 4.4.

Table 4.4. Values of enthalpy, ΔH , and entropy, ΔS , of the proton transfer reaction of MHQ in MeOH/dioxane

X_{MeOH}	ΔH (kJ/mol)	ΔS (J/mol/K)
0.55	5.2 ± 0.8	59 ± -2
0.61	-2.9 ± 0.4	38 ± 0
0.72	-1.6 ± 1.3	42 ± -4

Again, the positive entropic factor is consistent with the formation of two species, the proton and Z^* . The enthalpy factor is associated with the bonds that are involved with the proton transfer process, especially the hydrogen bond between the hydroxyl moiety and the MeOH cluster. Assuming this relation, and because the energy measured is too small for hydrogen bonds between MeOH molecules,¹⁴ the enthalpy change can be correlated to a weak hydrogen bond formed between the hydroxyl group and solvent molecules. At higher mole fractions of methanol, the positive entropic and negative enthalpic factor indicates the the reaction is exergonic at any temperature. Again, this is inconsistent with previous results and therefore these numbers must be met with caution.

In summary, the ESPT properties of MHQ in methanol/scCO₂ and in methanol/dioxane mixtures were studied. The photoprolytic dissociation rate was determined to be roughly constant, suggesting that the system is solely in the exergonic regime where extremely strong preferential solvation by methanol governs the ESPT rate.

References

1. (a) Kendall, J.L.; Canelas, D.A.; Young, J.L.; DeSimone, J.M. *Chem. Rev.* **1999**, 99, 543. (b) Leitner, W. *Acc. Chem. Res.* **2002**, 35, 746. (c) Subramaniam, B.; Rajewski, R.A.; Snavely, K. **1997**, 86, 885.
2. Nunes, R.M.D.; Arnaut, L.G.; Solntsev, K.M.; Tolbert, L.M.; Formosinho, S.J. *J. Am. Chem. Soc.* **2005**, 127, 11890.
3. Akien, G.R.; Poliakoff, M. *Green Chem.* **2009**, 11, 1083.
4. Tomasko, D.L.; Knutson, B.L.; Eckert, C.A.; Haubrich, J.E.; Tolbert, L.M. *ACS Symposium Series* **1992**, 488, 84.
5. Tomasko, D.L.; Knutson, B.L.; Pouillot, F.; Liotta, C.L.; Eckert, C.A. *J. Phys. Chem.* **1993**, 97, 11823.
6. Genosar, L.; Leiderman, P.; Koifman, N.; Huppert, D. *J. Phys. Chem. A* **2004**, 108, 309.
7. Koifman, N.; Cohen, B.; Huppert, D. *J. Phys. Chem. A* **2002**, 106, 4336.
8. (a) Papanastasiou, G.E.; Ziogas, I.I. *J. Chem. Eng. Data* **1992**, 37, 168 (b) Zhang, Y.; Yang, J.; Yu, Y.-X. *J. Phys. Chem. B* **2005**, 109, 13375.
9. Galicialuna, L.A., D. Richon, and H. Renon, *J. Chem. Eng. Data* **1994**, 39, 424.
10. Solntsev, K.M., Huppert, D., Agmon, N. *J. Phys. Chem A* **1999**, 103, 6984.
11. Dombro, R.A., McHugh, M.A.; Prentice, G.A.; Westgate, C.R. *Fluid Phase Equilibria* **1991**, 61, 227.
12. Lakowicz, J.R. *Principles of Fluorescence Spectroscopy*, 2nd ed.; Springer: New York, 2004; Chapter 6.

13. Popov, A.V., Gould, E.-A., Salvitti, M.A.; Hernandez, R.; Solntsev, K.M. *Phys. Chem. Chem. Phys.* **2011**, 13, 14914.
14. (a) Biczok, L., P. Valat, and V. Wintgens *Photochem. Photobiol. Sci.* **2003**, 2, 230. (b) Wallen, S.L; Palmer, B.J.; Garrett, B.C.; Yonker, C.R. *J. Phys. Chem.* **1996**. 100, 3959.

Part III: MHQ Photophysics in Nafion Films

Introduction

Nafion was initially developed by DuPont for the chloroalkali industry,¹ however it has become the preeminent membrane separator used in methanol fuel cells. Nafion has a high proton mobility and is chemically resistant and thermally stable up to 190°C,² which allows for its use for the relatively harsh conditions under which current fuel cells must operate. Not only is Nafion a staple in the fuel cell industry, but it is also used in electrochemical devices, metal-ion recovery, water electrolysis, plating, surface treatment of metals, batteries and sensors.³ In the protonated form, Nafion is an extremely strong acid ($\text{pK}_a \sim -6$), which makes it a good superacid catalyst for the production of fine chemicals.³ The structure of Nafion contains extremely polar and non-polar groups. It is a polymer with a polyfluorocarbon backbone (hydrophobic) and sulfonated side chains (hydrophilic). It is this intrinsic amphiphilic nature that causes the polymer to segregate into characteristic “domains”. The water in the hydrophilic domains allows for Nafion’s superb proton diffusion from the anode to the cathode of the fuel cell. The proton mobility of Nafion is known to be dependent on the nature of the hydrophilic region in the membrane.^{3b} Thus, the proton transport in Nafion is highly dependent on the water concentration in the membrane.⁴ However, the structure of the water nanopools and the proton transport through these pools are not fully elucidated.

Much information about the morphology of Nafion has been gathered over the past 30 years. However, despite the efforts of many top scientists^{3b,5} and despite the plethora of data, there is not a widely accepted morphological structure for Nafion. The

first work attempting to describe the structure of Nafion was by Gierke and Hsu.⁶ They proposed a cluster-network type model in which ionic sulfonate clusters, roughly spherical in shape, are connected by narrow water channels that allow proton diffusion from one cluster to the next. Although the model proposed by Gierke and Hsu may be an oversimplification of a very complicated morphology, it remains widely accepted due to its ability to explain a large number of Nafion's properties.^{3b}

Recently, Fayer and coworkers used dynamic fluorescent probes to explore the nanostructure of Nafion.⁷ The ESPT of 8-hydroxypyrene-1,3,6-trisulfonic acid (HPTS), 8-hydroxy-*N,N,N',N',N'',N''*-hexamethylpyrene-1,3,6,-trisulfonamide (HPTA) Rhodamine 6G (R6G) was studied in Nafion as a function of hydration level of the films.⁷ HPTS is a hydrophilic trianion which resides in the water regions of the film; HPTA is a neutral probe, which resides in the hydrophilic-hydrophobic region of the film; R6G is a cationic molecule which can be found in the water-polymer interface. The use of these three probes allowed for examination of the three distinct regions in Nafion. As expected, little ESPT is seen at low hydration levels, and as hydration level increases, ESPT increases. With increased hydration, more water is in the membrane so enough molecules can orient properly to solvate the proton.

To extend the work of Fayer and coworkers⁷ to cationic "super" photoacids, MHQ was used as a photoprobe in an attempt to comment on the nanostructure of the Nafion water pools because the dynamics of the ESPT in MHQ is so strongly affected by the ability of the proton-accepting solvent to solvate the proton. The geminate recombination reaction is also reversible, and will therefore be affected by the proton mobility of the surrounding media.

Experimental Protocols

MHQ was synthesized according to the procedure in Chapter 3. The acid form of Nafion 117, 115, 212, and 211 were purchased from Fuelcellstore.com. “117” indicates a film having 1100 equivalent weight and a thickness of 0.007 in. Films were cut to uniform size for all experiments. For the thin, laboratory prepared films, Nafion was purchased from Clean Fuel Cells, Inc., as a 5 wt% solution. The solution of Nafion was spin coated onto quartz slides and dried over-night in a vacuum oven at room temperature. MHQ was incorporated into the membrane by soaking Nafion in a solution of MHQ of the desired concentration for ~ 24 h at room temperature. After the MHQ was incorporated into the membrane, the films were rinsed first with deionized water, allowed to soak in deionized water for ~ 1 h, and rinsed for a second time to ensure that the photoacid was actually incorporated into the membrane and not just adhered to the surface.

Uv-vis absorption spectra were taken on a Perkin Elmer Lambda 19 and fluorescence measurements were acquired using a Horiba Jobin Yvon Fluorolog 2 Spectrophotometer. Fluorescence spectra were collected at a right angle from the excitation source. The excitation source was a 1000 W high-pressure Hg-Xe lamp. Entrance and exit slits were set to 1.5 mm. Measurements were taken at three different humidity levels: “in solution”, “wet”, and “dry”. “In solution” refers to spectra that were collected as the film sat in a quartz cuvette filled with deionized water. “Wet” films were removed from deionized water and allowed to sit at ambient conditions for ~ 1 h before spectral data collection. “Dry” films were either dried over nitrogen for ~ 15 min or dried

overnight in an oven at 130°C. In the latter cases, both methods yielded identical results. The emission spectra of the “wet” and “dry” films were collected on a solid sample holder. Fluorescence emission spectra were acquired with the excitation set at the maximum absorption wavelength.

Results

MHQ was readily absorbed into Nafion 117 and 115 as can be seen by the absorption spectra of the water solutions used for soaking in Figure 4.21. For Nafion 117 and 115, the characteristic absorption peak of MHQ (black curve) at 360 nm disappears and the solution shows no absorption in the UV-vis range after 24 hours of soaking the films. In contrast to Nafion 117 and 115, the 212 and 211 films do not show any appreciable uptake of MHQ. The MHQ-water solution has the same concentration of MHQ after a 24 hour soak, while the absorption maximum blue-shifted to indicate formation of the ground-state zwitterionic species (green and pink curves).

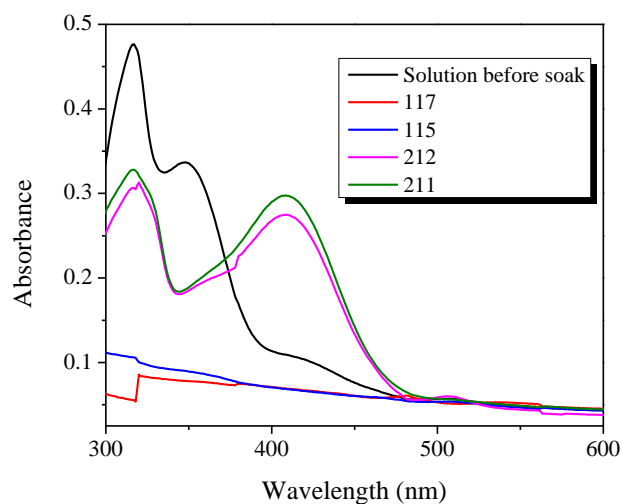


Figure 4.21. MHQ in Nafion: water solutions before/after 24 hr soak.

Figure 4.22 shows the emission spectra of MHQ in Nafion 117 and 115. ESPT is observed in films dipped in a solution of water as indicated by the dual emission in the top spectrum of Figure 4.22. However, upon removal from the water, ESPT disappears and only a single emission from the excited-state cation is observed (Figure 4.22, middle spectrum). As expected, upon drying the films, ESPT is still not observed, however, the

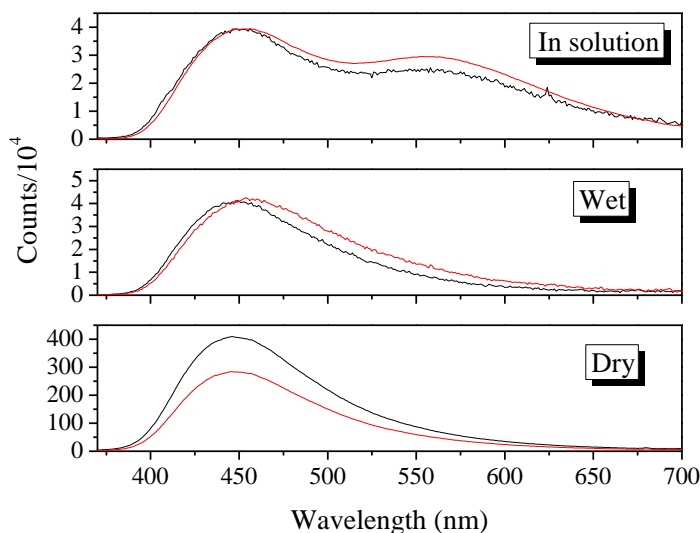


Figure 4.22. Steady-state emission of MHQ in Nafion 117 (black) 115 (red)

fluorescence intensity of the MHQ C* signal is increased by over two orders of magnitude (Figure 4.22, bottom spectrum). Little difference is seen in all spectra for Nafion 117 versus 115.

The same set of experiments was performed in laboratory-prepared 320 nm films. While some MHQ was incorporated into the 320 nm films, only a single emission was observed under all conditions, indicating that no ESPT was present regardless of the water environment.

The TCSPC decays of wet and dry MHQ in Nafion 117 and 115 are shown in Figure 4.23. The decays are independent of film thickness, although shorter lifetimes are observed for wet films.

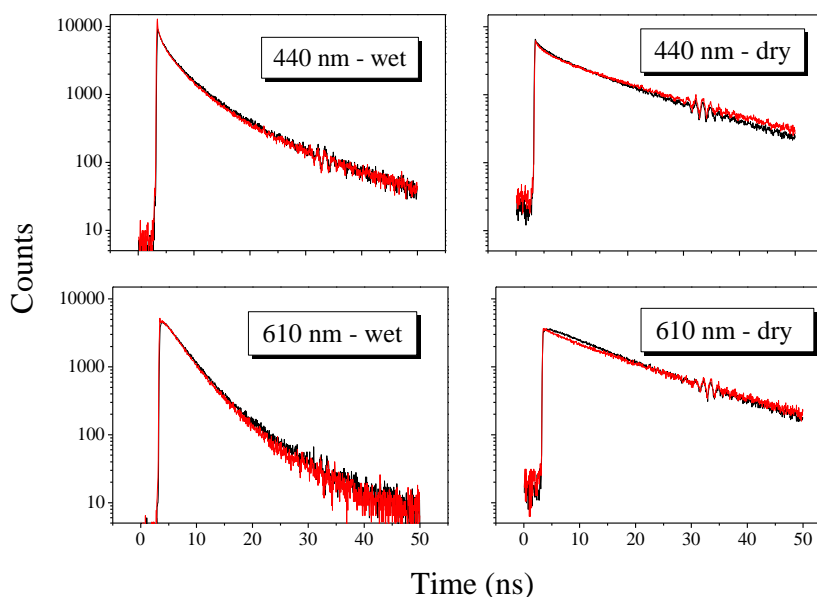


Figure 4.23. MHQ in Nafion: TCSPC decays of C* (440 nm) and Z* (610 nm).

Discussion and Conclusions

The absorption spectra shown in Figure 4.21 indicate that MHQ can be readily absorbed by certain Nafion films, however the film preparation and morphology influences dye uptake. MHQ is readily absorbed by 183 and 127 μm (Nafion 117 and 115, respectively) extrusion-cast commercially available films, while 50.8 and 25.4 μm (Nafion 212 and 211, respectively) dispersion-cast commercially prepared films do not absorb dye in measureable concentrations. In contrast, lab-prepared spin-cast very thin films, approximately 320 nm thick, do absorb MHQ, however the concentrations are

much lower (Table 4.3). Film preparation has been shown to influence Nafion morphology through the conformations of Nafion molecules in solution that lead to variable aggregation patterns in the resulting films.⁸

From the steady-state emission spectra (Figure 4.22), it can be concluded that ESPT increases as hydration level in Nafion 117 and 115 increases. This phenomenon is well-documented throughout the literature.⁷ With increased hydration, more water is in the membrane so enough molecules can orient properly to solvate the proton. The observation from the steady-state emission spectra of MHQ in Nafion that ESPT only occurs in films in solution demonstrates that Nafion must have very high water content in order to support proton dissociation.

The average lifetimes of MHQ in Nafion 117 and 115 are independent of film thickness (Table 4.5). The lifetimes decrease in the presence of water. This is not unexpected due to the known preferential solvation of MHQ by water (Chapter 3). Confirming the lack of ESPT observed from the steady-state spectra, the lifetimes do not change appreciably from monitoring the C* and Z* decays, indicating lack of the photoprotolytic process.

Table 4.5. Average lifetimes of MHQ in Nafion

Film Thickness (micron)	τ_{avg} (ns) 445, 610 nm
183(wet)	3.1, 4.1
127(wet)	4.1, 3.8
183(dry)	8.0, 9.7
127(dry)	8.0, 9.7

For thinner, laboratory prepared films, no proton transfer was seen even in very swollen films. This indicates that the water nanopools are not available to accept a proton. Even though the very thin films are in bulk water, the water channels are so few or so small that they are not available to accept a proton. This could be due to all the water solvating the sulfonic acid groups.⁷

Although proton transfer is seen in thicker, water-rich films, the overall fluorescence of the system is heavily quenched. Upon drying the films, the overall emission increases by more than two orders of magnitude as shown in Figure 4.24.

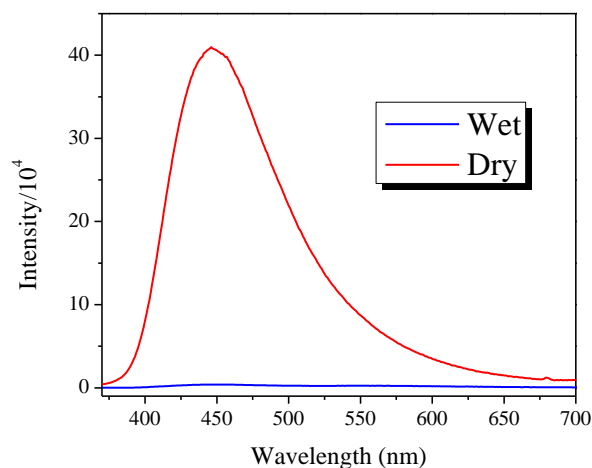


Figure 4.24. Fluorescence quenching in Nafion: dry (red) vs. wet (blue) films.

Unfortunately, this indicates that MHQ is an ineffective ESPT probe in these systems because the proton acceptor (water) heavily quenches MHQ fluorescence. The quenching of MHQ by various solvents will be discussed in detail in Chapter 5.

References

1. Hora, C. J.; Maloney, D. E. *J. Electrochem. Soc.* **1977**, 124, C319
2. Hofmann, D.W.M.; Kuleshova, L.; D'Aguanno, B.; Di Noto, V.; Negro, E.; Conti, F.; Vittadello, M. *J. Phys. Chem. B* **2009**, 113, 632-639.
3. (a) Larminie, J.; Dicks, A. *Fuel Cell Systems Explained*; J. Wiley and Sons: Chichester, **2000**. (b) Mauritz, K. A.; Moore, R. B. *Chem. Rev.* **2004**, 104, 4535-.
4. (a) Anantaraman, A. V.; Gardner, C. L. *J. Electroanal. Chem.* **1996**, 414, 115. (b) Zawodzinski, J. T. A.; Derouin, C.; Radzinski, S.; Sherman, R. J.; Smith, T. V.; Springer, T. E.; Gottesfeld, S. *J. Electrochem. Soc.* **1993**, 140, 1041.
5. (a) Roche, E. J.; Pineri, M.; Duplessix, R. *J. Polym. Sci., Polym. Phys.* **1982**, 20, 107. (b) Yeager, H. L.; Steck, A. *J. Electrochem. Soc.* **1981**, 128, 1880. (c) Cappadonia, M.; Erning, J. W.; Stimming, U. *J. Electrochem. Soc.* **1994**, 376, 189. (d) Litt, M. H. *Polym. Prepr.* **1997**, 38, 80. (e) Rieberer, S.; Norian, K. H. *Ultramicroscopy* **1992**, 41, 225. (f) Ceynowa, J. *Polymer* **1978**, 19, 73. (g) Xue, T.; Trent, J. S.; Osseo-Asare, K. *J. Membr. Sci.* **1989**, 45, 261.
6. (a) Hsu, W. Y.; Gierke, T. D. *Macromolecules* **1982**, 15, 101. (b) Gierke, T. D.; Munn, G. E.; Wilson, F. C. *J. Polym. Sci., Polym. Phys.* **1981**, 19, 1687.
7. 40, 41 OP Spry, D.B.; Fayer, M.D. *J. Phys. Chem. B* **2009**, 113, 10210-10221

8. Lin, H.-L.; Yu, T.L.; Huang, C.-H.; Lin, T.-L. *J. Poly. Sci. B.* **2005**, 43, 3044.

CHAPTER 5

FLUORESCENCE QUENCHING OF QUINOLINIUM SALTS:

SOLVENT EFFECTS

Introduction

Fluorescence quenching is the depopulation of the excited state via non-radiative pathways. These pathways can occur within the excited-state lifetime or can occur due to formation of complexes in the ground state. The processes are divided into two types of quenching: static vs. dynamic (collisional) and are known to follow Stern-Volmer kinetics:

$$I_0/I = \tau_0/\tau = 1 + k_q \tau_0[Q] = 1 + K_{SV}[Q]$$

Where I_0 , τ_0 and I , τ are the fluorescence intensities and the lifetimes of the fluorophore in the absence and presence of the quencher, respectively, $[Q]$ is the concentration of the quencher, k_q is the bimolecular quenching rate constant and K_{SV} is the Stern-Volmer quenching constant. A Stern-Volmer plot (I_0/I vs. $[Q]$) in the simplest case will produce a straight line with the slope K_{SV} . In the case of static quenching, K_{SV} is the equilibrium constant for formation of the ground-state complex. If both dynamic and static quenching are involved, the Stern-Volmer equation is second order.

The fluorescence quenching of aromatic compounds has been extensively studied.¹ Weber studied the quenching of several neutral fluorophores by iodide and other aromatic molecules.² The quenching of quinolinium salts by anions and solvents has been previously reported.³ The quenching mechanism is generally explained by electron

transfer from the electron-rich anions to the quinolinium cations. Specifically, the *N*-sulfonatopropyl-6-methoxy-quinolinium salt is known for its use as a chloride indicator.⁴ Quinolinium and isoquinolinium perchlorates were shown to undergo electron-transfer induced fluorescence quenching by electron-rich olefins at rates near to the diffusion-controlled limit.⁵ 5-(4-*R*-phenyl)-7,7-dimethyl-7H-indolo[1,2-*a*]quinolinium perchlorate was shown to undergo quenching by various organic solvents via complex formation between the solvents and the fluorophores.^{3d} The complex stability was similar to that of strong hydrogen bonds.

MHQ was synthesized with non-nucleophilic counteranions, such as perfluoroalkanesulfonates, to overcome both solubility issues and quenching by the counteranion. As discussed previously, MHQ-nonaflate (MHQ-Nf) exhibits strong emission and the highest excited-state photoacidity measured thus far (See Chapter 3). A high fluorescence quantum yield and efficient ESPT has been obtained for these salts in non-nucleophilic solvents. While there have been studies done on anion quenching, there have not been studies done on the quenching of quinoliniums by a wide variety of solvents, and there has been little discussion of the photophysics of this process. Therefore, after the observation that MHQ undergoes significant fluorescence quenching by hydroxylic solvents (Chapter 4, Section III), we sought to explore fluorescence quenching of a variety of quinolinium salts in a wide array of solvents to more clearly identify the molecular basis for such quenching.

Experimental Protocols

All quinolinium salts, with the exception of *N*-methyl-6-cyano-quinolinium (6CNMQ), were synthesized according to the procedure outlined in Chapter 3 beginning with the appropriate quinoline.

Synthesis of 6CNMQ. *Synthesis of 6-tosylquinoline.* 6-Hydroxyquinoline (98%) was purchased from Acros and used without further purification. 4-Toluenesulfonyl chloride (99%) was purchased from Aldrich and used without further purification. A 1.3 molar equivalent of 4-toluenesulfonyl chloride (1.7 g, 9.0 mmol) was added to 6HQ (1.1 g, 7.5 mmol) in pyridine and heated at 50°C for 6 hours. The solution was added to NH₄Cl and H₂O to quench the reaction and remove pyridine from the crystals. The crystals were filtered and washed several times with water.

Synthesis of N-methyl-6-cyanoquinoline. A phosphine catalyst was prepared by stirring Pd(OAc)₂ (6.2, 0.028 mmol), 2-[2-(dicyclohexylphosphino)phenyl]-1-methyl-1H-indole (34.6 mg, 0.086 mmol), dichloromethane and triethylamine under nitrogen flow for 30 minutes. Upon removal of solvent, 6-tosylquinoline (451 mg, 1.5 mmol), potassium hexacyanoferrate(II) trihydrate, and potassium carbonate were added to the phosphine catalyst in a 1:1 solution of water and 2-methyl-2-propanol under nitrogen flow and stirred for 24 hours. The crude product cooled to room temperature before adding EtOAc and water. The organic layer was extracted and dried with anhydrous magnesium sulfate. The product was then filtered using a carbon decolorizing agent and washed with EtOAc. The resulting cyanoquinoline was methylated according to the procedure described in Chapter 3 using methyl nonaflate.

Optical spectra were acquired using the same instrumentation described in Chapter 3.

Stock solutions were prepared so that the optical density of the quinolinium salt was $OD = 0.5$ ($\sim 10^{-5}$ M) in acetonitrile. Microliter aliquots of the desired quencher were added to 3 mL of stock solution, measured with a 3mL volumetric flask, in a quartz cuvette, such that the total volume of added quencher never exceeded 2% of the total volume. Measurements were taken after each addition of quencher. All solvents (quenchers) were anhydrous spectral grade and were used as purchased without further purification.

Results

In order to clarify the role of steric hindrance, as well as electronic effects, several *N*-methylquinolinium salts were synthesized for study. These included compounds with methyl, methoxy, and cyano substituents, as well as the photoacid MHQ and the parent *N*-methylquinolinium (MQ). In this section, the quinoliniums studied were divided into three categories: compounds with no substituents or with methylated substituents, compounds with strongly electron donating substituents, and one compound with a strongly electron withdrawing substituent. The structures of all compounds studied are shown in Table 5.1.

Table 5.1. Structures of quinolinium salts studied.

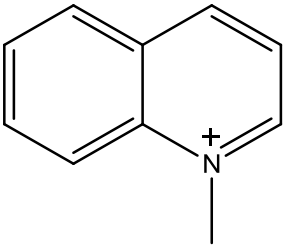
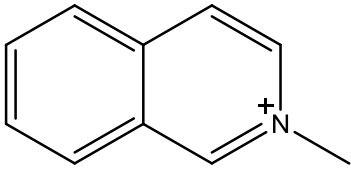
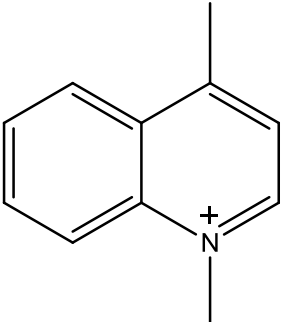
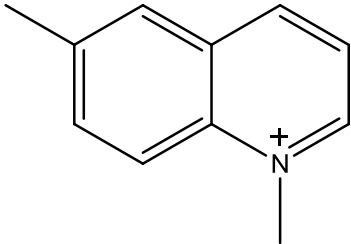
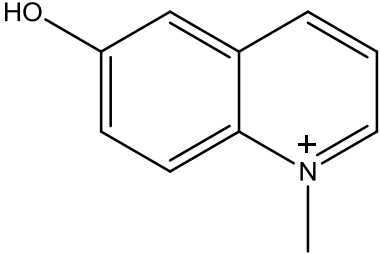
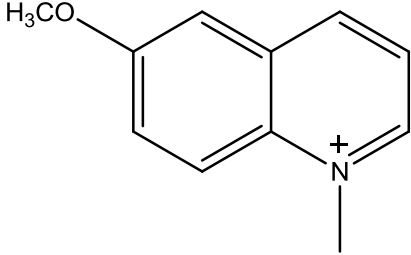
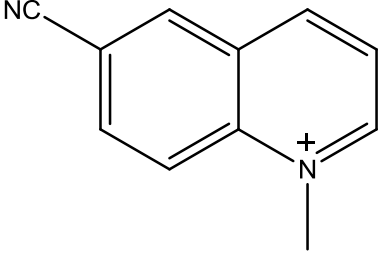
<p>MQ</p> 	<p>isoMQ</p> 
<p>4MMQ</p> 	<p>6MMQ</p> 
<p>MHQ</p> 	<p>MMQ</p> 
<p>6CNMQ</p> 	

Figure 5.1 shows the Stern-Volmer quenching plots of MQ, isoMQ (top panel) and 4MMQ, 6MMQ (bottom panel) nonaflate salts by various ethers. For these quinoliniums containing only methyl substituents, either solely on the nitrogen (MQ, isoMQ) or on the nitrogen and the 4- or 6-position (4MMQ and 6MMQ, respectively), dioxane quenches the emission most efficiently. With the exception of isoMQ, 2-methyl-

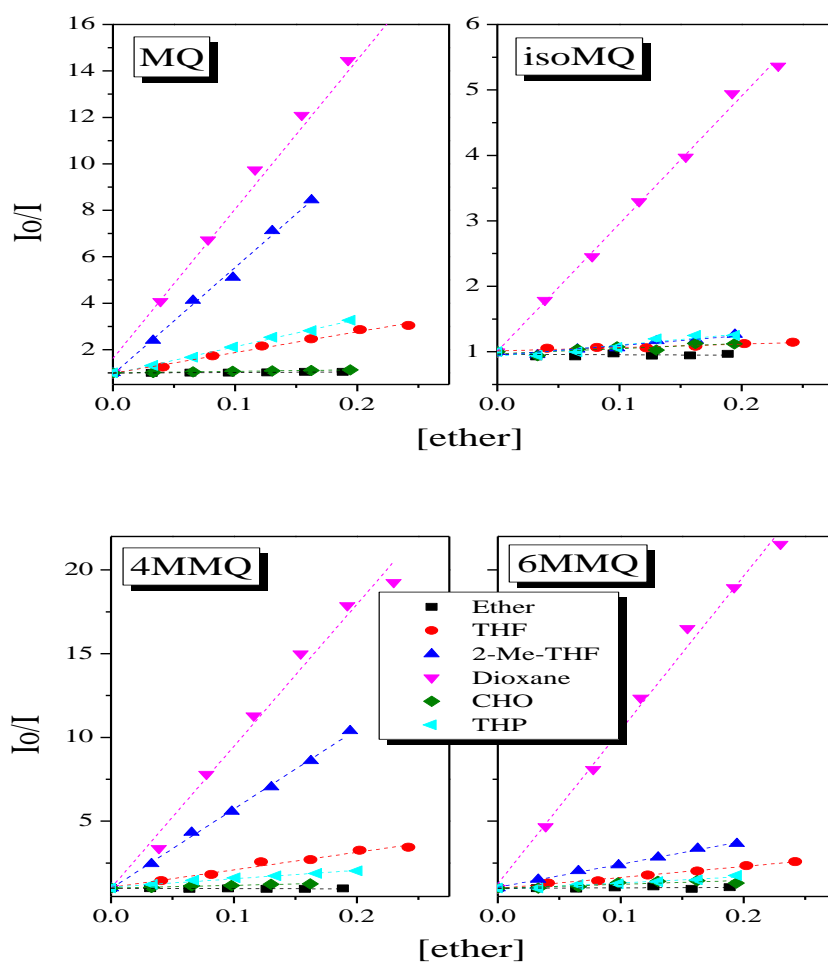


Figure 5.1. Fluorescence quenching of MQ, isoMQ (top panel) and 4MMQ, 6MMQ (bottom panel) by ethers

THF is the next most efficient quencher of the compounds. THF and THP both induce some quenching in the quinoliniums; however, their efficiency is lower than that of dioxane and THP. Ether and CHO do not quench the emission of 4MMQ, 6MMQ, MQ and isoMQ within experimental error. The overall fluorescence is quenched by approximately the same amount for MQ, 4MMQ, and 6MMQ, while isoMQ shows a diminished quenching (note y-axis scale).

Figure 5.2 shows the quenching of quinolinium nonaflate salts with strongly electron donating groups at the 6-position, i.e., MHQ (6-OH) and MMQ (6-OMe). Unlike the compounds described above, MHQ and MMQ show the most decrease in fluorescence in the presence of THP. Further, the overall fluorescence is quenched by approximately an order of magnitude less than the methylated compounds, with the exception of isoMQ, where the fluorescence of MHQ and MMQ are quenched ~ 4 times less. Other than THP, the emission by MMQ is relatively unaffected by ethers. MMQ does show a slight fluorescence enhancement with THF and dioxane, but it is very small and could be a result of experimental error.

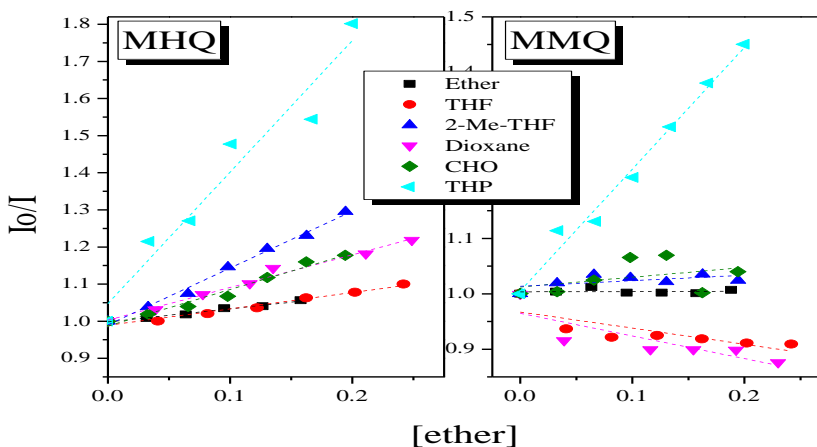


Figure 5.2 Fluorescence quenching of MHQ and MMQ by ethers

The quenching by ethers of the quinolinium with a strong electron withdrawing group in the 6-position is shown in Figure 5.3. 6CNMQ is quenched by all ethers, with the largest quenching constants of all the quinoliniums studied. In accordance with the first set of compounds mentioned, 6CNMQ is quenched most heavily by dioxane and least by CHO and ether. Of interest is the noted plateau in emission intensity in the presence of THF, 2-methyl-THF, and THP.

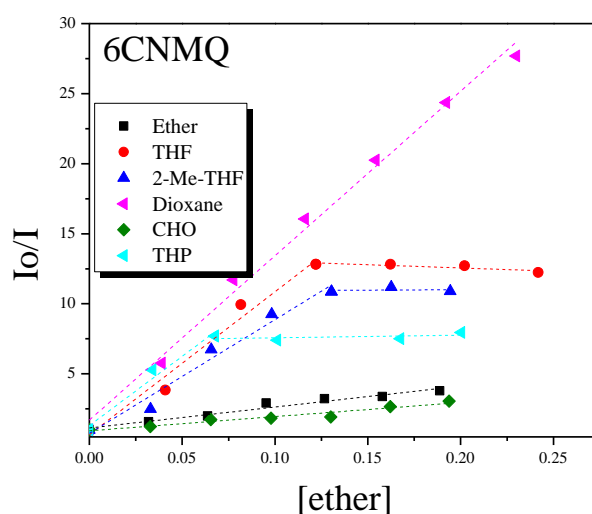


Figure 5.3 Fluorescence quenching of 6CNMQ by ethers

Fluorescence quenching of quinolinium salts by hydroxylic solvents

Figure 5.4 shows the Stern-Volmer quenching plots of MQ, isoMQ (top panel) and 4MMQ, 6MMQ (bottom panel). In this case, these compounds do not show any appreciable quenching by hydroxylic solvents.

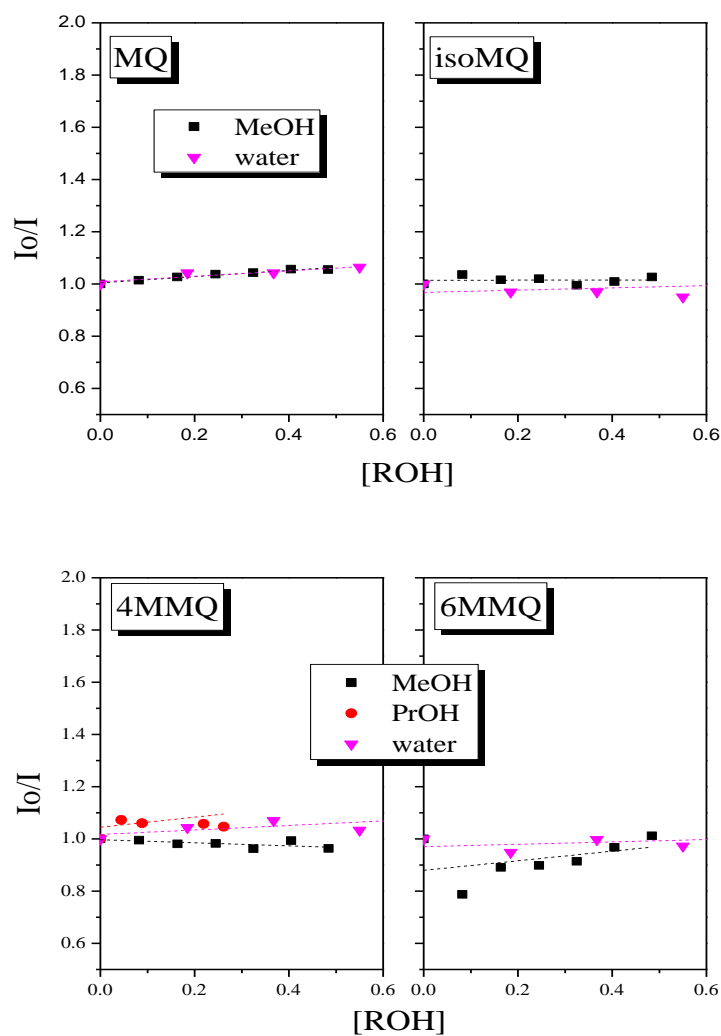


Figure 5.4 Fluorescence quenching of MQ, isoMQ (top panel) and 4MMQ, 6MMQ (bottom panel) by hydroxylic solvents

The quenching of MHQ and MMQ is shown in Figure 5.5. The emission of MMQ is not affected by the presence of hydroxylic solvents. In contrast, MHQ, which can undergo ESPT, shows significant quenching by the same alcohols. The salt is quenched by alcohols with relatively the same efficiency for MeOH, PrOH, and BuOH. As noted in previous experiments (Chapter 4, Part III), MHQ is also heavily quenched by water.

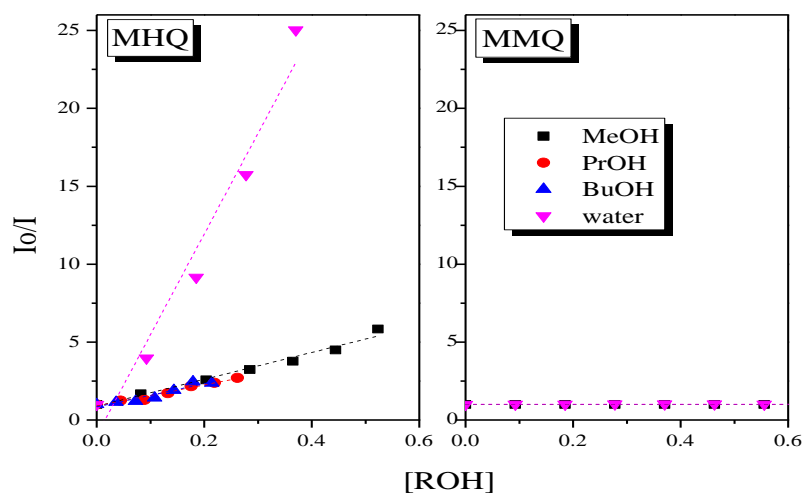


Figure 5.5 Fluorescence quenching of MHQ (left) and MMQ (right) by hydroxylic solvents.

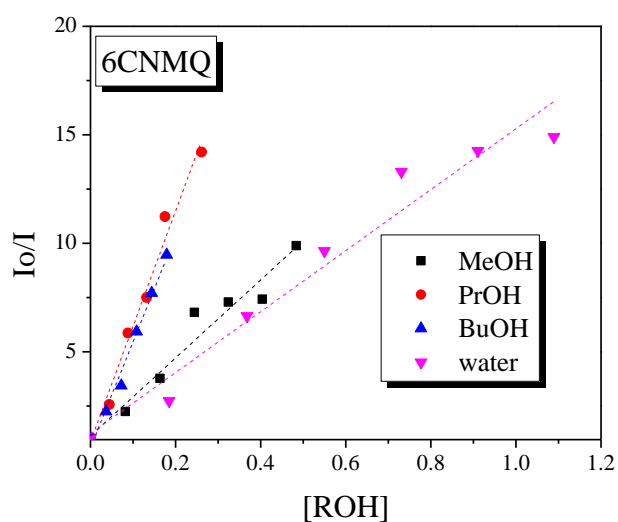


Figure 5.6 Fluorescence quenching of 6CNMQ by hydroxylic solvents.

The quenching effect of the strong EWG cyano in the 6-position of the quinolinium is shown in Figure 5.6. Like MHQ, 6CNMQ is quenched by all hydroxylic solvents studied. However, the overall quenching is greater in the presence of alcohols for 6CNMQ than for MHQ, while for water the efficiency is relatively the same.

Fluorescence quenching of quinolinium salts by nucleophilic solvents

The final set of solvents studied will be referred to as “nucleophilic” quenchers: DMSO, DMF, DMS and acetone. Figure 5.7 shows the Stern-Volmer plots of MQ,

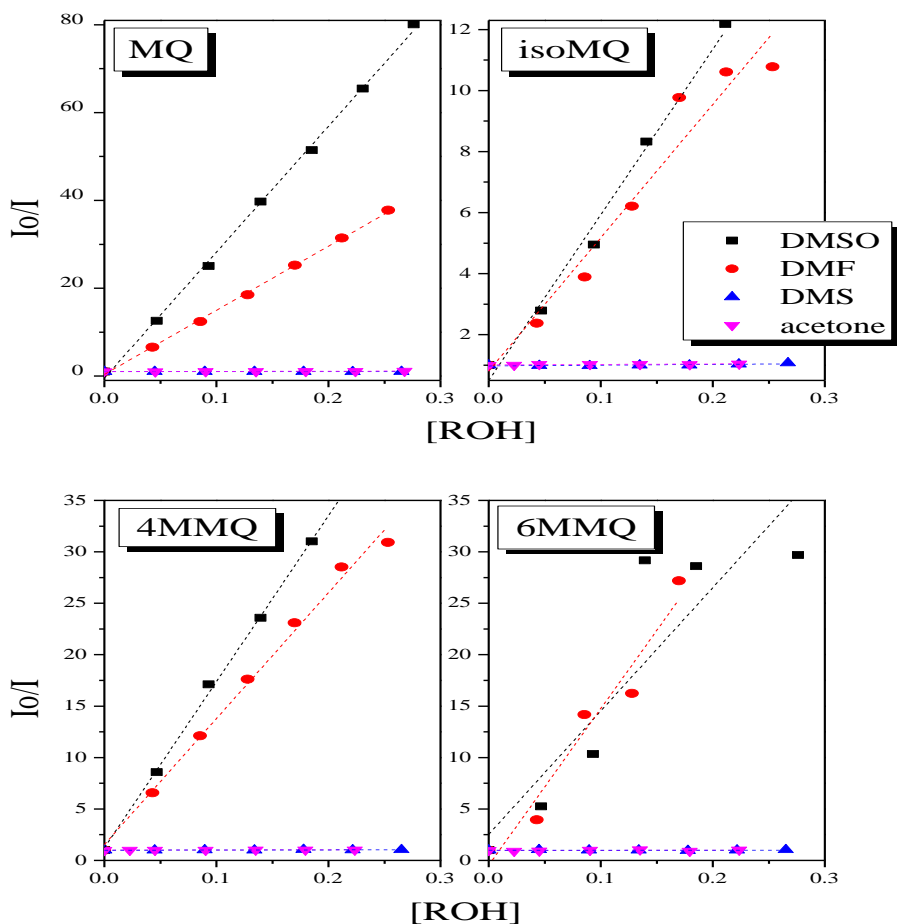


Figure 5.7. Fluorescence quenching of MQ, isoMQ (top panel) and 4MMQ, 6MMQ (bottom panel) by “nucleophilic” solvents.

isoMQ (top panel) and 4MMQ, 6MMQ (bottom panel) quenched by various nucleophilic solvents. The emission of these four compounds decreases in the presence of DMSO and DMF, but not in the presence of DMS and acetone. In general, the quenching is most efficient in DMSO, where the effect is most pronounced for MQ. The MQ emission is diminished by ~ 2 times more than for 4MMQ and 6MMQ and by ~ 6 times more than for isoMQ.

The analogous plots for MHQ and MMQ are shown in Figure 5.8. Like the compounds above, DMS and acetone do not induce any appreciable quenching for MHQ and MMQ. Interestingly, MMQ is quenched relatively efficiently by DMSO. This is the only quencher studied in which MMQ shows appreciable quenching. As is the case in hydroxylic solvents, ESPT can occur to DMSO and DMF, where we see MHQ emission quenching by these solvents.

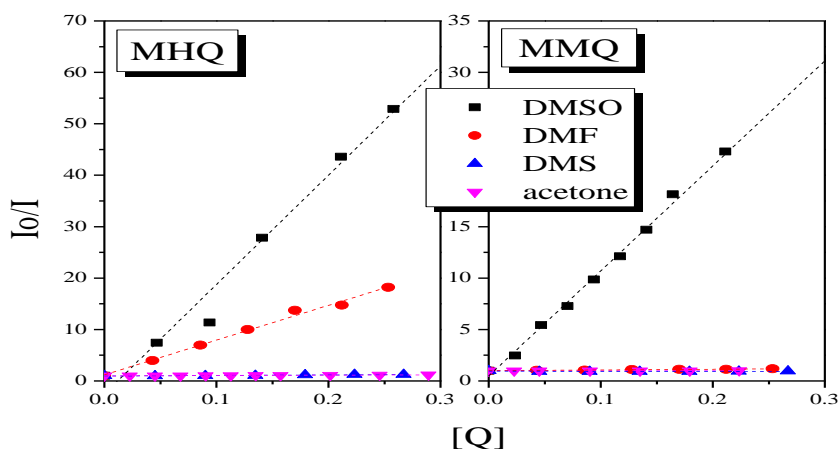


Figure 5.8. Fluorescence quenching of MHQ and MMQ by nucleophilic solvents.

The quenching by nucleophilic solvents for 6CNMQ is shown in Figure 5.9. Again, DMSO and DMF induce appreciable fluorescence quenching. In the presence of DMS, the emission is not diminished, while in acetone some quenching is observed.

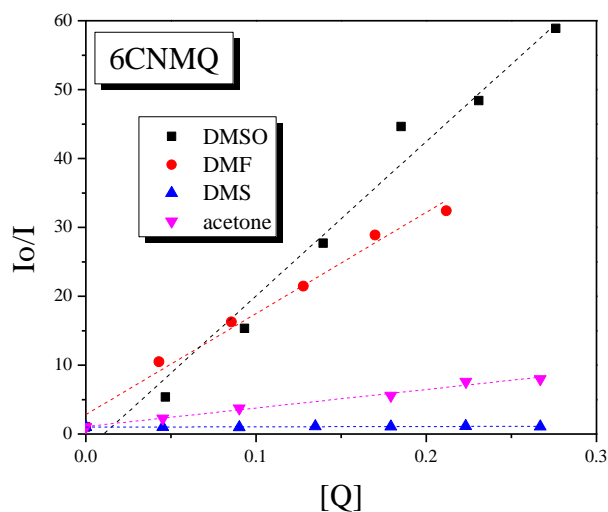


Figure 5.9. Fluorescence quenching of 6CNMQ by nucleophilic solvents.

Fluorescence quenching of MHQ by DMSO and water

Figure 5.10 shows the Stern-Volmer plot of MHQ by water and DMSO. DMSO quenches MHQ more than twice as efficiently as water, with $K_{SV} = 203$ and 90, respectively.

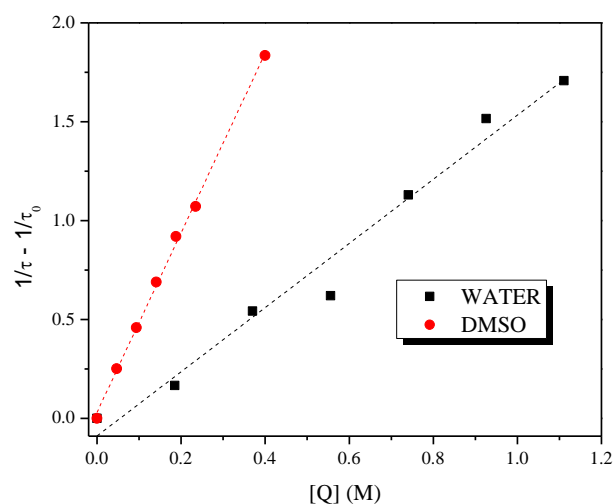


Figure 5.10. Fluorescence quenching ($1/\tau - 1/\tau_0$ vs. $[Q]$) of MHQ in water (black) and DMSO (red).

Figures 5.11 and 5.12 show the kinetic decay curves of the C* and Z* species, respectively, in DMSO and water. A long-lifetime tail appears in just 0.36 M water, where its amplitude remains relatively constant upon addition of increasing amounts of water. As discussed previously (Chapter 3), this long-lifetime tail does not appear upon addition of DMSO.

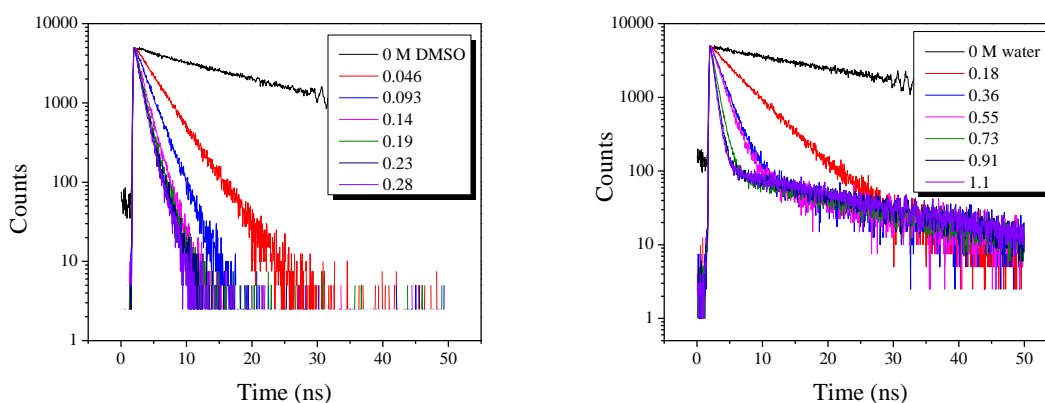


Figure 5.11. MHQ-Nf decays at 440 nm in MeCN/DMSO (left) and MeCN/water (right).

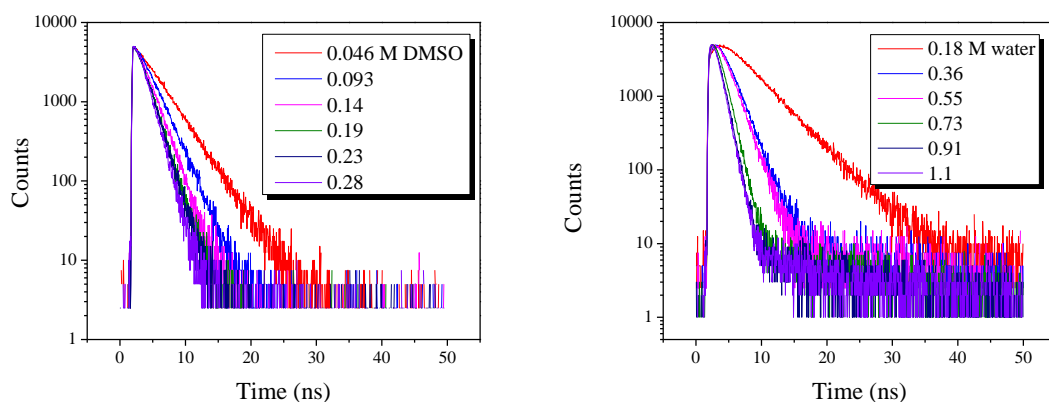


Figure 5.12. MHQ-Nf decays at 610 nm in MeCN/DMSO (left) and MeCN/water (right).

The lifetimes of MHQ in acetonitrile versus the concentration of the quenchers DMSO and water are shown in Figure 5.13. The lifetimes in pure MeCN are ≈ 20 ns, where the lifetimes in the presence of both quenchers decrease with increasing concentration of quencher. Upon increasing addition of both quenchers, the differences in the C^* and Z^* lifetimes increase. However, the C^* and Z^* lifetimes in water are much closer to each other than in DMSO.

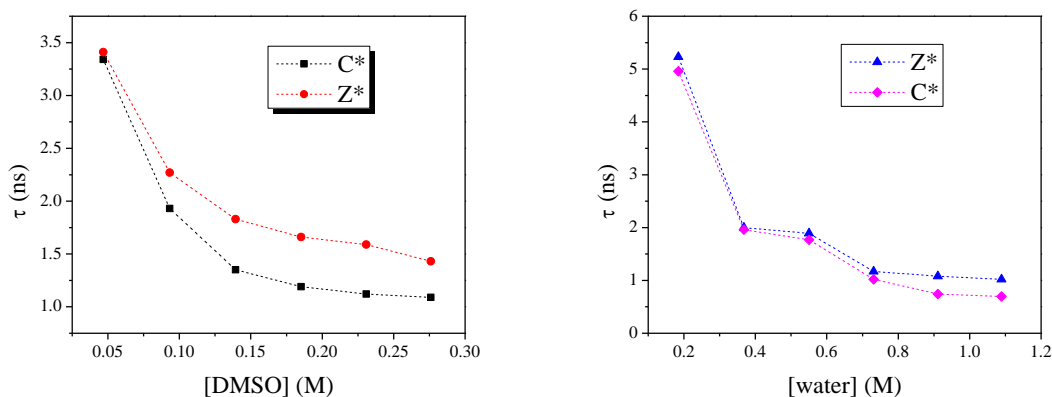


Figure 5.13. Lifetimes of MHQ-Nf in DMSO (left) and water (right) versus $[Q]$.

Table 5.2 Lifetimes in the absence of quencher (τ_0) and Stern-Volmer quenching constants, k_{SV} , for all systems studied where $k_{SV} = \tau_0 k_q$

Quinolinium (τ_0 , ns)	MQ (14)	isoMQ (7.5)	4MMQ (21)	6MMQ (23)	MHQ (21)	MMQ (23)	6CNMQ (11.3)
Ethers							
Diethyl Ether	0.31 ± 0.0 4	-0.07 ± 0.17	-0.08 ± 0.08	0.23 ± 0.31	0.35 ± 0.02	0.00	15.0 \pm 1.3
THF	8.92 ± 0.3 9	0.52 ± 0.07	10.49 ± 0.65	6.57 ± 0.23	0.49 ± 0.02	-0.29 ± 0.01	102 \pm 11
2-Me-THF	39.5 ± 4.0	1.49 ± 0.23	47.5 ± 0.9	13.8 ± 0.4	1.53 ± 0.06	0.10 ± 0.06	69.1 ± 8.6
Dioxane	64.3 ± 3.5	19.5 ± 0.5	84.8 ± 4.3	91.9 ± 3.3	0.90 ± 0.05	0.002 ± 0.000	117 ± 4
CHO	0.67	0.79	1.6	2.3	1.06	0.00	10.1

	±0.0 3	±0.23	±0.1	±0.6	±0.08		±1.1
THP	11.7 ±0.3	1.7 ±0.3	5.01 ±0.27	3.7 ±0.4	3.5 ±0.4	2.2 ±0.1	22.9 ±10.7
Hydroxylic							
MeOH	0.12 ±.01	0.00 ±0.03	-0.06 ±0.03	0.18 ±0.18	7.61 ±0.13	0.001 ±0.001	18.0 ±1.8
PrOH	1.24 ±0.1 7	--	0.19 ±0.28	--	7.10 ±0.58	--	50.4 ±3.9
Water	0.06 ±0.0 0	0.04 ±0.03	0.087 ±0.030	0.045 ±0.025	89.4 ±3.2	-0.001 ±0.007 4	14.1 ±1.3
Nucleophilic							
DMSO	302	54.2	162	120	203	102	224

	±5	±3.1	±16	±29	±4	±2	±14
DMF	146	43.7	130	152	67.5	0.67	147
	±2	±4.2	±17	±17	±2.6	±0.053	± 8.7
DMS	-	0.25	0.13	-0.01	1.05	0.013	1.45
	0.07	±0.09	±0.08	±0.12	±0.16	±0.004	± 0.22
	8						
	±0.0						
	42						
Acetone	0.48	0.15	0.16	0.18	0.72	0.0001	26.9
	±0.0	±0.05	±0.09	±0.27	±0.03	±0.000	±1.5
	2					1	

Discussion and Conclusions

The quenching of quinolinium fluorescence, particularly by counteranions, has been the subject of numerous studies.^{3,4} In most of these studies, the primary correlation has been with the difference in redox potentials between the excited quinolinium and anion. That is, the quenching mechanism is the result of electron transfer from the donor anion to the excited quinolinium. The appropriate potentials can be estimated by a consideration of the ground-state polarographic redox potentials and the $E_{0,0}$ energies of the excited molecule through the well-known Weller equation,

$$\Delta G = E_{\text{ox}} - E_{\text{red}} - E_{0,0} + C \quad (\text{Eq. 5.1})$$

where E_{ox} is the oxidation potential of the donor (anion), E_{red} is the reduction potential of the acceptor (quinolinium), $E_{0,0}$ is the singlet excitation energy of the fluorophore, and C is the coulombic energy upon charge transfer as defined by,

$$C = - e_0^2 / 4\pi\epsilon_0\epsilon a \quad (\text{Eq. 5.2})$$

where ϵ_0 is the permittivity of free space, ϵ is the solvent dielectric constant, and a is the distance between the donor and acceptor. Although we do not have the polarographic potentials of 6CNMQ and 6MMQ, the efficient quenching of 6CNMQ and the inefficient quenching of 6MMQ would seem to fit this pattern. Nevertheless, the quenching by poor electron donors such as ethers and alcohols, not to mention water, is problematic. These are very difficult to oxidize, and electron transfer from water or ethers, even to the quinolinium excited state, appears unrealistic. Moreover, the quenching rate constants are only poorly correlated with ionization potentials of the solvents.

The quenching of all of the methylquinolinium salts by simple aliphatic ethers is particularly curious. The lifetimes in the absence of quencher, τ_0 , and quenching rate constants, k_q , are shown for MQ, isoMQ, 4MMQ and 6MMQ in Table 5.1. Again, although quenching of such high-potential salts by electron transfer is conceivable, despite the high oxidation potentials of simple ethers, the correlation with ionization potential is not straightforward. Of interest was the observation that dioxane quenched all of the salts most efficiently. Since dioxane, with one oxygen providing anchimeric assistance to the other, is fairly nucleophilic, this led us to consider whether solvent nucleophilicity is driving the quenching reaction. Further, literature precedence suggests that nucleophilic anions also quench the fluorescence of MQ.^{3f}

Table 5.3 Lifetimes in MeCN and quenching constants in ethers of MQ, isoMQ, 4MMQ and 6MMQ in ethers.

Compound	τ_0 (ns)	Ether	THF	2-Me-THF	Dioxane	CHO	THP
MQ	14	4.37	126	557	907	31.4	165
isoMQ	7.5	-0.51	3.90	11.2	147	5.93	12.8
4MMQ	21	-1.71	218	988	1760	33.3	104
6MMQ	23	5.13	152	319	2120	53.1	85.5

Unfortunately, nucleophilicity data for ethers is very elusive. Although there are a number of measures of nucleophilicity, particularly of inorganic ions, there are no tables of nucleophilicity for simple ethers. We must, therefore, seek other experimental measures of nucleophilicity that would be appropriate for attack of a weak nucleophile on an electron deficient species.

There exists one report on the reaction of simple ethers with the benzyl cation generated by pulse radiolysis, which can provide insight into this effect.⁶ For the purposes of the discussion, we consider the natural log of the rate of reaction k_{nuc} of benzyl cation with ethers from the pulse radiolysis data as one variable and the log of the quenching rate constant as the other. Figure 5.14 is a plot of $\ln(k_q)$ of the MQs as a function of the nucleophilicity parameter $\ln(k_{\text{nuc}})$. The plot is highly linear, with the rate of quenching increasing with increasing nucleophilicity of the quencher, indicating a clear relationship between quenching by the ethers and nucleophilic attack of benzyl cation. In fact, the only ether deviating from the plot is tetrahydropyran (THP), which

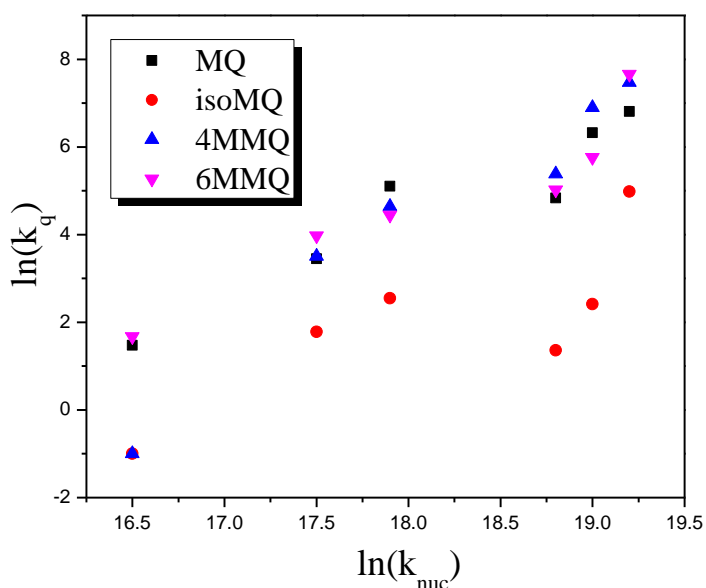


Figure 5.14. Fluorescence quenching of various quinoliniums as a function of quencher nucleophilicity. $\ln k_q$ vs $\ln k_{\text{nuc}}$ (*note value for dioxane interpolated from Ref 6.).

suggests that the error may be not in our measurements, but in the measured rate of benzyl cation reaction itself. IsoMQ deviates slightly from linearity, which is not

completely unexpected as the dipole moment for isoMQ is much different than that of the other compounds due to the position of the N-methyl group. The change in dipole moment may also explain why the emission of isoMQ is less quenched than the emission of MQ, 4MMQ and 6MMQ.

The mechanism of quenching by nucleophiles presents a challenging question. Certainly the reaction of ethers with benzyl cation has a large component of charge transfer within the transition state, and we cannot exclude such a component from the

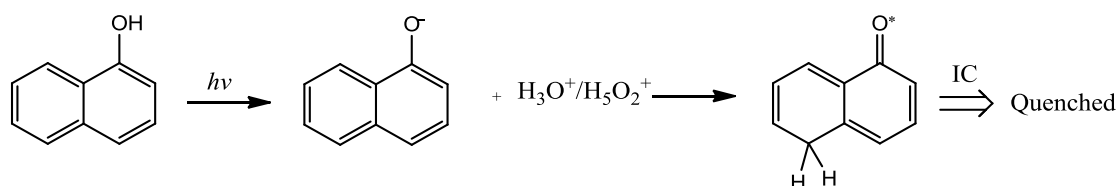


Figure 5.15. 1-naphthol quenching by photoprotonation

mechanism. We also note that quenching of the 1-naphtholate anion by protons is accompanied by deuterium exchange at the C-5 position (Figure 5.15).⁷ This result was attributed to the low lying LUMO for the resulting tetraenone and subsequent facile internal conversion. In the case of quinolinium salts, nucleophilic attack at C-5 would produce an electronically similar oligoene, and it is possible that internal conversion induced by nucleophiles may involve such an intermediate or, at least, approach to such an intermediate (Figure 5.16).

Semiempirical calculations were done using the AM1 method and suggest that, in the ground state, such an intermediate has no barrier to immediate collapse to the two species. Nevertheless, as the nucleophile approaches the excited quinolinium, the low-lying ground-state may provide a facile curve-crossing mechanism for internal conversion. It is noted, however, that this is an uncommon mechanism that produces no

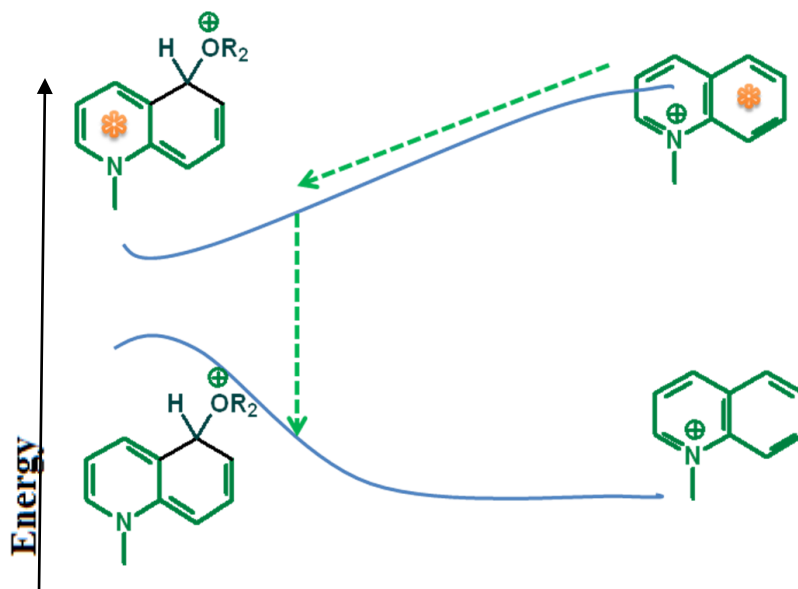


Figure 5.16. Nucleophilic quenching mechanism of quinolinium salts.

permanent photochemistry. Although most literature to-date claims quinolinium quenching via an electron-transfer mechanism, changing the chain length of the *N*-alkyl group has been shown to change the quenching properties of the fluorophore, which is consistent with a nucleophilic mechanism.^{4c,d} Although rigorous excited-state multiconfiguration methods might provide some insight into the decay mechanisms, there are fraught with sources of error, and we are reluctant to embark on them without a rigorous collaborator.

It must be stated that nucleophilicity is not an intrinsic property of a species, but rather a convolution of electron-donating ability, polarizability, and solvation. The intervention of electron-transfer to generate discrete radical ion intermediates at one end or via simple configuration interaction at another may just be two extremes of highly correlated processes.

If one assumes that the nucleophilicity of the quencher is the driving force behind the quenching reaction, it is not at all surprising that, with the exception of MHQ and 6CNMQ, quinolinium salts are not quenched by hydroxylic solvents. Water and alcohols are known to be relatively weak nucleophiles,⁸ and therefore a strong emission in the presence of these solvents is expected.

For the case of MHQ under these conditions, an ESPT reaction can occur. From the time-resolved data, it can be concluded that ESPT can occur even in very low concentrations of water (Figures 5.11, 5.12). ESPT-induced quenching is a known phenomenon.⁹ While the exact mechanism of the quenching of MHQ has not been resolved, it is clearly the case that conditions under which ESPT occurs, fluorescence quenching also occurs. The theory of “aborted proton-transfer quenching mechanism” has been previously reported¹⁰ where the system evolves on the excited-state surface along the proton transfer reaction coordinate and very quickly reaches a region where there is an intersection with the ground-state surface that leads to ultrafast internal conversion before the ESPT reaction is complete. This is an intriguing idea that requires more attention. However, Kovalenko et al. studied the stimulated emission spectra of MHQ and reported the appearance of the Z^* band within 2 picoseconds that is parallel to

the disappearance of the C* band;¹¹ thus, the “aborted proton-transfer quenching mechanism” is most likely not occurring in this system.

The examination of 6MCNQ was an attempt to rule out electronic versus steric effects. While no ESPT reaction can occur, the quenching of 6MCNQ is quite different from that of the other compounds where no ESPT occurs. These results indicate clearly that the electronic structure of the compound plays a role in the fluorescence quenching, even without the possibility of ESPT. It is reasonable to assume that the huge difference in redox potential between the cyano compound¹² and the others could result in such a dramatic difference in the quenching. However, this explanation is not straightforward as there is no obvious correlation between the ionization potential of the quencher and the quenching rate constant of 6CNMQ. Nucleophilicity involves elements of electron transfer, orbital overlap and steric effects. Therefore, the difficulty correlating the quenching to the redox potentials may indicate that the reaction (i.e., bond-making) has progressed relatively far before reaching the high-energy transition state. For very favorable electron transfer, the process takes place without bond formation.

The very efficient quenching by DMSO for all compounds studied is expected as DMSO is known to act as a good nucleophile, where the oxygen is a nucleophile towards hard electrophiles and the sulfur tends to act as the nucleophile towards soft, or more delocalized, electrophiles.¹³ For MHQ, the fluorescence quenching by DMSO is quite dramatic due to the ability of DMSO to efficiently accept and solvate the proton and due to the high nucleophilicity of the quencher. Curiously, while MMQ is not quenched appreciably by any other solvent studied, the quenching constant in the presence of DMSO is quite high, which again can be attributed to the comparatively high

nucleophilicity of DMSO. The efficient quenching by DMF for quinolinium salts is analogous to DMSO, where DMF has been shown to be a relatively good nucleophile.¹⁴

The more efficient quenching by DMSO than by water for MHQ is not unexpected because DMSO is both more basic and more nucleophilic than water. The decrease in fluorescence intensity of MHQ corresponds to the decrease in MHQ lifetime in both solvents, indicating that the quenching mechanism in both solvents is purely dynamic. A purely dynamic quenching mechanism has been previously reported for various quinolinium salts.^{3b}

The effects of the counteranion on the quenching of MHQ were also studied. Figure 5.17 shows the quenching of three different MHQ salts (BF_4^- , SbF_6^- , Nf^-) in DMSO and water.

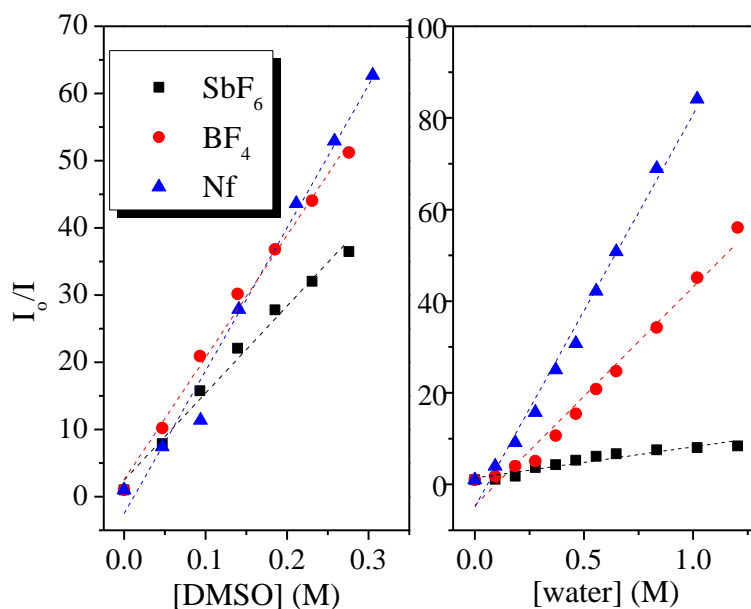


Figure 5.17. Fluorescence quenching of MHQ- SbF_6^- (black), BF_4^- (red), and Nf^- (blue) by DMSO (left) and water (right).

While the quenching of MHQ in DMSO is relatively independent of the counteranion present, this is not the case for water. When MHQ is quenched by water, the k_q is heavily dependent on the counteranion. Interestingly, the quenching is an inverse function of the appearance of the long-lifetime tail (Figure 3.8, left panel) where the magnitude of the tail is in the order of $\text{Nf}^- < \text{BF}_4^- < \text{SbF}_6^-$ and the rate of quenching by water follows $\text{SbF}_6^- < \text{BF}_4^- < \text{Nf}^-$. Clearly, this long-lifetime tail is due to some non-reacting form of MHQ that does not show proton transfer, and therefore it is not quenched by water through ESPT. The higher the yield of the long-lifetime tail, the smaller population of C^* emitter is quenched. This observation may help explain the origin of the long-lifetime tail. In the least, it can be concluded quenching is a function of the appearance of the long-lifetime tail as the tail disappears in DMSO where the quenching is independent of counteranion.

The fluorescence from quinolinium salts is heavily quenched by a wide array of solvents including ethers, hydroxylic solvents and “nucleophilic” solvents such as DMSO. There is a strong contribution to the deactivation of MHQ by excited-state proton transfer as can be evidenced by the heavy quenching by all proton accepting solvents. While most studies have concluded that the fluorescence quenching of MQs is caused by electron transfer, this we propose that perhaps nucleophilic attack may lead to deactivation of the excited state, at least in the case of weak nucleophiles such as ethers. This quenching phenomenon is the major drawback to using these very strong photoacids in any applications.

References

1. Lakowicz, J.R. *Principles of Fluorescence Spectroscopy*, 2nd ed.; Springer: New York, 2004; Chapter 8.
2. Weber, G. *Trans. Faraday Soc.* **1948**, 44, 185.
3. (a) Amendola, V.; Fabbrizzi, L.; Monzani, E. *Chem. Eur. J.* **2004**, 10, 76. (b) Jayaraman, S.; Verkman, A.S. *Biophys.Chem.* **2000**, 85, 49. (c) Swinburne, A.N.; Paterson, M.J.; Beeby, A.; Steed, J.W. *Org. Biomol. Chem.* **2010**, 8, 1010(d) Soroka, J. A.; Komorowska, B.; Soroka, K. B.; Bendig, J. *J. Photochem. Photobiol.*, A **1998**, 118, 81 (e) Geddes, C. D.; Apperson, K.; Karolin, J.; Birch, D. J. S. *Anal. Biochem.* **2001**, 293, 60. (f) Chao, S.C.; Tretzel, J.; Schneider, F.W. *J. Am. Chem. Soc.* **1979**, 101, 134.
4. (a) Illsley, N. P., and A. S. Verkman. *Biochemistry* 26: 1215–1219, 1987. (b) Biwersi, J.; Verkman, A. S. *Biochemistry* **1991**, 30, 7879-7883. (c) Lanig, H.; Hof, M. Stahl, T. Schneider, F.W. *Chem. Phys. Lett.* **1994**, 220, 423. (d) Lanig, H.; Engel, T.; Kaeb, G.; Schneider, F. W. *Chem. Phys. Lett.* **1995**, 235, 58-64. (e) Asakawa, T.; Kubode, H.; Ozawa, T.; Ohta, A.; Miyagishi, S. *J. Oleo. Sci.* **2005**, 54, 545-552. (f) Kuwamoto, K.; Asakawa, T.; Ohta, A.; Miyagishi, S. *Langmuir* **2005**, 21, 7691-7695
5. Yoon, U.C.; Quillen, S.L.; Mariano, P.S.; Swanson, R.; Stavinoha, J.L.; Bay, E. *J. Am. Chem. Soc.* **1983**, 105, 1204.
6. Reed, D.T.; Dorfman, L.M. *Macromol.* **1984**, 17, 32.
7. Webb, S.P.; Philips, L.A.; Yeh, S.W., Tolbert, L.M., Clark, J.H. *J. Phys. Chem.* **1986**, 90, 5154.

8. Solomons, T.Q. G.; Fryhle, C. *Organic Chemistry*, 10th ed.; Wiley: New York, 2009, Chapter 6.
9. H. Shizuka *Acc. Chem. Res.* **1985**, 18, 141 and references therein.
10. (a) Sinicropi, A.; Nau, W.M.; Olivucci, M. *Photochem. Photobiol. Sci.* 2002, 1, 537. (b) Sobolewski, A.; Domcke, W. In *Ab-initio Reaction Paths and Potential Energy Functions*; Elsaesser, T., Bakker, H.J., Eds.; Kluwer Academic Publishers: Amsterdam, 2002; p 93.
11. Perez-Lustres, J.L.; Rodriguez-Prieto, F.; Mosquera, M.; Senyushkina, T.A.; Ernsting, N.P.; Kovalenko, S.A. *J. Am. Chem. Soc.* **2007**, 129, 540.
12. (a) Ohkubo, K.; Kobayashi, T.; Fukuzumi, S. *Angew. Chem. Int. Ed.* **2011**, 20, 8652. (b) Baciocchi, E.; Del Giacco, T.; Lanzalunga, O.; Mencarelli, P.; Procacci, B. *J. Org. Chem.* **2008**, 73, 5675. (c) Speelman, A.L.; Gilmore, J.G. *J. Phys. Chem. A* **2008**, 112, 5684.
13. Anslyn, E.V.; Dougherty, D.A. *Modern Physical Organic Chemistry*; University Science Books: Sausalito, CA, 2006.
14. Ahmad, S.M.; Braddock, D.C.; Cansell, G. Hermitage, S.A. *Tet. Lett.* **2007**, 48, 915.

CHAPTER 6

CONCLUSIONS AND FUTURE WORK

In this dissertation, various aspects of excited-state proton transfer were examined. A minor part of the research focused on the chirality effects on the ESPT in 1,1'-bis-2-naphthol (BINOL) and its derivatives while the major part of the research explored the ESPT dynamics of the “super” photoacid, *N*-methyl-6-hydroxyquinolinium. Studies were conducted that included the design, synthesis, and characterization of MHQ. The ESPT kinetics of the photoacid were investigated both experimentally and theoretically, including studying the ultrafast kinetics and using Brownian dynamics simulations to describe the MHQ excited-state proton transfer reaction. Further, several applications of MHQ were explored including its use as a photoinitiator in the cationic polymerization of a simple epoxide, as a tool to understand the microheterogeneous environment of gas-expanded liquids, and finally as a photoprobe to explore the proton transport channels in the Nafion membrane. Because a substantial fluorescence quenching effect was noted, the quenching of various quinolinium salts by a wide array of solvents was studied.

By using Brownian dynamics simulations, we were able to accurately model and fit the kinetics of the MHQ system. Although it is customary to employ the Spherical Symmetric Diffusion Problem (SSDP) when the kinetics of a photoacid system cannot be solved analytically, the totally new dynamics of ESPT from the charge structure of MHQ made this impossible. This impossibility occurred because the MHQ system is highly asymmetric and SSDP could not model the time evolutions of the cation and zwitterion

pair. The Brownian dynamics simulations, on the other hand, gave a set of ESPT rate constants, as well as a class of spherically symmetric parameters, that accurately described the MHQ kinetics. The spherically symmetric parameters were then applied to the SSDP program, where the pK_a^* of MHQ was estimated to be ~ -7 in water, making it the strongest photoacid reported to-date.

From the kinetic studies, we determined that the ultrafast kinetics; i.e., the proton-transfer step, are solvent-controlled and that the lifetimes approach the dielectric solvent relaxation times, τ_D . We also observed the appearance of a long-lifetime emitter, whose presence was not predicted by the theoretical model, and that in some cases accounts for $>10\%$ of the overall emitting species. The precise origin of this tail remains elusive; however, it is clearly due to some unreactive form of MHQ; i.e., aggregates or other species that do not exhibit proton transfer. The MHQ ESPT temperature dependence in various alcohols was studied and compared to the well-known “super” photoacid DCN2. Different behavior was observed for MHQ than that which was previously reported for DCN2. This difference was attributed to the differences in the excited-state acidities of MHQ and DCN2 ($\Delta\text{pK}_a^* \approx 3$), where the relative contributions of the solvent-coordinate and the proton-transfer coordinate change for the photoacids. The protolytic dissociation rate constant for MHQ was higher than for DCN2, while the ESPT activation energies of MHQ were smaller. Finally, we concluded that the previously reported model for DCN2 does not accurately describe the MHQ system.

The properties of MHQ as a photoinitiator in the cationic polymerization of cyclohexene oxide were explored. While MHQ did catalyze the reaction, a set of control experiments revealed that direct-ESPT was not the mechanism of the catalysis. In fact,

latent acid formation was detected under all conditions and several important observations were made. A strong-dependence on the counteranion present was noted; only salts with fluoride-containing counteranions catalyzed the reaction. Several mechanisms for the production of protons are possible including proton abstraction from the MHQ methyl group, or electron transfer from the CHO to the quinolinium followed by proton abstraction from the CHO. Further, acetone was required for the polymerization to occur, suggesting that the excited state of acetone plays a role in the polymerization mechanism. Finally, control experiments using other phenolic photoacids that had been previously reported to induce polymerization via a direct-ESPT showed that latent acid is generated under those conditions as well.

The ESPT properties of MHQ in gas-expanded methanol were studied through steady-state and time-resolved measurements. The kinetics were analyzed using SSDP and the protolytic dissociation rate was found to be nearly constant under all conditions. From these results, it was concluded that the system is solely in the exergonic regime ($\Delta G < 0$) where extremely strong preferential solvation by methanol governs the ESPT rates. Under these conditions, the amount of methanol in the system is high enough that the preferential solvation by methanol overcomes any breaking of the methanol/proton network that would occur upon injection of CO₂ into the system.

The proton-transport properties of Nafion were explored by examining the ESPT of MHQ in Nafion membranes. We found that ESPT increases as a function of increasing hydration level in the film, and that no ESPT is seen in dry films. These results were consistent with previously reported work on ESPT in Nafion. Because we were stymied in these studies by the intervention of strong fluorescent quenching in the presence of

water, we were not able to develop a good model for the proton channels in Nafion. However, this observation led us to study of the quenching by a variety of solvents on MHQ and other quinolinium salts as a phenomenological issue.

The fluorescence from quinolinium salts is heavily quenched by a variety of solvents. Specifically, a strong quenching by weak nucleophiles such as ethers was observed. While the exact mechanism of this quenching is unresolved, we proposed a mechanism involving nucleophilic attack on the electron-poor aromatic ring, leading to the development of a curve crossing with the ground state and rapid internal conversion. The quenching by MHQ specifically by proton-accepting solvents was attributed to ESPT-induced quenching. Finally, we determined that the extremely enhanced quenching by solvents such as DMSO and DMF on MHQ could be explained by both the proton-accepting and nucleophilic properties of these solvents.

In summary, the present research allowed for a more complete understanding of the ESPT dynamics in the MHQ system. Consequently, we should expect that the characterization of the compounds will allow for optimization of the ESPT so that this class of photoacids can be used in a wider range of applications. Upon complete elucidation of these mechanisms, we can begin to use the transient control of acidity made available by MHQ in a variety of applications. Due to the lack of research in the area of cationic “super” photoacids, this research is important to the fundamental understanding of such systems. The research expanded the range of photoacids available for fundamental studies on proton-transfer kinetics by proposing a new mechanism for a highly anisotropic photoacid system and developing the strongest photoacid reported to-date. The testing of this new mechanism on other cationic and anionic photoacids that

exhibit similar anisotropic behavior in the excited state may yield more information regarding these systems.

To extend the investigation of “super” photoacids, chirality could be introduced into the system. Since the photochemistry and photophysics of BINOLs have previously been investigated as described above, a logical extension would be to synthesize *N*-alkylated azaBINOLs. (Figure 6.1) *O,O'*-dialkylated derivatives of enantiopure azaBINOLs can be mono- or diquaternized easily by alkyl halides, followed by

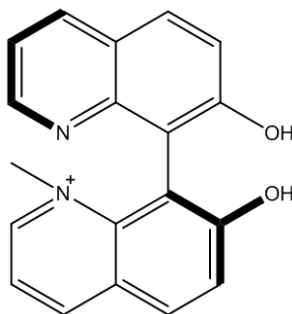


Figure 6.1. Proposed chiral “super” photoacid.

deprotection of the ether linkages resulting in the desired photoacids. As shown with MHQ, *N*-alkylated hydroxyquinolines exhibit enhanced photoacidity and the bulky alkyl groups could prevent the ESPT-induced photoracemization observed for BINOLs. This could produce a strong, stable “super” photoacid that could transfer a proton to various weak chiral proton acceptors.

Further, one could increase the number of aromatic rings in the system and the distance between the charges by incorporating the *N*-alkyl and hydroxyl functionalities into a molecule like anthracene or pentacene. (Figure 6.2) Investigations could examine

the influence of separating the charges on the dipole moment and the dynamics of the proton, as well as the quenching of the system. Further exploration into the fluorescence quenching would be fruitful, i.e. is this quenching limited to the quinoliniums or is it common for the whole class of highly anisotropic photoacids? Once a system is developed that is not quenched, the photoacid can be attached to any substituent through quaternization of the nitrogen. The quaternization would allow the probe to be covalently bonded to a variety of systems including, but not limited to, nanoparticles through an –SH linker and amino acids in biological systems.

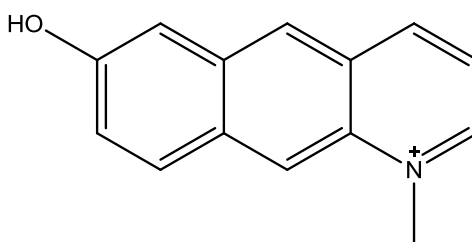


Figure 6.2. Proposed anthracene-based “super” photoacid.

The quenching of quinolinium salt fluorescence by solvents, either through electron-transfer or through nucleophilic attack, presents an obstacle toward using these highly photoacidic species in other diagnostic or catalytic ways. We continue to be intrigued, however, by ways in which such quenching could be inhibited. It is possible that increased steric hindrance by larger protective groups on the quaternary nitrogen would be effective. Alternatively, use of sequestering agents to create encapsulated compounds in which the proton would be small enough to enter or leave presents a tantalizing prospect. Clearly the reactivity induced by the electronic structures of hydroxyquinolinium salts and their excited states required extraordinary measures to capture their unique reactivity.

As stated previously, photoacids may act as probes in biological and material applications. Specifically, proton transport dynamics can be used in a variety of media including biological systems and synthetic membranes. To comment on the proton transport through these systems can help optimize their final use in fuel cells, drug therapies, and a variety of other applications.

APPENDIX A

CHARACTERIZATION OF COMPOUNDS STUDIED

***N*-methyl-6-hydroxyquinolinium Iodide.** mp 224-226 °C. ¹H NMR (300 MHz, Acetone) δ 10.09 (s, 1H), 9.34 (d, J = 5.0, 1H), 9.10 (d, J = 8.5, 1H), 8.54 (d, J = 9.5, 1H), 8.11 (dd, J = 5.7, 8.5, 1H), 7.92 (dd, J = 2.8, 9.6, 1H), 7.75 (d, J = 2.7, 1H), 4.84 (s, 3H); EIMS, m/z 160.1 (M⁺, 24%), 145.1 (100%), 89.1, 63.1; MS (EI, m/z), calcd. for C₁₀H₁₀NO: 160.076. Found: 160.1.

***N*-methyl-6-hydroxyquinolinium Bromide.** mp 245-246 °C. ¹H NMR (300 MHz, Acetone) δ 10.09 (s, 1H), 9.34 (d, J = 5.0, 1H), 9.10 (d, J = 8.5, 1H), 8.54 (d, J = 9.5, 1H), 8.11 (dd, J = 5.7, 8.5, 1H), 7.92 (dd, J = 2.8, 9.6, 1H), 7.75 (d, J = 2.7, 1H), 4.84 (s, 3H). EIMS, m/z 160.1 (M⁺, 24%), 145.1 (100%), 89.1, 63.1; MS (EI, m/z), calcd. for C₁₀H₁₀NO: 160.076. Found: 160.1.

***N*-methyl-6-hydroxyquinolinium Triflate.** mp 100-102 °C. ¹H NMR (300 MHz, Acetone) δ 10.09 (s, 1H), 9.34 (d, J = 5.0, 1H), 9.10 (d, J = 8.5, 1H), 8.54 (d, J = 9.5, 1H), 8.11 (dd, J = 5.7, 8.5, 1H), 7.92 (dd, J = 2.8, 9.6, 1H), 7.75 (d, J = 2.7, 1H), 4.84 (s, 3H). EIMS, m/z 160.1 (M⁺, 24%), 145.1 (100%), 89.1, 63.1; MS (EI, m/z), calcd. for C₁₀H₁₀NO: 160.076. Found: 160.1.

***N*-methyl-6-hydroxyquinolinium Nonaflate.** mp 125-126 °C. ¹H NMR (300 MHz, Acetone) δ 10.09 (s, 1H), 9.34 (d, J = 5.0, 1H), 9.10 (d, J = 8.5, 1H), 8.54 (d, J = 9.5, 1H), 8.11 (dd, J = 5.7, 8.5, 1H), 7.92 (dd, J = 2.8, 9.6, 1H), 7.75 (d, J = 2.7, 1H), 4.84 (s, 3H). EIMS, m/z 160.1 (M⁺, 24%), 145.1 (100%), 89.1, 63.1; EIMS, m/z 160.1 (M⁺, 24%), 145.1 (100%), 89.1, 63.1; MS (EI, m/z), calcd. for C₁₀H₁₀NO: 160.076. Found: 160.1.

***N*-methyl-6-methoxyquinolinium Nonaflate.** mp 83-85 °C. ¹H NMR (300 MHz, Acetone) δ 9.41 (s, 1H), 9.21 (d, J = 8.5, 2 4 1H), 8.58 (d, J = 10.1, 1H), 8.17 (dd, J = 5.7, 8.5, 1H), 7.93 (dd, J = 2.7, 8.0, 2H), 4.86 (s, 3H), 4.09 (d, J = 1.9, 3H).

***N*-methyl-6-hydroxyquinolinium Hexafluorophosphate.** mp 164-168 °C. ¹H NMR (300 MHz, Acetone) δ 10.09 (s, 1H), 9.34 (d, J = 5.0, 1H), 9.10 (d, J = 8.5, 1H), 8.54 (d, J = 9.5, 1H), 8.11 (dd, J = 5.7, 8.5, 1H), 7.92 (dd, J = 2.8, 9.6, 1H), 7.75 (d, J = 2.7, 1H), 4.84 (s, 3H). EIMS, m/z 160.1 (M⁺, 24%), 145.1 (100%), 89.1, 63.1; MS (EI, m/z), calcd. for C₁₀H₁₀NO:160.076. Found: 160.1.

***N*-methyl 6-hydroxyquinolinium Tetrafluoroborate.** mp 151-152 °C. ¹H NMR (300 MHz, Acetone) δ 10.09 (s, 1H), 9.34 (d, J = 5.0, 1H), 9.10 (d, J = 8.5, 1H), 8.54 (d, J = 9.5, 1H), 8.11 (dd, J = 5.7, 8.5, 1H), 7.92 (dd, J = 2.8, 9.6, 1H), 7.75 (d, J = 2.7, 1H), 4.84 (s, 3H). EIMS, m/z 160.1 (M⁺, 24%), 145.1 (100%), 89.1, 63.1; MS (EI, m/z), calcd. for C₁₀H₁₀NO:160.076. Found: 160.1.

***N*-methyl-6-hydroxyquinolinium Hexafluoroantimonate.** mp 195-197 °C. ¹H NMR (300 MHz, Acetone) δ 10.09 (s, 1H), 9.34 (d, J = 5.0, 1H), 9.10 (d, J = 8.5, 1H), 8.54 (d, J = 9.5, 1H), 8.11 (dd, J = 5.7, 8.5, 1H), 7.92 (dd, J = 2.8, 9.6, 1H), 7.75 (d, J = 2.7, 1H), 4.84 (s, 3H). EIMS, m/z 160.1 (M⁺, 24%), 145.1 (100%), 89.1, 63.1; MS (EI, m/z), calcd. for C₁₀H₁₀NO:160.076. Found: 160.1.

***N*-methylquinolinium Nonaflate.** ¹H NMR (300 MHz, Acetone) δ 9.62 (d, J = 5.7, 1H), 9.38 (d, J = 8.4, 1H), 8.68 (d, J = 9.6, 1H), 8.56 (d, J = 8.1, 1H), 8.38 (m, J = 7.2, 1H), 8.27 (m, J = 8.4, 1H), 8.14 (m, J = 7.2, 1H), 4.91 (s, 3H).

***N*-methyl6-cyanoquinolinium Nonaflate.** ^1H NMR (300 MHz, Acetone) δ 9.81 (d, $J=5.7$, 1H), 9.51 (d, $J=8.7$, 1H), 9.13 (d, $J=2.1$, 1H), 8.91 (d, $J=9.3$, 1H), 8.62 (dd, $J=1.8$, 9.3, 1H), 8.45 (dd, $J=2.7$, 8.4, 1H), 4.99 (s, 3H).

APPENDIX B

SSDP FITS FOR MHQ KINETICS

Table B.1 SSDP fit parameters for MHQ in alcohols . Values of τ_{Z^*} are obtained from the experiment while those which are in parentheses are found during SSDP-fitting.

Solvent	T (K)	k_d (ns ⁻¹)	k_r (Å/ns)	R_D (Å)	a (Å)	τ_{C^*} (ns)	τ_{Z^*} (ns)	D (cm ² /s)	τ (ns)
BuOH	173	0.7	0.08	54.8	5.5	18	8.8	1.0e-6	--
	185	0.9	0.13	51.2	5.5	18	(7.494)	2.0e-6	--
	197	2.0	0.22	48.1	5.5	18	6.5	5.0e-6	--
	210	2.5	0.42	45.1	5.6	18	(5.5)	(7.2e-6) 8.0e-6	3
	222	3.3	0.42	42.7	5.7	18	4.2	(6.8e-6) 8.5e-6	2.5
	235	4.6	0.6	40.3	5.7	18	(2.805)	(6.5e-6) 10.0e-6	2
	248	6	0.4	38.2	5.7	18	2.0	(5.5e-6) 11.0e-6	2
	260	7	0.6	36.4	6	18	(1.978)	(5.5e-6) 11.0e-6	2
	273	9	0.43	34.7	5.9	18	1.8	(5.5e-6) 11.0e-6	2
	285	13	0.6	33.2	5.8	18	(1.482)	(5.5e-6) 11.0e-6	2

	293 ^a	13	0.4	35.8	5.7	20	1.25	5.71e-6	--
PrOH	173	1.3	0.45	44.7	5.7	18	9.5	1.5e-6	--
	185	2.2	0.7	41.8	5.7	18	(6.953)	3.5e-6	--
	197	3.3	1	39.3	5.7	18	5.2	6.0e-6	--
	210	4.2	1.7	36.8	5.8	18	(4.107)	9.0e-6	--
	222	6	2.1	34.9	6	18	3.3	12.0e-6	--
	235	8	2.9	32.9	6	18	(2.713)	14.0e-6	--
	248	10	3	31.2	6.3	18	2.3	15.0e-6	--
	260	14	3.5	29.8	6.2	18	(2.2)	15.0e-6	--
	273	18	4	28.3	6.2	18	1.8	15.0e-6	--
	297	20	6	27.1	6.3	18	(1.6)	15.0e-6	--
EtOH	168	3	1	41.3	6.3	18	4.0	1.5e-6	--
	185	4.5	1.6	37.5	6.3	18	3.5	5.0e-6	--
	197	6.5	3	35.2	6.3	18	3.0	11e-6	--
	210	10	3.2	33.1	6.3	18	2.5	19e-6	--
	222	11.5	3.4	31.3	6.3	18	(2.203)	20e-6	--

	235	13	4.8	29.5	6.4	18	(1.96)	23e-6	--
	248	18	5.5	28.0	6.4	18	1.9	25e-6	--
	273	24	6	25.4	6.5	18	1.5	25e-6	--
	297	28	11	23.4	6.4	18	1.2	25e-6	--

^aFrom Popov et. al. PCCP, 2011, 13, 14914.

T : temperature in Kelvin at which measurement taken

k_p : proton transfer rate in ns⁻¹

k_r : recombination rate in Å/ns

R_D : Debye radius calculated from the temperature-dependent formula $R_D = 168668/\epsilon \cdot T$ in Å

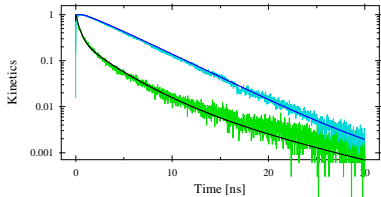
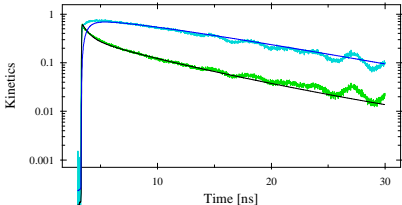
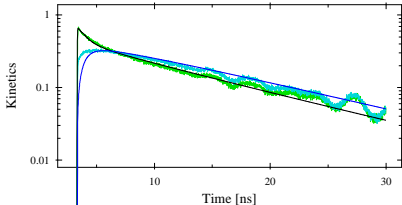
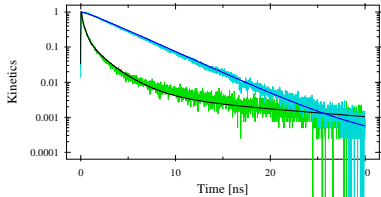
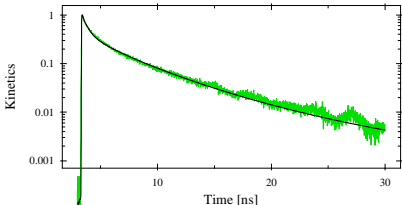
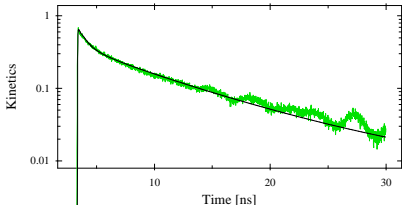
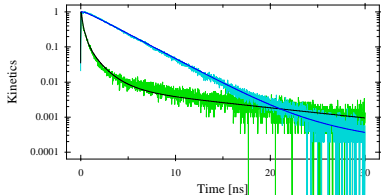
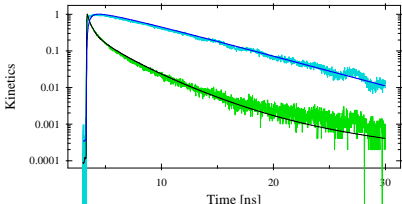
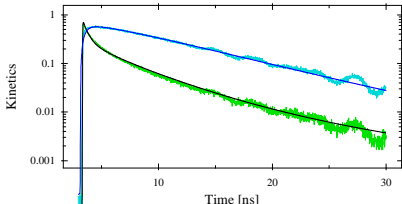
a : reaction space in Å

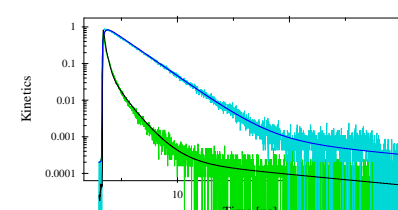
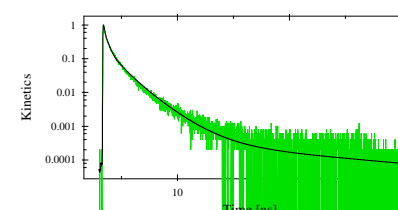
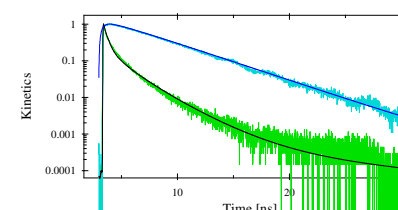
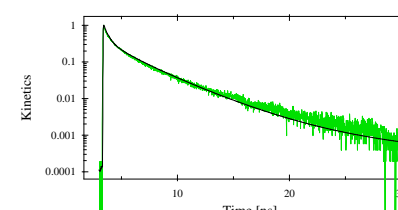
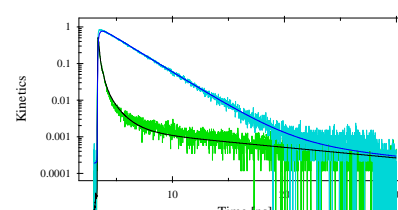
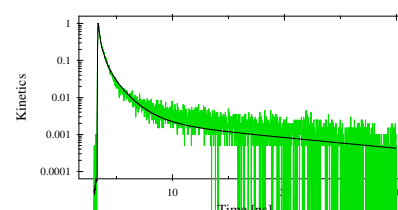
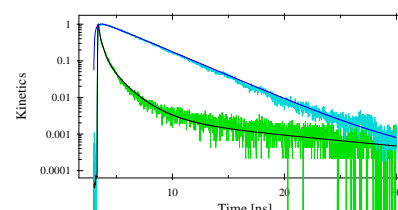
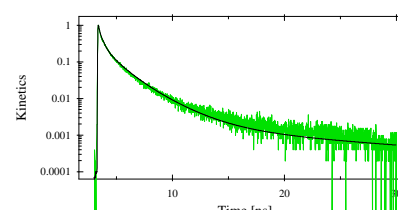
τ_{ROH^*} : lifetime of the bound, cationic state of MHQ in ns

τ_{RO^*} : lifetime of the unbound, zwitterionic state of MHQ in ns

D : diffusion coefficient in cm²/s When two diffusion coefficients are presented, the first one (in parentheses) denotes the initial diffusion coefficient, D_0 , and the second one denotes the final diffusion coefficient, D_1 (see the text).

Table B.2 SSDP Fits of C* (green) and Z* (cyan) decays on MHQ in various alcohols at different temperatures.

T (K)	EtOH	PrOH	BuOH
168			
173			
185			
197			



260

273

285

297

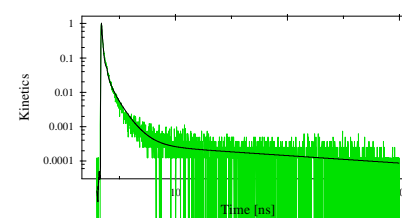
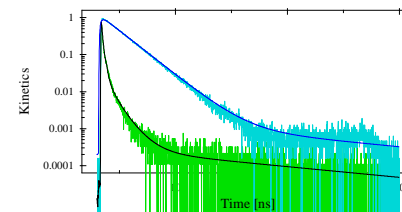
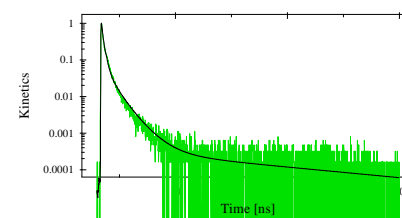
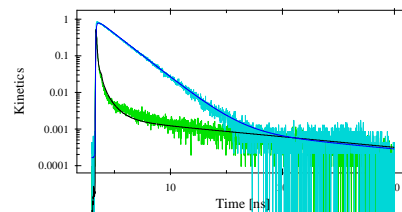
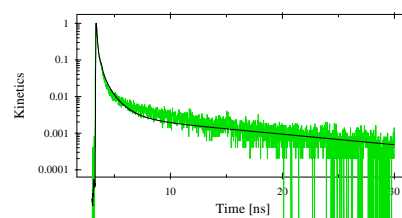
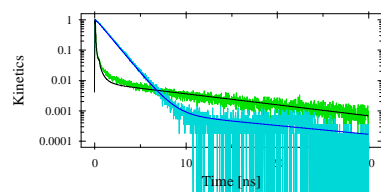
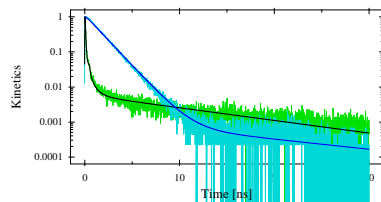


Table B.3. SSDP fit parameters for MHQ in MeOH/scCO₂ mixtures. Values of τ_{z^*} are obtained from the experiment while those which are in parentheses are found during SSDP-fitting. **Purple:** 0.33 mL MeOH; **blue:** 0.40 mL MeOH; **yellow:** 0.50 mL MeOH

X_{MeOH}	T (K)	P (bar)	R_D (Å)	D (cm ² /s)	A (Å)	τ_{C^*} (ns)	τ_{Z^*} (ns)	k_d (ns ⁻¹)	k_r (Å/ns)
0.38	330	140	18.9	1.85e-5	5.0	18	0.48	12	9.0
0.37	323	141	18.5	1.85e-5	5.0	18	0.56	12	8.0
0.40	313	141	18.2	1.85e-5	5.0	18	0.62	12	7.8
0.32	323	197	18.5	1.85e-5	5.0	18	0.54	12	9.2
0.46	313	200	18.2	1.85e-5	5.0	18	0.58	12	12.5
0.25	330	210	18.9	1.85e-5	5.0	18	0.48	12	9.5
0.40	313	129	18.2	1.85e-5	5.0	18	0.75	14.6	13
0.46	323	130	18.5	1.85e-5	5.0	18	0.64	14.6	12.8
0.47	330	132	18.9	1.85e-5	5.0	18	0.60	14.6	12.5
0.38	323	195	18.5	1.85e-5	5.0	18	0.62	14.6	12.9
0.38	313	197	18.2	1.85e-5	5.0	18	0.72	14.6	13.8
0.32	330	199	18.9	1.85e-5	5.0	18	0.58	14.6	13.2

0.55	330	137	18.9	1.85e-5	5.0	18	0.61	13	8.5
0.55	313	140	18.2	1.85e-5	5.0	18	0.68	13	7.0
0.51	323	146	18.5	1.85e-5	5.0	18	(0.74)	13	6.5
0.32	323	200	18.5	1.85e-5	5.0	18	0.68	13	8.0
0.61	313	200	18.2	1.85e-5	5.0	18	0.70	13	10
0.38	330	215	18.9	1.85e-5	5.0	18	0.8	13	7.8

Table B.4 SSDP Fits of C* (green) and Z* (cyan) decays on MHQ in MeOH/scCO₂ mixtures; vol MeOH=0.33 mL.

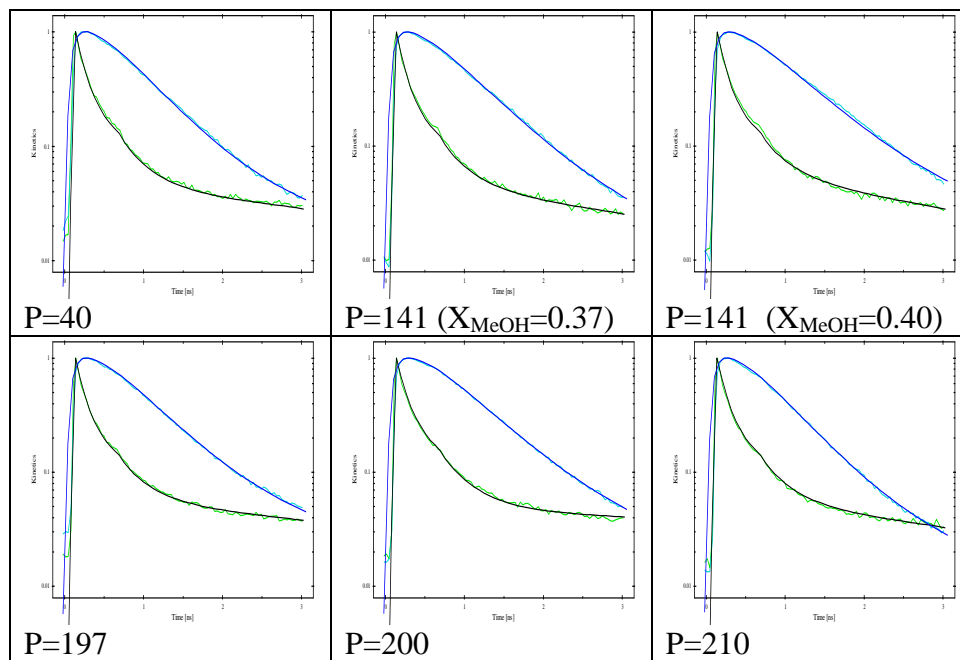


Table B.5 SSDP Fits of C* (green) and Z* (cyan) decays on MHQ in MeOH/scCO₂ mixtures; vol MeOH=0.40 mL

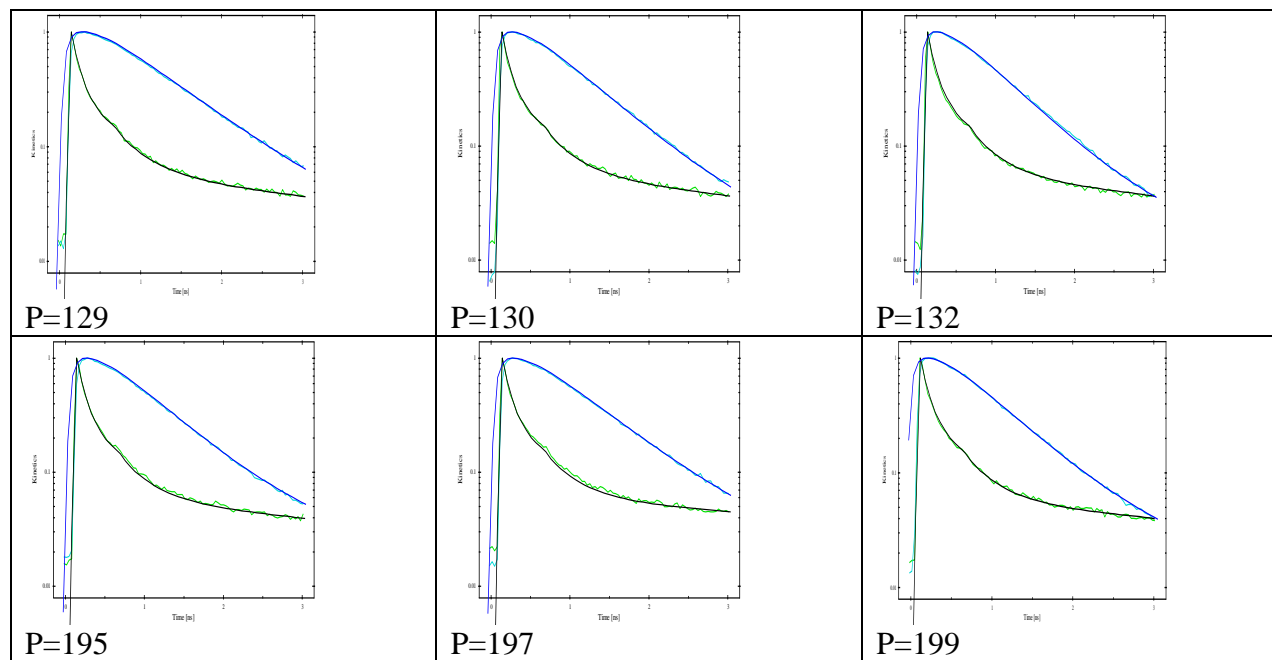


Table B.6. SSDP Fits of C^* (green) and Z^* (cyan) decays on MHQ in MeOH/scCO₂ mixtures; vol MeOH=0.50 mL

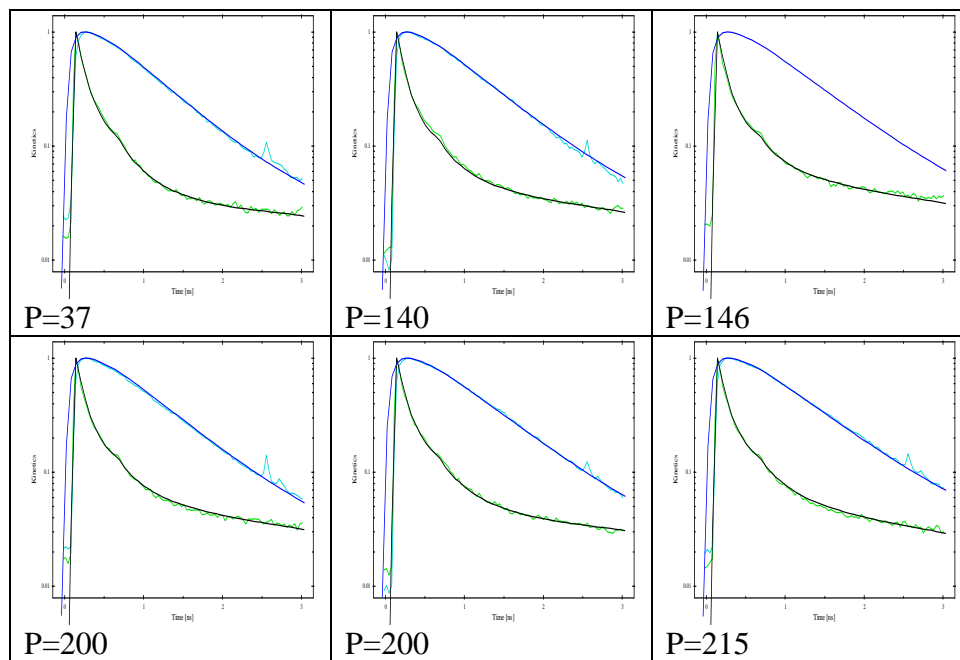
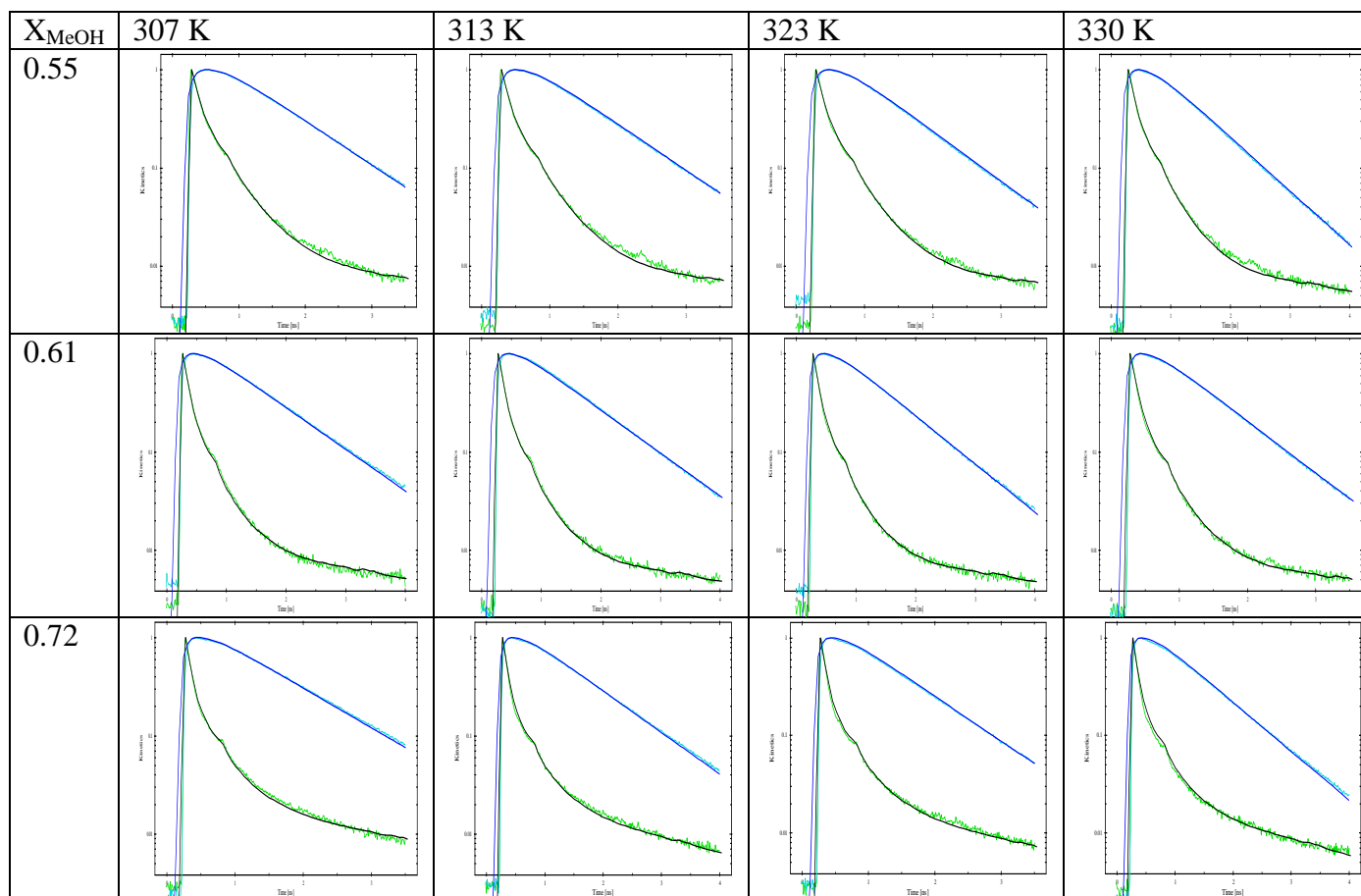


Table. B.7. SSDP fit parameters for MHQ in MeOH/scCO₂ mixtures.

X_{MeOH}	T (K)	R_D (Å)*	D (cm ² /s)	A (Å)	τ_{c^*} (ns)	τ_{z^*} (ns)	k_d (ns ⁻¹)	k_r (Å/ns)
0.55	307	18.1	1.85e-5	5.0	18	0.93	11	10.6
0.61	307	18.1	1.85e-5	5.0	18	1.0	12	5.5
0.72	307	18.1	1.85e-5	5.0	18	1.05	15	7.5
0.55	313	18.2	1.85e-5	5.0	18	0.89	11	9.8
0.61	313	18.2	1.85e-5	5.0	18	0.98	12	5.5
0.72	313	18.2	1.85e-5	5.0	18	1.0	15	7.5
0.55	323	18.5	1.85e-5	5.0	18	0.82	11	9.0
0.61	323	18.5	1.85e-5	5.0	18	0.86	12	5.5
0.72	323	18.5	1.85e-5	5.0	18	0.92	15	7.0
0.55	330	18.9	1.85e-5	5.0	18	0.76	11	8.0
0.61	330	18.9	1.85e-5	5.0	18	0.80	12	5.2
0.72	330	18.9	1.85e-5	5.0	18	0.84	15	7.0

Table B.8. SSDP Fits of C* (green) and Z* (cyan) decays on MHQ in MeOH/dioane mixtures.



APPENDIX C

ALGORITHM OF BROWNIAN DYNAMICS SIMULATIONS

*From Popov, A.V., Gould, E.-A.; Salvitti, M.A.; Hernandez, R.; Solntsev, K.M. *Phys. Chem. Chem. Phys.* **2011**, 13, 14914.

The algorithm for the BD simulations described in this Appendix was developed by Alexander V. Popov of the Hernandez Group at Georgia Institute of Technology.

The BD simulations of the reaction process or the numerical implementation of the Debye-Smoluchowski equation (DSE) using computers allows one to model very complex systems. Further, the DSE is a purely statistical approach used to calculate averaged quantities. It has specific limitations like space and time scale coarse graining and mean-field considerations of forces between particles.

C.1 The geometric scheme

To construct a suitable model system, a coarse-grained geometrical model must first be built to account for the main features of the spatial structure and the force field of the system. The particle sizes in the model are chosen to be close to real molecular sizes. However, one should remember that the particle sizes are frequently treated as fitting parameters and are included in the calculations together with other variables like reaction rate constants, *etc.*¹

The geometrical scheme of the system is shown in Figure C.1. The molecular minimum energy configurations were obtained by the Avogadro software.² The combination of spheres of different sizes was used to mimic the forms of the molecules.

The proton is presented as a sphere with a covalent radius $R_P = 0.4 \text{ \AA}$.³ The radius of the CI ($\text{C}_4\text{F}_9\text{SO}_3^-$) is chosen to be $R_{\text{CI}} = 3 \text{ \AA}$ and indicates its size rather than shape. We assume that the charge of the CI, rather than its shape, affects the dynamics of the proton.

Modeling the Z^* as a dumb-bell shaped particle consisting of two adjoining spheres (instead of one in the spherically-symmetrical case) is the central modification of the algorithm. It becomes very important when the dynamical and reaction properties — the diffusion coefficients and the reaction rates — are assigned to the system. Indeed, this representation naturally prevents the acid molecule from fast rotations allowing the system to evince its anisotropy character. The spheres have the same radius $R_{Z^*} = 2.5 \text{ \AA}$, which approximately corresponds to the distance between the centers of each ring and the hydrogen atoms.

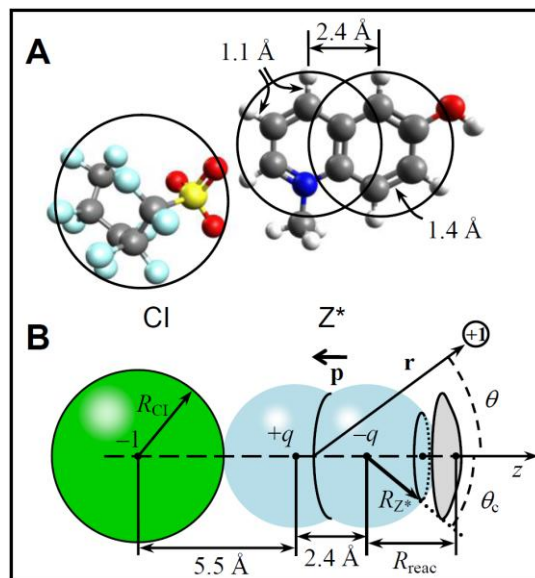


Figure. C.1. Real (A) and model (B) systems. (A) Real chemical system. Numbers are covalent bond lengths taken from Ref. 3 (B) The coarse-grained model. The sphere and the dumbbell represent CI and Z^* , correspondingly. \mathbf{r} and θ are the coordinates of the proton relative to Z^* ; the charges (± 1 and $\pm q$) are put in the centers of the corresponding spheres and define the dipole moment \mathbf{p} ; the reaction zone (the lens) is defined by the apex angle θ_c , distance R_{reac} and width Δ .

C.2. Forces

The interactions within pairs of particles are constituted from long-ranged, attractive/repulsive Coulomb and short-ranged, repulsive harmonic potentials. The former is described by the formula

$$U_{i,j}^C(r) = k_B T \frac{R_D}{r} q_i q_j, \quad (\text{Eq. C.1})$$

where R_D is the Debye radius taken equal to 35.8 Å in butanol;⁴ q_i and q_j are the charges on corresponding particles: for the proton $q_P = 1$, for the CI $q_{CI} = -1$, for the negative and positive parts of the Z^* $q_{Z^*+} = -q_{Z^*-} = 5/2.4 \approx 2.08$. These charges and their allocation are taken to keep the value of the dipole moment of the Z^* in the excited state close to the experimental one, $|p| = 5 \text{ D}$.¹³

The repulsive potential between particles i and k reads

$$U_{i,k}^R(r) = \begin{cases} \frac{\mu_{i,k} \omega^2}{2} (r - R_i - R_k)^2, & r < R_i + R_k \\ 0, & r > R_i + R_k \end{cases}. \quad (\text{Eq. C.2})$$

Here $\mu_{i,k}$ is the reduced mass, the sum $R_i + R_k$ constitutes the equilibrium (contact) distance between the particles, and the cyclic frequency is chosen to be the same for all pairs of particles: $\mu = 6 \cdot 10^{14} \text{ s}^{-1}$. The latter corresponds to the vibrational frequency of O-H covalent bond, and is important for calculation of the proton propagation (see below). We found, however, that changing this frequency from 10^{13} to 10^{15} s^{-1} for all the particles does not affect the resultant kinetics.

C.3. Translational and rotational Brownian dynamics

The motion of centers of masses of each representative particle obeys the stochastic equation⁶

$$d\mathbf{r} = \frac{D}{k_B T} \mathbf{F} dt + \sqrt{2Ddt} \cdot \mathbf{W} \quad (\text{Eq. C.3})$$

where \mathbf{F} is the force acting on a particle; D is its translational diffusion coefficient and \mathbf{W} is the vector consisting of three independent random Gaussian numbers (Wiener processes) with the unit width, $\langle \mathbf{W}^2 \rangle = 1$.

The diffusion coefficient for the proton found from conductivity measurements⁷ is $D_P = 85 \text{ \AA}^2/\text{ns}$. The zwitterion diffusion constant, D_{Z^*} , is assumed to be about $75 \text{ \AA}^2/\text{ns}$ in water (and independent of the electronic state). This value is within the range 55–95 $\text{\AA}^2/\text{ns}$, observed for various aromatic compounds.⁸ It was scaled to its value in butanol using the viscosity ratio $\eta_{\text{H}_2\text{O}}/\eta_{\text{BuOH}} = 1:3.64$ to get $D_{Z^*} = 25 \text{ \AA}^2/\text{ns}$. The diffusion coefficient of the CI is taken to be equal to $D_{\text{CI}} = 20 \text{ \AA}^2/\text{ns}$, which is slightly less than that of the Z^* molecule. This is because the diffusion coefficient scales with the molecular size, and the CI is approximately 20% smaller than the Z^* .

The rotation motion of the MHQ is described by the Legendre process⁹

$$d\theta = \frac{D_R}{k_B T} M dt + D_R \cot \theta \cdot dt + \sqrt{2D_R dt} \cdot W_\theta, \quad (\text{Eq. C.4})$$

$$d\varphi = \frac{\sqrt{2D_R dt}}{\sin \theta} \cdot W_\varphi, \quad (\text{Eq. C.5})$$

where M is the torque acting on the molecule and W_θ and W_φ are independent random Gaussian numbers with unit widths.

The rotational diffusion coefficient, D_R , can be found from the fluorescence anisotropy relaxation time as $D_R^{-1} = 6\tau_R$. The relaxation time for Coumarin 153 (C153) in 1-butanol¹⁰ is $\tau_R = 211$ ps. Relaxation time for Z^* can be estimated from the difference in volumes of two molecules: in accordance with hydrodynamic Stokes-Einstein-Debye theory,¹¹ rotational relaxation times are proportional to the volumes of the molecules or, roughly speaking, to the number of atoms (given the bonds and the angles between them are of the same nature and size in these molecules). Simply counting the atoms gives the ratio $\tau_R(Z^*)/\tau_R(\text{C153}) = 22/30$, *i.e.*, $\tau_R \approx 150$ ps – less than that for C153. We believe the difference in the geometry of C153 and Z^* does not significantly affect the rotational properties. Indeed, the maximal lengths and widths relate to each other as 9:7 (for C153) and 8:5 (for Z^*). If we use these values as the axes of ellipsoids circumscribing the molecules then the Perrin's factors,¹² which correct the relaxation times of the axial/equatorial direction vectors, are 0.456/0.497 for C153 and 0.427/0.507 for Z^* – very close to each other.

The largest time step has been chosen to be $dt = 10$ fs. It is small enough that for the proton, the fastest particle in the system, the corresponding diffusion distance is about $\sqrt{D_p dt} \approx 0.03$ Å. A recursive algorithm is implemented which decreases the time step if a change in energy becomes greater than $0.01 k_B T$ at $T=300$ K.

C.4 Reaction

The recombination/dissociation process has a quantum nature, and when considered within the framework of classical diffusion, the concept of the reaction zone with the corresponding reaction probabilities are used to determine the changes in the states of the reagents. The choice of a form of the reaction zone is connected to a specific reaction mechanism, and the uncertainty in defining the radius and width of the reaction zone is related to the statistical description of the chemical kinetic rates used within the DSE approximation.

At the moment of dissociation (formation of the CIP) the proton is transferred to a nearby location somewhere within the first solvation shell. This quick motion is a ballistic trajectory which cannot be adequately described via the model of random walks. It causes the reaction zone to be shifted somewhat away from the contact distance, and its position is defined through R_{reac} (grey lens in Figure C.1). In the simulations different values of R_{reac} are used, beginning from $R_{Z^*} + R_p = 2.9 \text{ \AA}$, to define the most appropriate reaction distance.

The reaction zone is defined by a reactive spot near the negatively charged surface of the Z^* (Figure C.1). This spot segment corresponds to a solid angle of a cone with apex angle $2\theta_c$. Since the reaction is not stereospecific, we assume $\theta_c = \pi/2$, *i.e.*, the proton can attach to and release from any point of the right hemisphere near the negative part of the Z^* dumbbell. The zone is chosen to be narrow with the width $\Delta = 0.1 \text{ \AA}$. The reason of this choice is in the fact that a contact reaction ($\Delta = 0$) is a very good model for many types of diffusion-controlled reactions.

The MHQ cation dissociates with the probability $1 - \exp(-\kappa_d dt)$ for time dt , where κ_d is the dissociation (proton transfer) rate. Immediately after dissociation, the proton is transferred to the closest point in the reaction zone and put within its width with a uniform probability. The constant κ_d is responsible for the quick decay of the bound state population and is established by fitting the simulation data.

The association reaction occurs when the proton diffuses back into the reaction zone. As soon as the proton is found in the reaction zone, it can bind to the Z^* with the probability $1 - \exp(-\kappa_a dt)$, where κ_a is the intrinsic association rate (assumed to be constant within the reaction zone) and dt is the simulation time step. The association rate constant κ_a is found by fitting the simulation data.

In the bound state the proton is connected to the reaction site of the MHQ through the harmonic potential with the cyclic frequency $\omega = 6 \cdot 10^{14} \text{ s}^{-1}$ which corresponds to the vibrational frequency of the hydroxyl group, $\sim 3000 \text{ cm}^{-1}$. This force keeps the proton near the negatively charged sphere of the Z^* at a contact distance $R_P + R_{Z^*} = 2.9 \text{ \AA}$ with the accuracy $\delta R \sim \sqrt{k_B T / m_p \omega^2} \sim 0.03 \text{ \AA}$. The reflective boundary is applied at $\theta = \theta_c$ to prevent the proton from leaving the reaction site.

Note that the association and dissociation reaction rates are implemented into the DSE via the sink terms $w_a(\mathbf{r})$ and $w_d(\mathbf{r})$, which values are equal to κ_a and κ_d/V_R , correspondingly, within the reaction zone which has volume V_R , and zeroes otherwise.

C.5. Lifetimes

Two different lifetimes are included in the simulations, so that the system decays to the ground state with the probabilities $1-\exp(-k_0 dt)$ for the bound (C^*) and $1-\exp(-k'_0 dt)$ for the unbound (Z^*) state.

The excited-state lifetime of the Z^* , $\tau'_0 \equiv 1/k'_0 = 1.25$ ns, was determined directly from the long-time exponential decay of the Z^* fluorescence signal. Determination of the C^* lifetime, $\tau_0 \equiv 1/k_0$, is more problematic, because the measurements under acidic conditions (in attempt to suppress ESPT) led to quenching by protons. For solvents in which C^* does not dissociate (e.g., acetonitrile), we typically find that the difference in C^* lifetimes between MHQ-Nf and its methyl ether MMQ-Nf does not exceed 10%. We have therefore used the major fluorescence decay component of MMQ-Nf, 18 ns, as an estimate for τ_0 .

Obtaining sufficient statistics at times $t > \tau_0, \tau'_0$ requires performing a very large number of runs. This is because numerical simulations with finite lifetimes are restricted in their accuracy at long times where they are interrupted due to decay processes. To improve the accuracy of the calculations we shift the smallest decay rate constant to zero. This procedure amounts to a trivial exponential factor, $\exp(-|k_0 - k'_0| t)$. The ultimate result is then multiplied by this factor.¹³

C.6. Initial configuration

Initial configuration of the system corresponds to the bound state with the CI in a contact position, as it is depicted in Figure C.1. Literature values of the association constants of various organic¹⁴ and inorganic¹⁵ ions in butanol and other high alcohols are in the 10^2 - 10^3 M⁻¹ range. Therefore, it is natural to assume that the majority of MHQ-Nf ionic molecules exist as contact ion pairs.¹⁶

The proton is initially placed at the contact distance from the negatively charged part of the Z* on the spherical segment within the cone angle θ_c .

C.7. Quantities to be fitted

Since the sizes of the molecules and their force field are determined mostly by the molecular geometry and charge distribution, and the mobility properties are taken from the published experimental data, we concentrate our research on finding the important kinetic parameters: κ_a , κ_d , as well as the reaction distance, R_{reac} . The lifetime τ'_0 is found with a good accuracy, but the lifetime τ_0 in the bound state, known only approximately, can also be corrected.

C.8 Derivations of the potential via two methods: PMF from full BD simulations and Kirkwood's averaging

PMF from BD simulations

The effective potential between the proton and the zwitterion was derived via two different methods. The first used full BD simulations to develop a potential of mean force

(PMF) between the proton and Z^* while the second used a simplified version of Kirkwood's averaging to develop a simpler effective potential. The results of the two potentials were compared (Figure 3.13) and it was shown that the latter potential gave accurate results and was therefore the choice for use in the SSDP package.

A way to account for the CI effect is to construct the effective potential between the proton and Z^* . The proton diffuses within the nonstationary force field created by Z^* and CI particles. The effective potential of mean force (PMF) between the proton and Z^* can be obtained by averaging the actual potential with respect to the relative distribution of the CI. The latter can be found directly from the full BD simulations (where all the reaction and forces are included) at any instant of time.

The fact that the proton stays within or near the potential well during the simulation time and, thus, follows the reaction site on the moving and rotating Z^* molecule, naturally leads to the conclusion that it rarely leaves the hemisphere associated with the reaction zone, and the calculation of the radial PMF can be restricted within this hemisphere. Averaging over the whole sphere would work if equilibrium could be established, *i.e.*, if the proton had enough time to fill a large space volume with its trajectory. In a nonequilibrium case we can only assume equilibrium within the PMF minimum, near the reaction site. In the averaging procedure the distance between the proton and the center of the Z^* is kept constant while integrating over the azimuthal angle from 0 to $\pi/2$.

The results of PMF calculations are shown in Figure. C.2. The difference between the upper and lower panels is that the curves in the lower are shifted to match their minima.

Panel A shows that at large distances the PMF is well described by Coulomb forces. This behavior is most pronounced at small times. Indeed, at large distances the proton motion is affected by the sum of charges on the Z^* and CI (which is -1). The CI migrates away with time, as well as the Coulomb part of the potential. Simultaneously, the potential at short distances rises with time. It is caused by leveling out the potential barrier created by the CI.

Panel B shows that the shape of the short-ranged PMF practically does not change and the corresponding force field remains stable. Open circles indicate the displacement of the proton relative to Z^* , determined from the MSDs in Figure 3.14. As it is seen, the proton does not leave the short-ranged part of the PMF during the simulation time. Interestingly, the potential minimum at 4.1 Å corresponds to the distance between the center of the Z^* dumbbell and the “contact” point – the closest location of the proton on the axis z where the attraction force acquires its maximal value (Figure C.1). Note that at other reaction distances this minimum always corresponds to $R_{\text{reac}} + 1.2$ Å.

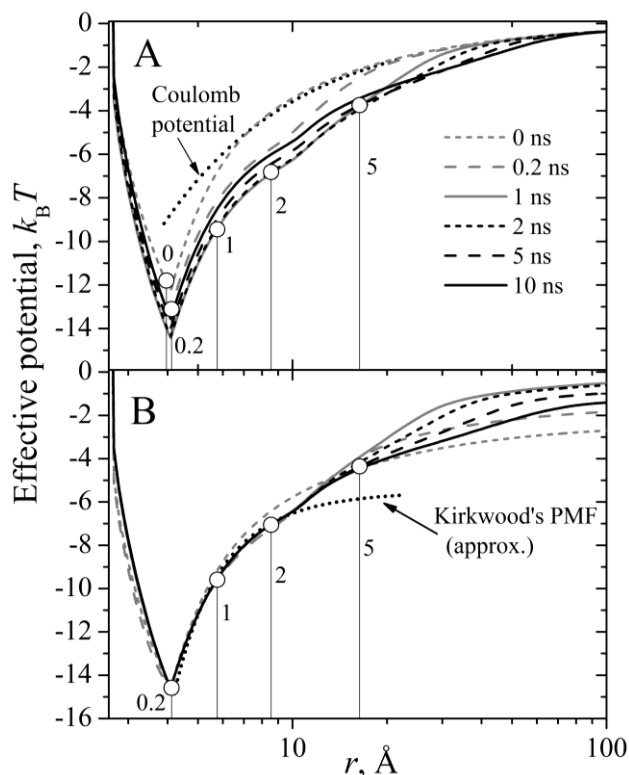


Figure. C.2. The time-dependent PMF between the proton and Z^* at several instants of time (dashed and solid curves). The PMFs in Panel B are shifted to match their minimums. The dotted black curve in Panel A is a pure Coulomb potential, $-R_D/r$, and in Panel B is an approximation arising from the dipole expansion of Kirkwood's PMF, Eq. C.11. Open circles with vertical lines show the characteristic P- Z^* distances at different instants of time (marked by numbers, in ns) as calculated from a square root of the corresponding MSD (see Figure 3.14). Each circle lies on a PMF corresponding to a particular time. The CI does not affect the short-distance forces, which are created, therefore, by the dipole-ion interaction between the proton and the Z^* and can be used for calculating the PMF at distances less than 20 Å.

U_{eff} from Kirkwood's Averaging

In this section we exploit the result that the dynamic part of the problem can be reduced to solely the consideration of the proton motion in the vicinity of the reactive site. We develop a method of calculation of the spherically-symmetric potential of mean force suitable to mimic the essential characteristics of the proton motion – such as reencounter statistics and MSD – to use it in the SSDP.

We employ the idea of averaging a three-dimensional force acting on a proton over the angle variables, θ and φ , thus obtaining the potential of mean radial force.¹⁷ A general representation of this distance-dependant force is

$$F_r(r) = \langle -\nabla_r U(r, \theta, \varphi) \rangle \equiv \frac{-\int_0^{2\pi} d\varphi \int_0^\pi \nabla_r U(r, \theta, \varphi) \rho(r, \theta, \varphi) \sin \theta d\theta}{\int_0^{2\pi} d\varphi \int_0^\pi \rho(r, \theta, \varphi) \sin \theta d\theta} \quad (\text{Eq. C.6})$$

where $\rho(r, \theta, \varphi)$ is the Boltzmann distribution,

$$\rho(r, \theta, \varphi) = A^{-1} \exp(-U(r, \theta, \varphi)/k_B T) \quad (\text{Eq. C.7})$$

with the normalization constant $A = \int_a^\infty r^2 dr \int_0^{2\pi} d\varphi \int_0^\pi \exp(-U(r, \theta, \varphi)/k_B T) \sin \theta d\theta$.

This approach is suitable for calculating the radial distribution of a proton in an ensemble of diffusing nonreactive Z*-proton pairs. However, for our particular case this method needs some modifications.

First, we omit the azimuthal angle, φ , because it can always be integrated out due to the ion-dipole axial symmetry of the potential. Second, the behavior of a proton near a reactive site (which relates to a negative part of the dipole molecule) plays the most significant role, defining the probabilities of reentries of the proton into the reaction zone. Therefore, the integration over θ must be performed within a corresponding cone $0 < \theta < \theta_c$, and the effective potential, U_{eff} , producing the radial force F_r , takes the form

$$U_{\text{eff}}(r) = -k_{\text{B}}T \ln \int_0^{\theta_c} \exp\left(-\frac{U(r, \theta)}{k_{\text{B}}T}\right) \sin \theta d\theta + \text{const} \quad (\text{Eq. C.8})$$

The constant is arbitrary here and will be chosen to annul the energy at large distances.

Using the explicit equation for the ion-dipole interaction with a dipole moment p ,

$$\frac{U(r, \theta)}{k_{\text{B}}T} = R_{\text{D}}p \frac{\cos \theta}{r^2} \quad (\text{Eq. C.9})$$

the effective potential can be found directly from Eq. (C.10):

$$U_{\text{eff}}(r) = k_{\text{B}}T \ln \left(\frac{R_{\text{D}}p(1 - \cos \theta_c)/r^2}{\exp(-R_{\text{D}}p \cos \theta_c/r^2) - \exp(-R_{\text{D}}p/r^2)} \right), \quad (\text{Eq. C.10})$$

which acquires a simpler form at large r :

$$\frac{U_{\text{eff}}(r)}{k_{\text{B}}T} \approx \frac{R_{\text{D}}p}{2r^2}(1 + \cos \theta_c) - \frac{R_{\text{D}}^2p^2}{24r^4}(1 - \cos \theta_c)^2. \quad (\text{Eq. C.11})$$

The difference between Eqs. (C.10) and (C.11) for $R_{\text{D}} = 35.8 \text{ \AA}$ and $p = -5 \text{ D}$ (the minus sign corresponds to the chosen direction of z -axis) is shown in Figure C.3. Because these equations give practically coinciding results at a distance larger than the contact one ($r = a = 4.1 \text{ \AA}$ in this case of the smallest R_{reac}), in the next section the simpler formula (Eq. C.11) will be used.

Potential (Eq. C.11) with $\theta_c = \pi/2$ is also shown in Figure C.2. As can be seen, its form is very close to that of the short-ranged PMF extracted from the BD simulations.

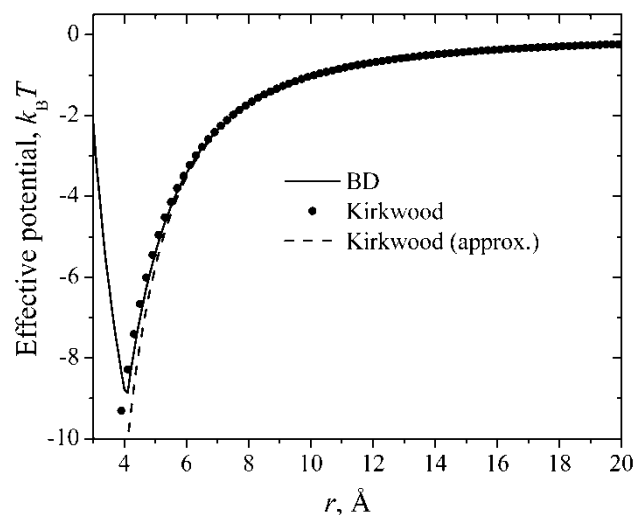


Figure C.3. Comparison of U_{eff} calculated from the BD simulations (solid curve), the PMF from Eqs. (C.10) (circles) and its approximation (C.11) (dashed curve). The angular size of the reactive spot is $\theta_c = \pi/2$. The contact radius corresponds to the minimum at $a = 4.1 \text{ \AA}$.

References

1. Agmon, N. *Chem. Phys. Lett.*, 2006, **417**, 530.
2. <http://avogadro.openmolecules.net/>
3. *CRC Handbook of Chemistry and Physics*. 63rd edition. CRC Press, Inc. Boca Raton, Florida, **1984**.
4. At room temperature the Debye radius $R_D = 566/\epsilon \text{ \AA}$.
5. Pérez Lustres, J.L.; Rodriguez-Prieto, F. ; Mosquera, M. ; Senyushkina, T.A. ;Ernsting, N.P. ; Kovalenko, S.A. *J. Am. Chem. Soc.*, **2007**, 129, 5408.
6. R.M. Mazo. *Brownian Motion: Fluctuations, Dynamics, and Applications*. Clarendon Press. New York, **2002**.

7. Values of D_{H^+} were determined using Nernst equation: $D_{H^+} = RT\lambda^{\circ}/F^2$, where λ° is the limiting proton mobility and F is the Faraday's constant. Value of λ° for HCl in 2-butanol were taken from R. De Lisi, M. Goffredi and V.T. Liveri, *J. Chem. Soc. Faraday, Trans. 1*, **1976**, 72, 436.
8. Sharma, L.R. and Kalia, R.K. *J. Chem. Eng. Data*, **1977**, 22, 39.
9. K. Itô and H.P. McKean, *Diffusion Processes and Their Sample Paths*, **1991**. Springer, Berlin.
10. Horng, M.-L.; Gardecki, J.A.; Maroncelli, M. *J. Phys. Chem. A*, **1997**, 101, 1030.
11. P. Debye. "*Polar Molecules*." Chemical Catalog Co., New York, **1929**.
12. (a) C.R. Cantor and P.R. Schimmel, "*Biophysical Chemistry. Part II. Techniques for the study of biological structure and function*." W. H. Freeman, 1980, pp. 561.
(b) Koenig, S.H. *Biopolymers*, **1975**, 14, 2421.
13. Park, S.; Shin, K.J.; Popov, A.V.; Agmon, N. *J. Chem. Phys.*, **2005**, 123, 034507.
14. (a) El-Hammamy, N.H.; Ahmed, A.M.; Mahmoud, H.A. ; Abd El-Halim, F.M. *J. Electrochem. Soc. India*, **1989**, 28, 269. (b) Ansari, A.A. ; Ansari, M. ; Patel, R.B. ; Topiwala, K.A. *Bull. Electrochem.*, **2005**, 21, 253..
15. Beronius, P. ; Pataki, L. *Acta Chem. Scand. A*, **1979**, 33, 675.
16. Berman, H.A. and Stengle, T.R. *J. Phys. Chem.*, **1975**, 79, 1001.
17. Kirkwood, J.G. *J. Chem. Phys.*, **1935**, 3, 300.